

Two-Phase Flow Heat Transfer in Nuclear Reactor Systems

Guest Editors: Boštjan Končar, Eckhard Krepper,
Dominique Bestion, Chul-Hwa Song, and Yassin A. Hassan





Two-Phase Flow Heat Transfer in Nuclear Reactor Systems

Science and Technology of Nuclear Installations

Two-Phase Flow Heat Transfer in Nuclear Reactor Systems

Guest Editors: Boštjan Končar, Eckhard Krepper,
Dominique Bestion, Chul-Hwa Song, and Yassin A. Hassan



Copyright © 2013 Hindawi Publishing Corporation. All rights reserved.

This is a special issue published in “Science and Technology of Nuclear Installations.” All articles are open access articles distributed under the Creative Commons Attribution License, which permits unrestricted use, distribution, and reproduction in any medium, provided the original work is properly cited.

Editorial Board

Nusret Aksan, Switzerland
A. C. Marques Alvim, Brazil
Won Pil Baek, Republic of Korea
Stephen M. Bajorek, USA
George Bakos, Greece
Jozsef Banati, Sweden
Ricardo Barros, Brazil
Anis Bousbia Salah, Belgium
Giovanni B. Bruna, France
Nikola Čavlina, Croatia
Xu Cheng, China
Leon Cizelj, Slovenia
Alejandro Clausse, Argentina
Francesco D' Auria, Italy
Marcos P. de Abreu, Brazil
Giovanni Dell'Orco, France
Juan Carlos Ferreri, Argentina
Nikolay Fil, Russia
Cesare Frepoli, USA
Giorgio Galassi, Italy
Regina Galetti, Brazil

Michel Giot, Belgium
Valerio Giusti, Italy
Horst Glaeser, Germany
Satish Kumar Gupta, India
Ali Hainoun, Syria
Keith E. Holbert, USA
Kostadin Ivanov, USA
Yacine Kadi, Republic of Korea
Ahmed Khedr, Egypt
Tomasz Kozłowski, USA
Tomoaki Kunugi, Japan
Mike Kuznetsov, Germany
H.-Y. Lee, Republic of Korea
Bundit Limmeechokchai, Thailand
Jiri Macek, Czech Republic
Annalisa Manera, USA
Borut Mavko, Slovenia
Oleg Melikhov, Russia
Rafael Miró, Spain
Josef Misak, Czech Republic
Rahim Nabbi, Germany

Manmohan Pandey, India
Yuriy Parfenov, Russia
Yves Pontillon, France
Nik Popov, Canada
Piero Ravetto, Italy
Francesc Reventos, Spain
Enrico Sartori, France
Carlo Sborchia, France
Massimo Sepielli, Italy
Arkady Serikov, Germany
James F. Stubbins, USA
Iztok Tiselj, Slovenia
Rizwan Uddin, USA
Eugenijus Upuras, Lithuania
Richard Wright, Norway
Chao Xu, China
X. George Xu, USA
Yanko Yanev, Bulgaria
Zhiwei Zhou, China
Enrico Zio, Italy
Massimo Zucchetti, Italy

Contents

Two-Phase Flow Heat Transfer in Nuclear Reactor Systems, Boštjan Končar, Eckhard Krepper, Dominique Bestion, Chul-Hwa Song, and Yassin A. Hassan
Volume 2013, Article ID 587839, 2 pages

CFD for Subcooled Flow Boiling: Parametric Variations, Roland Rzehak and Eckhard Krepper
Volume 2013, Article ID 687494, 22 pages

Bubble Departure Diameter Prediction Uncertainty, Marko Matkovič and Boštjan Končar
Volume 2012, Article ID 863190, 7 pages

CHF Phenomena by Photographic Study of Boiling Behavior due to Transient Heat Inputs, Jongdoc Park, Katsuya Fukuda, and Qiusheng Liu
Volume 2012, Article ID 248923, 12 pages

Aqueous Nanofluid as a Two-Phase Coolant for PWR, Pavel N. Alekseev, Yury M. Semchenkov, and Alexander L. Shimkevich
Volume 2012, Article ID 214381, 6 pages

Depressurization of Vertical Pipe with Temperature Gradient Modeled with WAHA Code, Oriol Costa, Iztok Tiselj, and Leon Cizelj
Volume 2012, Article ID 951923, 9 pages

Validation and Application of the Thermal Hydraulic System Code TRACE for Analysis of BWR Transients, V. H. Sánchez, M. Thieme, and W. Tietsch
Volume 2012, Article ID 247482, 9 pages

A Derivation of the Nonlocal Volume-Averaged Equations for Two-Phase Flow Transport, Gilberto Espinosa-Paredes
Volume 2012, Article ID 890815, 8 pages

Editorial

Two-Phase Flow Heat Transfer in Nuclear Reactor Systems

**Boštjan Končar,¹ Eckhard Krepper,² Dominique Bestion,³
Chul-Hwa Song,⁴ and Yassin A. Hassan⁵**

¹ Reactor Engineering Division, Jožef Stefan Institute, Jamova 39, 1000 Ljubljana, Slovenia

² Helmholtz-Zentrum Dresden-Rossendorf, Institute of Fluid Dynamics, Bautzner Landstraße 400, 01328 Dresden, Germany

³ Commissariat à l'Énergie Atomique (CEA), 17 rue des Martyrs, 38054 Grenoble, France

⁴ Thermal-Hydraulic Safety Research Division, Korea Atomic Energy Research Institute (KAERI), Daedeok-daero 989-111, Yuseong-gu, Daejeon 305-353, Republic of Korea

⁵ Department of Nuclear Engineering, Texas A&M University, 3133 Tamu, College Station, TX 77843-3133, USA

Correspondence should be addressed to Boštjan Končar; bostjan.koncar@ijs.si

Received 10 July 2013; Accepted 10 July 2013

Copyright © 2013 Boštjan Končar et al. This is an open access article distributed under the Creative Commons Attribution License, which permits unrestricted use, distribution, and reproduction in any medium, provided the original work is properly cited.

Heat transfer and phase change phenomena in two-phase flows are often encountered in nuclear reactor systems and are therefore of paramount importance for their optimal design and safe operation. The complex phenomena observed especially during transient operation of nuclear reactor systems necessitate extensive theoretical and experimental investigations.

This special issue brings seven research articles of high quality. Though small in number, they cover a wide range of topics, presenting high complexity and diversity of heat transfer phenomena in two-phase flow. In the last decades a vast amount of research has been devoted to theoretical work and computational simulations, yet the experimental work remains indispensable for understanding of two-phase flow phenomena and for model validation purposes. This is reflected also in this issue, where only one article is purely experimental, while three of them deal with theoretical modelling and the remaining three with numerical simulations.

The experimental investigation of the critical heat flux (CHF) phenomena by means of photographic study is presented in the paper of J. Park et al. They have used a high-speed camera system to observe the transient boiling characteristics on a thin horizontal cylinder submerged in a pool of water or highly wetting liquid. Experiments show that the initial boiling process is strongly affected by the properties and wettability of the liquid. The authors have stressed the

importance of the local scale observation leading to better understanding of the transient CHF phenomena.

In the article of G. Espinosa-Paredes et al. a theoretical work concerning the derivation of transport equations for two-phase flow is presented. The author proposes a novel approach based on derivation of nonlocal volume averaged equations which contain new terms related to nonlocal transport effects. These non-local terms act as coupling elements between the phenomena occurring in at least two different spatial scales.

Uncertainty in modelling of bubble departure diameter at boiling was studied by M. Matkovic and B. Koncar. In this article the propagation of input uncertainties for the simplified model of bubble departure size is evaluated. A methodology for estimating the prediction capability of a given correlation is provided taking into account its range of applicability.

Aqueous nanofluids have a great potential for cooling applications, hence they have been studied in the article of P. N. Alekseev et al. as a possible coolant in pressurized water reactor (PWR). The theoretical study presents how a stable formation of nanoparticles in water solution can be established. Formation of fractal nanoparticles with a higher thermal conductivity than water can enhance the heat transfer of water used as a coolant in PWR. Apart from solid particles, also alternative formation of gaseous nanoparticles in density fluctuations of water is discussed.

The article of R. Rzehak and E. Krepper provides a comprehensive overview of the state-of-the-art in the field of CFD modelling of subcooled flow boiling. The efficient predictive capability of current models requires calibration of model parameters over a wide range of measured data and operating conditions. The results presented in the article confirmed the great potential of the existing modelling approach for the 3D simulation of subcooled flow boiling in industrial applications but also highlight the need for specific model improvements to achieve highly accurate predictions.

Two articles deal with one-dimensional analyses of two-phase flows. In the article of O. Costa et al., a rapid depressurization in vertical heated pipe is simulated with the in-house 1D computer code WAHA, which was developed specifically for simulations of two-phase water hammer phenomena. The WAHA results were confronted with the simulations of the well-known system code RELAP5 on the same experimental data.

The thermal-hydraulic system code TRACE was used for validation of typical transient in Boiling Water Reactor (BWR) as elaborated by V. H. Sanchez et al. A validation of BWR relevant models on the BFBT benchmark experiments was upgraded by development of an integral plant model of the German BWR. The critical power tests with the 2D plant model demonstrated that TRACE predictions are in good agreement with the recorded plant data.

We believe that this special issue provides interesting information on the recent progress in nuclear thermal-hydraulics research.

*Boštjan Končar
Eckhard Krepper
Dominique Bestion
Chul-Hwa Song
Yassin A. Hassan*

Research Article

CFD for Subcooled Flow Boiling: Parametric Variations

Roland Rzehak and Eckhard Krepper

Institute of Fluid Dynamics, Helmholtz-Center Dresden-Rossendorf, P.O. Box 510119, 01314 Dresden, Germany

Correspondence should be addressed to Roland Rzehak; r.rzehak@hzdr.de

Received 9 July 2012; Accepted 22 October 2012

Academic Editor: Yassin Hassan

Copyright © 2013 R. Rzehak and E. Krepper. This is an open access article distributed under the Creative Commons Attribution License, which permits unrestricted use, distribution, and reproduction in any medium, provided the original work is properly cited.

We investigate the present capabilities of CFD for wall boiling. The computational model used combines the Euler/Euler two-phase flow description with heat flux partitioning. Very similar modeling was previously applied to boiling water under high pressure conditions relevant to nuclear power systems. Similar conditions in terms of the relevant nondimensional numbers have been realized in the DEBORA tests using dichlorodifluoromethane (R12) as the working fluid. This facilitated measurements of radial profiles for gas volume fraction, gas velocity, liquid temperature, and bubble size. Robust predictive capabilities of the modeling require that it is validated for a wide range of parameters. It is known that a careful calibration of correlations used in the wall boiling model is necessary to obtain agreement with the measured data. We here consider tests under a variety of conditions concerning liquid subcooling, flow rate, and heat flux. It is investigated to which extent a set of calibrated model parameters suffices to cover at least a certain parameter range.

1. Introduction

Subcooled flow boiling occurs in many industrial applications where large heat transfer coefficients are required. However, the efficient heat transfer mechanism provided by vapor generation is limited at a point where liquid is expelled from the surface over a significant area. This occurs at the critical heat flux where the heat transfer coefficient begins to decrease with increasing temperature leading to an unstable situation. In this event a rapid heater temperature excursion occurs which potentially leads to heater melting and destruction. For a given working fluid, the critical heat flux depends on the flow parameters as well as the geometry of the flow domain. The verification of design improvements and their influence on the critical heat flux requires expensive experiments. Therefore, the supplementation or even the replacement of experiments by numerical analyses is of high interest in industrial applications.

In the past, many different empirical correlations for critical heat flux were developed and fitted to data obtained from experimental tests. These have been implemented mainly in purpose-specific 1D codes and applied for engineering design calculations. However, these correlations are valid only in the limited region of fluid properties, working conditions,

and geometry corresponding to the tests to which they were fitted. Using large look-up tables based on a great number of experiments, a significant range of fluid properties and working conditions can be covered. But this method is still limited to only that specific geometry for which they were developed. Independence of the geometry can only be achieved by the application of CFD methods. Existing CFD models, however, are not yet able to describe critical heat flux reliably. A precondition would be the complete understanding and simulation of boiling as a preliminary state towards critical heat flux.

For engineering calculations, currently the most widely used CFD approach to model two-phase flows with significant volume fractions of both phases is the Eulerian two-fluid framework of interpenetrating continua (see, e.g., [1–3]). In this approach, balance equations for mass, momentum, and energy are written for each phase, that is, gas and liquid, separately and weighted by the so-called volume fraction which represents the ensemble averaged probability of occurrence for each phase at a certain point in time and space. Exchange terms between the phases appear as source/sink terms in the balance equations. These exchange terms consist of analytical or empirical correlations, expressing the interfacial forces, as well as heat and mass fluxes, as functions of the average

flow parameters. Since most of these correlations are highly problem-specific, their range of validity has to be carefully considered and the entire model has to be validated against experiments.

For the case of boiling flows, where heat is transferred into the fluid from a heated wall at such high rates that vapor is generated, additional source terms describing the physics of these processes at the heated wall have to be included. A CFD wall boiling model following the lines of Kurul and Podowski [4, 5] was calibrated and validated by several authors, for example, Krepper et al. [6], against the experimental results of Bartolomej and Chanturiya [7]. In these tests, subcooled flow boiling of water at high pressure flowing upwards in a vertical pipe heated from the outside was investigated and measurements of the axial development of gas volume fraction, wall temperature, and cross-sectionally averaged liquid temperature were provided.

An application of continuing high interest is the thermal hydraulic flow in a nuclear reactor. However, typical flow conditions encountered in this application do not particularly lend themselves to experimental investigation. High pressure, high temperature, narrow channels, and small expected sizes of steam bubbles represent significant challenges for measurements. The use of refrigerants can greatly relieve this burden. In the French DEBORA tests [8, 9], dichlorodifluoromethane (R12) was used as the working medium. Advantages are that this allows a choice of test parameters that are more convenient for the measurement compared to the water/steam system at high pressure. The same vapor/liquid density ratio can be achieved at a much lower system pressure and the same Reynolds number can be achieved at a larger diameter of the heated pipe. This enables a measurement of radial profiles for gas volume fraction, temperature, liquid and gas velocities, and bubble sizes which allows a stringent validation of CFD models.

The applicability of CFD models to the DEBORA tests was recently studied in Krepper and Rzehak [10, 11] to demonstrate their general validity and identify specific weak points. By coupling a population balance approach to the wall boiling model, it was shown that a reasonable prediction of the measured radial profiles of void fraction, bubble size, liquid velocity, and liquid temperature could be achieved. Based on a review of the theoretical and experimental basis of correlations used in the wall boiling model, a careful assessment of the necessary recalibrations to describe the DEBORA tests was given. Most important are the bubble size at detachment and the nucleation site density. Within a limited range of conditions, different tests could be simulated with a single set of model parameters.

In the present work, the previous methodology is applied to a number of further test cases for varied conditions of liquid subcooling, flow rate, and heat flux. In this way, the robustness of the model formulation can be assessed and the (in)dependence of model parameters on the experimental conditions be investigated.

The paper is organized as follows. A brief summary of the DEBORA test facility and selected data is given in Section 2. In Section 3 the details of the models used for the simulations are described. The presentation is adapted from our previous

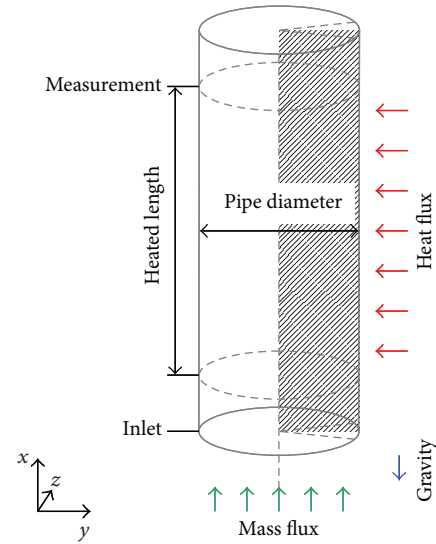


FIGURE 1: Sketch of the DEBORA test geometry.

work [10, 11] to make the paper self-contained. The setup of the simulations together with necessary calibrations of the models is described in Section 4. The results presented in Sections 5 and 6 show that the coupling of wall boiling with the population balance model enables the simulation both of the measured bubble size profiles and the gas volume fraction profiles provided the models are suitably calibrated. A discussion of the achievements so far and needs for further research are finally offered in Section 7.

2. The Investigated Experiments

2.1. Test Cases and Parameters. A detailed description of the DEBORA test facility can be found in Manon [8] and Garnier et al. [9]. In a vertical heated pipe having an inner diameter of 19.2 mm, dichlorodifluoromethane (R12) is heated over a pipe length of 3.5 m as sketched in Figure 1. The facility is operated at various pressures, flow rates, heat fluxes, and subcoolings. The radial profiles for gas volume fraction and gas velocity at the end of the heated length are measured by means of an optical probe. Furthermore, profiles of bubble size at this position are available. In addition, radial liquid temperature profiles as well as axial profiles of the wall temperature are measured by thermocouples. Unfortunately, temperature- and phase-related measurements are not both available for all experimental conditions.

Table 1 lists the parameters of the DEBORA tests selected for the present investigation. The first two cases, P26-G2-Q74-T16 and P26-G2-Q74-T18, have been considered previously, for example, in Yao and Morel [12, 13], Boucker et al. [14], and Krepper and Rzehak [10, 11]. The next three cases extend the range of inlet subcooling at the same flow rate and heat flux. The second series of four cases covers the same range of inlet subcooling but at different values of flow rate and heat flux. In the last group, the heat flux is varied at constant values of inlet subcooling and flow rate. For all

investigated tests, the system pressure is kept at a fixed value of $P = 2.62$ MPa. The question is to what extent the model is capable to reproduce the data under all of these conditions with as little recalibration as possible.

2.2. Fluid Properties and Dimensionless Groups. To compare results obtained for the DEBORA tests to other typical experiments and applications, where the working medium is water at different pressure levels, the values of the relevant dimensionless groups have to be considered. For boiling phenomena, the pipe Reynolds number, the liquid-to-gas density ratio, the Jakob number, and the Boiling number play a role. Focusing on the bubble dynamics furthermore the bubble Reynolds number, the Eötvös number, and the Morton number are important. Conditions at which the DEBORA tests were performed have been chosen to match values of these dimensionless parameters to those for water at conditions typical for pressurized water reactors. The replacement of water by R12 allows measurements at more convenient pressures and temperatures. Also advantageous is the possible increase of pipe diameter which enables the measurement of radial profiles.

For R12 liquid and vapor, the relevant material properties were taken from the National Institute of Standards and Technology (NIST) Standard Reference Database on Thermophysical Properties of Fluid Systems (<http://webbook.nist.gov/chemistry/fluid>). The saturation properties for the value of pressure considered, that is, $P = 2.62$ MPa, are listed in Table 2. Based on the NIST data, fluid property tables were generated and used in the calculations.

3. The Models

The general equations for diabatic two-phase flow in the Euler/Euler framework of interpenetrating continua have been reviewed in many places before (e.g., [1–3]). Therefore, we here focus on those issues that are particularly relevant for the present investigation as a starting point serves the subcooled boiling model implemented in ANSYS CFX which has been used in a large number of previous studies (e.g., Krepper et al. [6] and references therein).

The first major block is the wall boiling model describing vapor generation at the wall and transfer of sensible heat to the liquid. Here, the CFX model closely follows the heat flux partitioning approach of Kurul and Podowski [4, 5]. It has been emphasized in Krepper and Rzehak [10] that some of the commonly used correlations are not universally applicable but have to be recalibrated carefully to the specific conditions under investigation. The basis on which such a recalibration can be carried out for varying conditions is discussed. The final outcome of the calibration will be presented in Section 4.2.

A second issue is the modeling of interfacial area that determines the exchange of mass, momentum, and energy between the phases. For the bubbly flow regime, it is convenient to use an equivalent Sauter diameter and work with the bubble size. Obviously, in boiling flows the bubble size may change due to both condensation/evaporation and bubble

coalescence/breakup. The importance of taking into account the latter processes has been shown in Krepper et al. [11]. This may be achieved by a population balance model with a source at the wall, the size of the generated bubbles being given by the bubble detachment diameter as calculated from the wall boiling model. Since the rates for bubble coalescence and breakup depend sensitively on the turbulence, bubble-induced contributions to the turbulence have to be included as well. To simplify matters, the vapor bubbles are assumed to be at saturation temperature everywhere which is a rather good approximation except close to the critical heat flux.

Turbulent fluctuations are modeled by a shear stress turbulence (SST) model according to Menter [15, 16] applied to the liquid phase. This corresponds to a $k-\omega$ model near the walls and a $k-\varepsilon$ model far from the walls. The frequently used prescription of Sato et al. [17] for the bubble-induced turbulence has been replaced by including source terms in the turbulence equations following Politano et al. [18]. In addition, a wall function for boiling flows based on analogy to a rough wall is employed, which could be shown in Krepper and Rzehak [10] to give an improved prediction of the velocity profiles.

For momentum exchange between the phases, finally, lift and turbulent dispersion forces are included in the model in addition to the ubiquitous drag force. For adiabatic flows, there is in addition also a force that pushes a bubble translating in an otherwise quiescent liquid parallel to a wall in close proximity away from this wall. Different models for this so-called wall force were investigated, but the influence turned out to be small. Therefore, in the present study, this force was neglected. In general the applicability of a wall force to flow boiling should be investigated further.

3.1. Modeling of Boiling at a Heated Wall. In boiling, heat is transported from the hot wall to the fluid by several different mechanisms. On parts of the wall, where no bubbles reside, heat flows directly to the subcooled liquid in the same way as that in single-phase flow. On parts of the wall where bubbles grow, heat is consumed by the vapor generation which occurs at the so-called nucleation sites. Moreover, there is a liquid mixing mechanism due to the bubbles which leave the wall. As a consequence of the recirculation around the detaching bubble, a cold liquid from the bulk of the flow is brought into contact with the hot wall which leads to additional cooling. This mechanism, which is obviously not present in single-phase flows, is termed quenching.

Accordingly, the given external heat flux Q_{tot} , applied to the heated wall, is written as a sum of three parts:

$$Q_{\text{tot}} = Q_C + Q_Q + Q_E, \quad (1)$$

where Q_C , Q_Q , and Q_E denote the heat flux components due to single-phase turbulent convection, quenching, and evaporation, respectively. The individual components in this heat flux partitioning are then modeled as functions of the wall temperature and other local flow parameters. Once this is accomplished, (1) can be solved iteratively for the local wall temperature T_w , which satisfies the wall heat flux balance. Denoting the fraction of area influenced by the bubbles as

TABLE 1: System parameters for the selected test cases, $P = 2.62$ MPa.

	Mass flow rate ($\text{kg m}^{-2} \text{s}^{-1}$)	Wall heat flux (kW m^{-2})	Inlet subcooling (K)	Inlet temperature ($^{\circ}\text{C}$)	Outlet equilibrium vapor quality
P26-G2-Q74-T16			15.7	70.7	0.0848
P26-G2-Q74-T18			17.9	68.5	0.058
P26-G2-Q74-T20	2000	74	19.8	66.6	0.0324
P26-G2-Q74-T26			25.7	60.8	-0.0205
P26-G2-Q74-T28			27.6	58.3	-0.0719
P26-G3-Q118-T16			16.0	70.7	0.1056
P26-G3-Q118-T20	3000	118	20.2	66.2	0.0483
P26-G3-Q118-T24			24.2	62.2	-0.0027
P26-G3-Q118-T28			27.6	58.3	-0.0523
P26-G3-Q129-T29		129	28.6	57.9	-0.0334
P26-G3-Q139-T28	3000	139	27.8	58.6	0.0055
P26-G3-Q148-T28		148	28.3	58.2	0.0259

TABLE 2: Material properties of R12 and water at $P = 2.62$ MPa.

Material	R12
Pressure condition (MPa)	2.62
Saturation temperature (K)	360
Surface tension (N m^{-1})	0.00180
Enthalpy of vaporization (J kg^{-1})	293×10^3
Vapor density (kg m^{-3})	0.172×10^3
Liquid density (kg m^{-3})	1.02×10^3
Liquid specific heat capacity ($\text{J kg}^{-1} \text{K}^{-1}$)	1.42×10^3
Liquid viscosity ($\text{kg m}^{-1} \text{s}^{-1}$)	89.5×10^{-6}
Liquid thermal conductivity ($\text{W m}^{-1} \text{K}^{-1}$)	0.0457

A_W , the heat flux components are expressed as discussed in the following.

The turbulent convection heat flux is calculated in the CFX model version (see Wintterle [19]) in much the same way as for a pure liquid flow without boiling but multiplied by the fraction of area unaffected by the bubbles; that is,

$$Q_C = (1 - A_W) h_C (T_W - T_L). \quad (2)$$

Here h_C is the heat transfer coefficient which is written using the temperature wall function $T^+(y^+)$ known from Kader [20] as

$$h_C = \frac{\rho C_P u_\tau}{T^+}, \quad (3)$$

where nondimensional variables (indicated by superscript “+”) and the friction velocity u_τ are defined as usual. Note that (2)-(3) may be evaluated at any location y , provided it is used consistently whenever a variable depends on position.

Q_Q is represented in terms of the quenching heat transfer coefficient h_Q :

$$Q_Q = A_W h_Q (T_W - T_L). \quad (4)$$

A grid independent solution for Q_Q is obtained by evaluating the nondimensional temperature profile at a fixed value of y^+ .

The evaporation heat flux Q_E is obtained via the evaporation mass flux at the wall:

$$Q_E = \dot{m}_W H_{LG}, \quad (5)$$

where H_{LG} is the latent heat of evaporation and the generated vapor mass \dot{m}_W is expressed in terms of the bubble diameter at detachment d_W , bubble generation frequency f , and nucleation site density N as

$$\dot{m}_W = \rho_G \frac{\pi}{6} d_W^3 f N. \quad (6)$$

The bubble size at detachment is known to depend on a large number of variables, namely, the liquid subcooling, the flow rate, the heat flux, the wall superheat, the fluid properties at the system pressure, and the contact angle between the fluid and the wall. Although several differing proposals have been made (e.g., Ünal [21], Winterton [22], Zeng [23], Kandlikar et al. [24], Klausner et al. [25], Situ et al. [26], Basu et al. [27], and references therein), a generally valid empirical or theoretical correlation covering all of these dependencies is not available at present.

Some more readily usable results are possible for restricted conditions, for example, for water at atmospheric pressure. However, for the present application to R12, unfortunately even such more specialized results are not available. Yet more complex is the dependence on the contact angle, which varies significantly not only with the material combination of working fluid and heating surface but also depending strongly on ill-characterized factors like surface roughness and contaminants (e.g., Griffith and Wallis [28] and Hong et al. [29]). For the present application, the value of the contact angle is not available.

With respect to the other variables, it may be noted that for each individual test, the values of flow rate and heat flux are constant along the pipe. The available data on axial dependence of the wall superheat (cf., Section 5) suggest that this is also the case for the wall superheat except probably close to the beginning of the heated section. Thus further



FIGURE 2: Sketch of bubble nucleus.

simplification may be sought by fixing these conditions and focusing on the dependence with respect to the liquid subcooling.

Common practice in engineering simulations of flow boiling largely relies on an experimental investigation of the bubble size at detachment for water at atmospheric pressure by Tolubinsky and Kostanchuk [30], where the observed dependence on the liquid subcooling can be fitted to a correlation

$$d_W = d_{\text{ref}} e^{-(T_{\text{sat}} - T_L)/\Delta T_{\text{ref}d}}. \quad (7)$$

Here again T_L is obtained by evaluating the nondimensional temperature profile of Kader [20] at a fixed value of y^+ . The values of the fit parameters d_{ref} and $\Delta T_{\text{ref}d}$ then must be expected to depend on all the other variables. By suitable calibration of these fit parameters, it has been shown for a number of systems that reasonable agreement with data can be obtained [6, 10].

The approach taken in the present investigation is to allow a different calibration for different values of flow rate and heat flux. Eventually it will turn out that within certain limits the same calibration can be used even for different conditions. Detailed values will be given in Section 4.2.1.

Concerning the nucleation site density, most available correlations are expressed in the form of power laws depending on the wall superheat as

$$N = N_{\text{ref}} \left(\frac{T_W - T_{\text{sat}}}{\Delta T_{\text{ref}N}} \right)^P. \quad (8)$$

Notably, the only variable that appears is the wall superheat, although a recent compilation [31] shows that vastly different parameter values are required to match different data sets. This may be rationalized based on the microscopic theory of nonclassical heterogeneous nucleation [32]. Accordingly, bubble growth is initiated from preexisting nuclei trapped in surface corrugations of micrometer size as sketched schematically in Figure 2.

An important variable characterizing the thermodynamic stability of such nuclei is the local equilibrium temperature at

the curved liquid vapor interface [33] which may be roughly identified with the wall superheat; namely,

$$T_W - T_{\text{sat}} = \frac{2}{R_n} \frac{\sigma T_{\text{sat}}}{\rho_G H_{LG}}. \quad (9)$$

Due to the small spatial scales involved, this process may be expected to be independent of other parameters like liquid subcooling, flow rate, and heat flux. This provides some rationale for the appearance of the wall superheat as the only variable in correlations for the nucleation site density.

The diversity of specific expressions for these correlations is likely related to the geometry of corrugations on a given heating surface which depends strongly on the processes that were used to finish the surface. These processes are very diverse and in most boiling experiments not specifically controlled. Moreover, a characterization of the resulting surface topography is rarely available.

Parameter variations showed that the assumed nucleation site density has almost no influence on the calculated liquid temperature, a small influence on the calculated gas volume fraction, but a strong influence on the calculated wall superheat $T_W - T_{\text{sat}}$. Due to the common case of missing information on the nucleation site density, the approach taken in the present investigation is to make use of the measured wall temperature to calibrate the correlation equation (8). Since this calibration depends only on properties of the heating surface, it can then be used for all different conditions, as will be corroborated by the results. Detailed values will be given in Section 4.2.1.

In terms of bubble detachment diameter and nucleation site density given by (7) and (8), the wall area fraction influenced by vapor bubbles A_W is given by

$$A_W = \pi \left(a \frac{d_W}{2} \right)^2 N. \quad (10)$$

Here, a is the so-called bubble influence factor, for which a value of 2 is commonly used [4, 5]. Direct experimental evidence concerning this quantity is rather scarce. Probably the most relevant source is Han and Griffith [34] who in some ‘‘rough’’ experiments determined the hydrodynamic disturbance caused by lifting a spherical particle from a horizontal surface and found that it has a range of twice the size of the particle. A similar size has been claimed by Cieslinski et al. [35] from PIV measurement of the flow field around departing bubbles, although the quality of the images presented is rather poor.

Since $A_W = 1$ corresponds to the case where the whole surface is under the influence of bubbles, A_W as calculated by (10) has to be limited to values smaller than this limit. Moreover, it should be kept in mind that already as A_W approaches 1, the assumptions of the model are not really satisfied anymore.

The bubble detachment frequency f is given according to Cole [36] as a function of the detachment size d_W as

$$f = \sqrt{\frac{4g(\rho_L - \rho_G)}{3C_D d_W \rho_L}}. \quad (11)$$

Relations of this type have been reviewed critically by Ivey [37] and Ceumern-Lindenstjerna [38].

The quenching heat transfer coefficient is calculated using the analytical solution for one-dimensional transient conduction, as suggested by Mikic and Rohsenow [39]:

$$h_Q = \frac{2}{\sqrt{\pi}} f \sqrt{t_{\text{wait}} k_L \rho_L C_{P,L}}, \quad (12)$$

where t_{wait} is the waiting time between the departure of a bubble and the appearance of the next one at the same nucleation site. A simple assumption by Kurul and Podowski [4, 5] is adopted here, too, where the waiting time takes a fixed fraction of the bubble departure period:

$$t_{\text{wait}} = \frac{0.8}{f}. \quad (13)$$

Data supporting this simple estimate come from the work of del Valle and Kenning [40] which, however, is limited to the regime where the heat flux is 75% of the critical heat flux and larger.

3.2. Population Balance Approach to Bubble Size Distribution.

To describe polydispersed flows within a purely Eulerian approach, a number of different (multiple) bubble size groups $i = 1 \dots M$ is considered, each representing bubbles of typical size d_i . The fraction of gas volume contained in each bubble size group is denoted as α_i so that the total gas volume fraction is given by

$$\alpha_G = \sum_{i=1}^M \alpha_i. \quad (14)$$

It is useful to also define occupation numbers $f_i = \alpha_i/\alpha_G$ giving the contribution of each size group to the total gas volume fraction. Obviously we then have $\sum_i f_i = 1$.

For each size group, the equation of mass conservation assumes the form

$$\frac{\partial}{\partial t} (\alpha_i \rho_G) + \nabla (\alpha_i \rho_G \mathbf{u}_G) = \Gamma_i^{\text{topo}} + \Gamma_i^{\text{phase}}, \quad (15)$$

where the right-hand side gives the net source of mass for group i which results from topological changes due to coalescence and breakup as well as phase change due to condensation and evaporation. Models for these two contributions will be discussed in the following subsections.

For the homogeneous MUSIG model only one momentum and energy equation for the total amount of vapor is considered as well as the conservation equations of the liquid of course. In these equations, the total gas volume fraction α_G is calculated according to (14) above. In addition, also the bubble size d_B appears which is taken in the Sauter sense representing the interfacial area $A_I = 6\alpha_G/d_B$. In order to preserve this interpretation, d_B is calculated from the occupation number and bubble size for each group as

$$d_B = \left(\sum_{i=1}^M \frac{f_i}{d_i} \right)^{-1}. \quad (16)$$

The advantage of the homogeneous MUSIG approach is that a large number of bubble size groups can be considered while keeping the computational effort within reasonable bounds. On the other hand, profound effects of bubble size are missed entirely like, for example, the change in the sign of the lift force as discussed in Section 3.4.2. To capture such phenomena, provision has to be made that bubbles of different size may move with different velocities. To overcome these limitations, the inhomogeneous MUSIG model [41, 42] was developed and applied to boiling phenomena in Krepper et al. [11]. For the present investigation, however, it will be seen that this more elaborate treatment is not needed.

3.2.1. Coalescence and Breakup. The net mass source for size group i due to bubble coalescence and breakup can be expressed as the sum of bubble birth rates due to the breakup of larger bubbles from groups $j > i$ to group i and coalescence of smaller bubbles from size groups $j < i$ to group i as well as bubble death rates due to breakup of bubbles from size group i to smaller bubbles in groups $j < i$ and the coalescence of bubbles from size group i with bubbles from any other group to even larger ones which belong to groups $j > i$. That is,

$$\Gamma_i^{\text{topo}} = B_i^{\text{break}} - D_i^{\text{break}} + B_i^{\text{coal}} - D_i^{\text{coal}}. \quad (17)$$

The birth and death rates in turn are commonly expressed in terms of the coalescence and break-up kernels such that

$$\begin{aligned} B_i^{\text{break}} &= \rho_G \alpha_G \sum_{j>i} b(m_j, m_i) f_j \frac{m_i}{m_j} \Delta m_i, \\ D_i^{\text{break}} &= \frac{1}{2} \rho_G \alpha_G \sum_{j<i} b(m_i, m_j) f_i \Delta m_j, \\ B_i^{\text{coal}} &= \frac{1}{2} \rho_G^2 \alpha_G^2 \sum_{j \leq i} \sum_{k \leq i} c(m_j, m_k) X_{jki} f_j f_k \frac{m_j + m_k}{m_j m_k}, \\ D_i^{\text{coal}} &= \rho_G^2 \alpha_G^2 \sum_j c(m_i, m_j) f_i f_j \frac{1}{m_j}. \end{aligned} \quad (18)$$

Here X_{jki} is an approximation to the delta-function $\delta(m_j + m_k - m_i)$. For the break-up and coalescence kernel functions b and c , the commonly used break-up models according to Luo and Svendsen [43] and the coalescence models of Prince and Blanch [44] are applied in the present work but were adjusted by factors to match the measured bubble sizes. In this way the applicability of the general framework is demonstrated, but of course further developments will be necessary to improve the physical models and overcome such tuning procedures.

3.2.2. Condensation and Evaporation Including Boiling at the Wall. When condensation or evaporation occurs, the volume fraction in size group i changes for two reasons: (i) mass is transferred directly between the bubbles and the liquid and (ii) since due to this direct mass transfer, the bubbles are shrinking or growing, they may subsequently belong to a different size group.

Written as a source term for size group i the direct mass transfer to the liquid is given by

$$\tilde{\Gamma}_i = -\frac{A_{L,i}}{H_{LG}} h_{L,i} (T_L - T_{\text{sat}}), \quad (19)$$

where similar to previous work [10] the assumption has been made that the gas is at saturation temperature. The total source terms for size class i including also the ensuing change of bubble size, that is, Γ_i^{phase} in (15), have been derived recently by Lucas et al. [45] as

$$\Gamma_i^{\text{phase}} = \begin{cases} \frac{m_i}{m_i - m_{i-1}} \tilde{\Gamma}_i \\ -\frac{m_i}{m_{i+1} - m_i} \tilde{\Gamma}_{i+1} & \text{for } \tilde{\Gamma}_i < 0, \text{ that is, condensation,} \\ \frac{m_i}{m_i - m_{i-1}} \tilde{\Gamma}_{i-1} \\ -\frac{m_i}{m_{i+1} - m_i} \tilde{\Gamma}_i & \text{for } \tilde{\Gamma}_i > 0, \text{ that is, evaporation,} \end{cases} \quad (20)$$

where $m_i = \rho \pi d^3 / 6$ is the mass of each bubble in size group i . Basing the calculation on bubble mass rather than size for compressible flows has the advantage that since mass is conserved, no extra terms arise in the equations. Conversion to the corresponding bubble size which depends on the local density can be done straight forwardly as needed. For incompressible flows, no differences between mass- and size-based groups arise.

In principle $\tilde{\Gamma}_i$ should be evaluated with the group size d_i , but for practical reasons, an approximation is used where a direct transfer term $\tilde{\Gamma}_j$ is calculated according to (21) only for each velocity group j using the Sauter mean diameter of (16) and the area based fraction thereof is used for $\tilde{\Gamma}_i$; that is,

$$\tilde{\Gamma}_i = \frac{A_{L,i}}{A_{L,j}} \tilde{\Gamma}_j. \quad (21)$$

In this way, the size dependency of the factor $A_{L,i}$ in (21) is treated exactly, but that of the factor $h_{L,i}$ is not. The liquid side heat transfer coefficient, finally, is calculated according to Ranz and Marshall [46] as

$$h_L = \frac{k_L}{d_B} Nu = \frac{k_L}{d_B} (2 + 0.6 Re^{1/2} Pr^{1/3}). \quad (22)$$

In addition to the source terms for the continuity equations for the bubble size groups, there is also a mass source for the liquid phase continuity equation which is given by

$$\Gamma_L = -\sum_i \tilde{\Gamma}_i. \quad (23)$$

Moreover, corresponding secondary sources appear in the momentum and energy equations.

A validation of the above procedure against experimental data has been given by Krepper et al. [47].

To include the generation of vapor bubbles at the wall, an additional source term, S_{rpi} , is included in (19) following [48]. This source term applies only to the equation corresponding to the size group whose diameter is the closest to the bubble detachment diameter d_W . It is given by the evaporation mass flux computed in the wall heat partitioning distributed evenly throughout the grid cells adjacent to the heated wall; that is,

$$S_{\text{rpi}} = \dot{m}_W \frac{S}{V}, \quad (24)$$

where \dot{m}_W is given by (6) and S and V are wall surface area and volume of the corresponding grid cell, respectively.

3.3. Modeling of Turbulence in a Two-Phase Flow. Liquid-phase turbulence is modeled by a shear stress transport (SST) model [15, 16] with additional source terms describing the effects of the bubbles as detailed in Section 3.3.1. The reverse effect exerted by the turbulent fluctuations on the bubbles is taken into account by the turbulent dispersion force as will be described in Section 3.4.3. In addition, a turbulent wall function for boiling flows was employed [10] which is summarized in Section 3.3.2. Turbulence in the gas phase is neglected based on the small density as argued in Troshko and Hassan [49].

3.3.1. Bubble-Induced Turbulence. The effects of the dispersed gas bubbles on the turbulence in the continuous liquid phase are modeled by introducing appropriate source terms in the k - and ε - or ω -equations.

The bubble-induced source S_L^k in the k -equation describes additional generation of turbulent kinetic energy due to the bubbles. Assuming that all energy lost by the bubble due to drag is converted into turbulent kinetic energy in the wake of the bubble, this source can be calculated as

$$S_L^k = |\mathbf{F}^{\text{drag}} \cdot (\mathbf{u}_G - \mathbf{u}_L)|, \quad (25)$$

where \mathbf{F}^{drag} is the drag force given by (31) and $\mathbf{u}_G - \mathbf{u}_L$ is the relative velocity.

The bubble-induced source S_L^ε in the ε -equation describes additional dissipation of turbulent kinetic energy due to the bubbles. Following the same dimensional reasoning used in deriving the single phase ε -equation, this term is postulated proportional to the source in the k -equation divided by a suitable time scale τ ; that is,

$$S_L^\varepsilon = C_{\varepsilon 3} \frac{S_L^k}{\tau}. \quad (26)$$

Unfortunately no theoretical derivation is available for the time scale and a number of different expressions have been proposed. For the present simulation, we follow Lee et al. [50], Pfleger and Becker [51], and Politano et al. [18] who assumed that the usual turbulence time scale may be used; that is,

$$\tau = \frac{k}{\varepsilon}. \quad (27)$$

The coefficient $C_{\varepsilon 3} = 1.92$ was found to give satisfactory results.

An equivalent source term for the ω -equation is derived from S_L^k and S_L^ε as

$$S_L^\omega = \frac{1}{C_\mu k} S_L^\varepsilon - \frac{\omega}{k} S_L^k, \quad (28)$$

where $C_\mu = 0.09$, a standard parameter in the k - ε turbulence model. In the SST model, this term is used independent of the blending function since it should be effective throughout the fluid domain.

3.3.2. Turbulent Wall Function for Boiling Flow. A wall function for boiling flow is obtained by considering that the presence of the bubbles on the wall forces the liquid into a similar flow pattern as that observed in single-phase turbulent flow with wall roughness (e.g., Ramstorfer et al. [52] and Končar and Borut [53]). The latter is described by a modified law of the wall [54, 55]

$$\frac{u}{u_\tau} = \frac{1}{\kappa} \ln\left(\frac{y}{\delta}\right) + B = \frac{1}{\kappa} \ln\left(\frac{y}{s}\right) + B^*, \quad (29)$$

where $u_\tau = \sqrt{(\tau_w/\rho)}$ is the friction velocity, $\delta = \mu/(\rho u_\tau)$ is the viscous length scale, s is the hydrodynamic roughness length scale, and $\kappa \approx 0.41$ is the von Karman constant. For flow over smooth walls, $B \equiv \text{const} \approx 5.5$, while for flow over rough walls, B^* is a function of s/δ which in the limit of large s , that is, for the so-called fully rough walls, tends to a constant value of 8.5.

The hydrodynamic roughness s may be related directly to the bubble size and nucleation site density as [10]

$$s = C_S N d_W^3. \quad (30)$$

The constant of proportionality is not known from theoretical considerations at present, but a value of $C_S = 1.0$ has been found to yield good results.

As shown in [10], the representation of radial velocity profiles is greatly enhanced by employing this two-phase boiling wall function over the often used single-phase wall function.

3.4. Modeling of the Momentum Transfer. For momentum exchange between the phases, the Ishii and Zuber [56] drag law was used. Furthermore, a lift force with sign reversal according to Tomiyama et al. [57] and a Favre averaged turbulence dispersion force [58] were included. As noted in Krepper and Rzehak [10], the effect of an additional wall force is small. Therefore, in the present study this force was neglected. In the following expressions, the forces for the dispersed gaseous phase are given.

3.4.1. Drag Force. The volumetric source of gaseous momentum due to drag exerted by the liquid is given by

$$\mathbf{F}^{\text{drag}} = -\frac{3}{4d_B} C_D \rho_L \alpha_G |\mathbf{u}_G - \mathbf{u}_L| (\mathbf{u}_G - \mathbf{u}_L). \quad (31)$$

The drag coefficient C_D is calculated according to Ishii and Zuber [56] considering three different shape regimes as

$$C_D = \max(C_{D,\text{sphere}}, \min(C_{D,\text{ellipse}}, C_{D,\text{cap}})), \quad (32)$$

where

$$\begin{aligned} C_{D,\text{sphere}} &= \frac{24}{\text{Re}} (1 + 0.1 \text{Re}^{0.75}), \\ C_{D,\text{ellipse}} &= \frac{2}{3} \sqrt{\text{Eo}}, \\ C_{D,\text{cap}} &= \frac{8}{3}. \end{aligned} \quad (33)$$

3.4.2. Lift Force. A lift force due to interaction of the bubble with the shear field of the liquid was first introduced to two-fluid simulations by Zun [59]. The corresponding momentum source is given by

$$\mathbf{F}^{\text{lift}} = -C_L \rho_L \alpha_G (\mathbf{u}_G - \mathbf{u}_L) \times \text{rot}(\mathbf{u}_L). \quad (34)$$

The classical lift force, which has a positive coefficient C_L , acts in the direction of decreasing liquid velocity. In case of co-current upwards pipe flow this is the direction towards the pipe wall. Experimental [57] and numerical [60] investigations showed that the direction of the lift force changes its sign, if a substantial deformation of the bubble occurs. From the observation of the trajectories of single bubbles rising in simple shear flow of a glycerol water solution, the following correlation for the lift coefficient was derived:

$$C_L = \begin{cases} \min[0.288 \tanh(0.121 \text{Re}), f(\text{Eo}_\perp)] & \text{Eo}_\perp < 4, \\ f(\text{Eo}_\perp) & \text{for } 4 < \text{Eo}_\perp < 10, \\ -0.27 & 10 < \text{Eo}_\perp, \end{cases}$$

with $f(\text{Eo}_\perp) = 0.00105 \text{Eo}_\perp^3 - 0.0159 \text{Eo}_\perp^2 - 0.0204 \text{Eo}_\perp + 0.474$.

(35)

This coefficient depends on the modified Eötvös number given by

$$\text{Eo}_\perp = \frac{g(\rho_L - \rho_G) d_\perp^2}{\sigma}. \quad (36)$$

Here d_\perp is the maximum horizontal dimension of the bubble. It is calculated using an empirical correlation for the aspect ratio by the following equation [61]:

$$d_\perp = d_B \sqrt[3]{1 + 0.163 \text{Eo}^{0.757}}. \quad (37)$$

For the water-air system at normal conditions, C_L changes its sign at $d_B = 5.8$ mm which was confirmed by investigations of polydispersed upward vertical air/water bubbly flow [62, 63]. For R12 this value is decreased substantially to about 1.0 mm at 2.62 MPa.

3.4.3. *Turbulent Dispersion Force.* The turbulent dispersion force is the result of the turbulent fluctuations of liquid velocity. Burns et al. [58] derived an expression by Favre averaging the drag force as

$$\mathbf{F}^{\text{disp}} = -\frac{3}{4}C_D \frac{\alpha_L}{d_B} (\mathbf{u}_G - \mathbf{u}_L) \frac{\mu^{\text{eff}}}{\sigma^{\text{TD}}} \left(\frac{1}{\alpha_L} + \frac{1}{\alpha_G} \right) \nabla \alpha_G. \quad (38)$$

Here, $\sigma^{\text{TD}} = 0.9$ is an empirical parameter.

As noted in Krepper and Rzehak [10], the effect of an additional wall force is small. Therefore, in the present study, this force was neglected.

4. Model Setup

The models described in the previous section present a rather general framework that can be specialized to the simulation of any subcooled flow boiling problem. The necessary specifications to simulate the DEBORA test cases will now be described. These comprise prescription of flow domain and boundary conditions and specification of grid and bubble classes as well as calibration of model parameters.

The simulations are performed by ANSYS CFX 13. For details of the numerical procedures, we refer to the user guide [64].

4.1. *Geometry and Boundary Conditions.* The tests were simulated in a quasi-2D cylindrical geometry, that is, a narrow cylindrical sector with symmetry boundary conditions imposed on the side faces. The validity of this simplification has been verified by grid resolution studies and by comparison to a 3D simulation representing a 60° sector of the pipe.

At the upstream end of the pipe, an unheated flow development zone has been added to obtain at the beginning of the heated section a fully developed turbulent flow that is independent of the detailed conditions imposed at the inlet. The required length of this flow development zone was determined by examining the development of velocity and temperature as well as turbulent kinetic energy and dissipation rate to ensure that these did not vary anymore in the axial direction before entering the heated section. At the outlet at the top, a pressure boundary condition was imposed.

On the heated walls, boundary conditions for mass and energy equations are provided by the heat flux partitioning discussed in Section 3.1. It remains to specify boundary conditions for the gas and liquid momentum equations. Since the gas volume fraction in our model represents bubbles that have detached from the wall, an appropriate boundary condition for the gas phase is the free slip condition. For the liquid phase, we argue that bubbles which have not left the wall are still attached to their respective nucleation site. Hence they restrain the liquid motion in the same way as the solid wall itself does. Therefore, we choose a no-slip condition for the liquid phase. While this issue does not appear to have received due attention in the literature, the results to be presented justify our choice as preliminary working solution until a more thorough investigation becomes available.

All of these two-phase flow simulations have been carried out on a quite coarse grid for which the center of the grid

TABLE 3: Parameters used for the bubble detachment model.

	T_{AV} (K)	T_{sub} (K)	$d_w(R)$ (mm)
P26-G2-Q74-T16	359.5	0.1	0.247
P26-G2-Q74-T18	359.2	0.35	0.237
P26-G2-Q74-T20	359.0	0.62	0.228
P26-G2-Q74-T26	356.4	3.23	0.165
P26-G2-Q74-T28	351.6	8.03	0.154
P26-G3-Q118-T16	359.3	0.3	0.152
P26-G3-Q118-T20	358.5	1.1	0.152
P26-G3-Q118-T24	355.9	3.7	0.134
P26-G3-Q118-T28	352.5	7.1	0.124
P26-G3-Q129-T29	353.8	5.8	0.142
P26-G3-Q139-T28	355.7	3.9	0.163
P26-G3-Q148-T28	356.4	3.3	0.161

cells adjacent to the wall has a nondimensional coordinate of $y^+ \approx 200$. For the test P26-G2-Q74-T16, a grid refinement study was performed which showed no change of the results until this value of y^+ has decreased to about 70. For still smaller values, no convergence could be achieved. This is a well-known problem of the Kurul and Podowski [4, 5] wall boiling model where all vapor generation occurs in the grid cell adjacent to the wall.

4.2. Calibration of Parameters

4.2.1. *Wall Boiling Model.* The necessity to recalibrate the boiling model parameters to the working fluid and heating surface of the experiment was discussed in a previous study [10].

For the model of bubble detachment size in (7), we proceed as follows. The outermost measurement points of the experimental bubble size profiles are taken as representative of the detachment size. The liquid subcooling at the measurement location is determined from the averaged measured liquid temperature profile for the test series P26-G2-Q74-Txx. For the two other series P26-G3-Q118-Txx and P26-G3-Qxx-T28, unfortunately no temperature measurements are available. Hence, the averaged liquid subcooling was determined from preliminary CFD calculations. The values of detachment size and liquid subcooling for all tests are listed in Table 3. For each of the three series of tests, values for the reference bubble size, d_{ref} , and the reference subcooling, $\Delta T_{\text{ref},d}$, were then found by fitting the expression (7) to the values of Table 3. The resulting correlations are shown in Figure 3 and the derived model parameters are collected in Table 4. It may be seen that the calibration parameters depend on the flow rate but not on the heat flux.

As discussed in Section 3.1 calibration of the model for nucleation site density in (8) is possible by matching the measured axial profiles of wall superheat. Such profiles are available only for the test series P26-G2-Q74-Txx, but as discussed in Section 3.1, the nucleation site density may be expected to depend on parameters subcooling, flow rate, and heat flux only indirectly through the wall superheat.

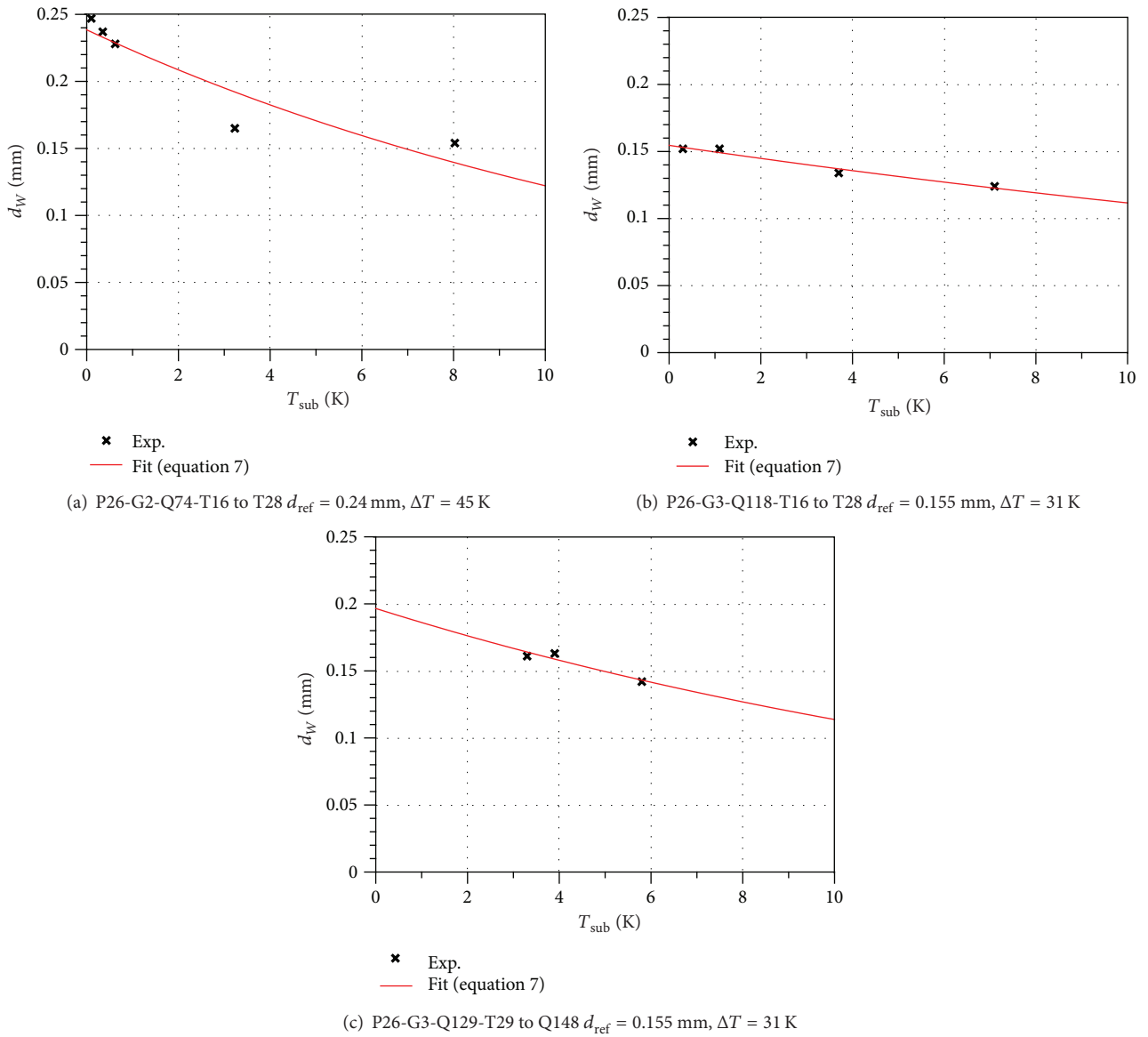


FIGURE 3: Bubble size at detachment according to (7) fitted to measurements.

TABLE 4: Adapted parameters for different test series.

Tests	T_{sub}	Equation (7) and Figure 3		Equation (8) and Figure 4		F_B	F_C
		d_{ref}	ΔT_{refd}	N_{ref}	ΔT_{refN}		
P26-G2-Q74-Txx	28, 26, 20, 18, 16	0.24	45	$3.0e + 7$	10	0.03125	0.5
	28,					0.015	1.0
P26-G3-Q118-Txx	24,	0.155	31	$3.0e + 7$	10	0.015	1.0
	20,					0.03125	1.0
	16					0.03125	0.5
P26-G3-Q129-T28						0.0075	1.0
Q139,	28	0.155	31	$3.0e + 7$	10	0.0075	1.0
Q148						0.0	1.0

Moreover, the sensitivity of the final results with respect to the exponent $p = 1.85$ is rather low; so only the prefactor N_{ref} will be adjusted for a value of the reference temperature $\Delta T_{\text{refN}} = 10$ K. Wall temperature profiles for two selected tests, P26-G2-Q74-T18 and P26-G2-Q74-T26, are shown in Figure 4. A value of $N_{\text{ref}} = 3.0e7 \text{ m}^{-2}$ gives good agreement with the respective data.

4.2.2. Coalescence and Break-Up Models. In the present work, bubble coalescence and breakup are described by the models proposed by Prince and Blanch [44] and by Luo and Svendsen [43]. To obtain agreement with the measurements, efficiency factors F_C and F_B were introduced and calibrated to match the measured radial bubble size profiles. Bubble size profiles for selected tests and several values of the calibration parameters F_C and F_B are shown in Figure 5. The procedure was successful so far as a good match could be obtained in all cases, but a different set of calibration parameters was necessary to this end (see Table 4). Therefore, this procedure has to be considered only as a first step and further model development needs to be done.

As discussed in Section 3.4.2, the lift force changes its sign at a certain bubble size. The value of this critical bubble size can be calculated as 1.0 mm for the material properties of R12 at a pressure of 2.62 MPa. Examination of the measured bubble sizes shows that these are lower than the critical value for all of the tests investigated here. Therefore, it is possible to use the simpler and computationally less expensive homogeneous MUSIG approach. For each test considered here, an equidistant bubble size discretization employing 15 size groups in the range of 0 to 1.5 mm was applied.

5. Reference Simulations

In this section, a more detailed discussion is given for a few selected tests, namely, P26-G2-Q74-T16, P26-G3-Q118-T16, and P26-G3-Q148-T28. As summarized in Table 1, these tests have the same pressure but different subcooling, flow rate, and heat flux. A comparison of measured and calculated profiles for gas volume fraction, gas velocity, bubble size, and liquid temperature at the end of the heated length ($x = 3.5$ m) are shown in Figures 6, 7, and 8. Unfortunately, temperature measurements are available only for the first of these.

For the first two test cases, experimental gas volume fractions exhibit s-shaped profiles with an inflexion point which is absent for the third test case. In the simulations, the gas volume fraction profiles for all cases have a slope that decreases monotonously from the wall towards the center of the pipe. Cross-sectionally averaged values agree with the experimental ones for the first two cases but deviate for the last one. There does not appear to be a simple explanation for these deviations at hand. Gas velocities (part b of the figures) are slightly overpredicted for all cases. Average bubble size profiles (part c of the figures) agree with the data to a varying degree which is not surprising due to the rather crude modeling approach for coalescence and break-up rates. The calculated bubble size distributions at several

radial positions (part d of the figures) show a rather narrow distribution near the pipe wall which broadens towards the center. This is due to the present modeling where all bubbles are generated with the same value of d_W at the wall. Where available, the temperature profiles show good agreement between simulation and experiment.

For all test cases, overall reasonable agreement between experiment and simulation is found. The relative deviations in all other aspects of the comparison are in the 20 to 30% range which is comparable to other state-of-the-art investigations in the field.

6. Parametric Variations

In this section, tests in two series with varying subcooling for otherwise fixed parameters are compared, namely, P26-G2-Q74-T16 to P26-G2-Q74-T28, P26-G3-Q118-T16 to P26-G3-Q118-T28, and P26-G3-Q129-T28 to P26-G3-Q148-T28. The resulting changes in the profiles for gas volume fraction, bubble size, and liquid temperature at the end of the heated length ($x = 3.5$ m) as the subcooling, considering the heat flux is varied, are shown in Figures 9, 10, and 11, respectively, where the left column gives the measured and the right columns the calculated values. For the latter two series, unfortunately no temperature measurements are available.

Thermal conditions in the liquid at the measurement location depend on all three parameters inlet subcooling, flow rate, and heat flux. The calculated temperature profiles compare quite well with the experimental ones for the case where the latter are available. As a reference the calculated profiles are shown also for the two cases where data are not provided.

For all tests, the bubble size increases with increasing the distance from the wall despite the fact that the bulk liquid is subcooled. Clearly this must be due to coalescence of the bubbles. This phenomenon could not be captured by the monodisperse model approach of Krepper and Rzehak [10]. For both test series upon decreasing the subcooling, a strong increase of bubble size is observed in the center of the pipe while the detachment size changes only relatively little. The present polydisperse modelling approach describes this behaviour at least qualitatively correct.

Comparing the radial gas volume fraction profiles with decreasing subcooling, a broadening of the wall peaking profile can be observed for both test series. This effect is due to a lower condensation rate in the bulk liquid as the subcooling decreases. Again this behaviour is described qualitatively correct by the present modeling approach where bubbles of all sizes move with the same velocity. A change from wall to core peaking profiles as for the test series considered by Krepper et al. [11] is not observed here. This matches with the explanation that such a transition is related to the sign change in the lift force as discussed in Section 3.4.2. For the presently investigated tests, the bubble size remains below this value while for the cases of Krepper et al. [11] it became larger for the lower values of subcooling.

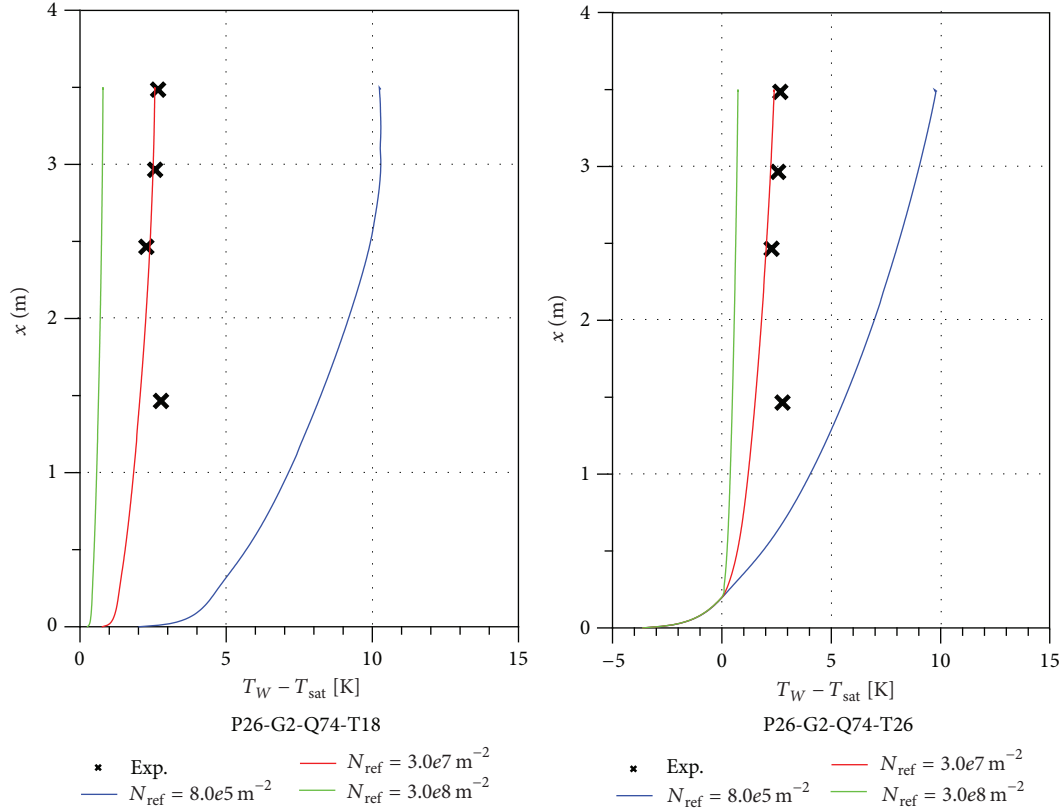


FIGURE 4: Wall superheat depending on the reference nucleation site density N_{ref} .

7. Summary and Conclusions

Boiling at a heated wall has been simulated by an Euler/Euler description of two-phase flow combined with a heat flux partitioning model describing the microscopic phenomena at the wall by empirical correlations adapted to experimental data. Such an approach was previously used and adjusted to boiling experiments with water at a pressure of several MPa. We here have investigated the applicability and necessary readjustments for similar tests using R12 at the DEBORa facility. At the same time, the bubble size distribution in the bulk was described by a population balance approach by coupling the wall boiling model with the MUSIG model.

A critical review of the detailed correlations used in previous work shows that some of the parameters used in these correlations have to be carefully recalibrated for the present applications. The DEBORa tests provide a large body of information that can be used to this end. Quantities with a strong influence on the amount of produced steam are the bubble size at detachment and the nucleation site density. The former can be taken straight forwardly from the measurements. On the latter, unfortunately no direct information is available; however, by matching the temperature of the heated wall, this gap can be closed. Previous work [10] has shown that the recalibration results in different values for different pressure levels. The present results suggest that for the bubble detachment size, a different calibration is needed for different flow rates but not for different heat fluxes while

for the nucleation site density, the same calibration can be used independently of either liquid subcooling, flow rate, and heat flux.

The measured gas bubble size profiles show an increase of the bubble size with increased distance from the heated wall. A monodispersed treatment is not able to capture this phenomenon, but including polydispersity by means of a MUSIG approach and suitable models especially for bubble coalescence this phenomenon can be described. In contrast to a previously investigated series of test cases [11], as the subcooling is decreased only a broadening of the wall peaking gas volume fraction profile occurs, but no transition to a core peaking profile is observed. Again this phenomenon could not be captured by a model with a monodisperse bubble size but can be described using a homogeneous MUSIG approach since the bubbles remain small enough so the sign change in the lift force does not occur.

A complete polydispersed description requires that processes of coalescence/breakup and condensation/evaporation must be modeled explicitly. For the latter, a suitable model is readily obtained from first principles with the aid of a heat transfer correlation like that of Ranz and Marshall [46]. Unfortunately the former are the more important processes, and for these the situation is much less clear. In the present work, the commonly applied models for bubble coalescence according to Prince and Blanch [44] and for bubble breakup according to Luo and Svendsen [43] were used as a first step. To reach a fair agreement with the measurements,

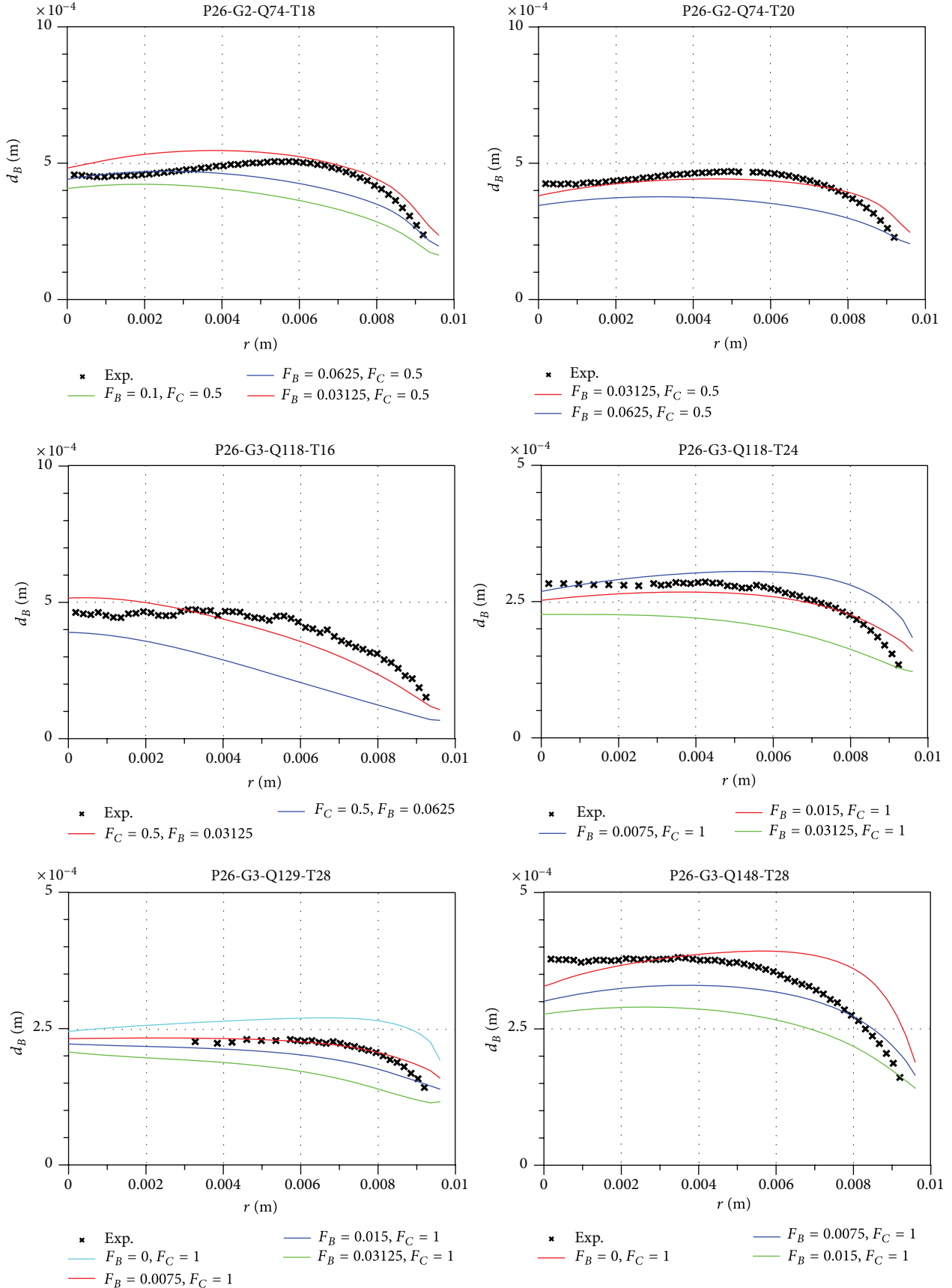
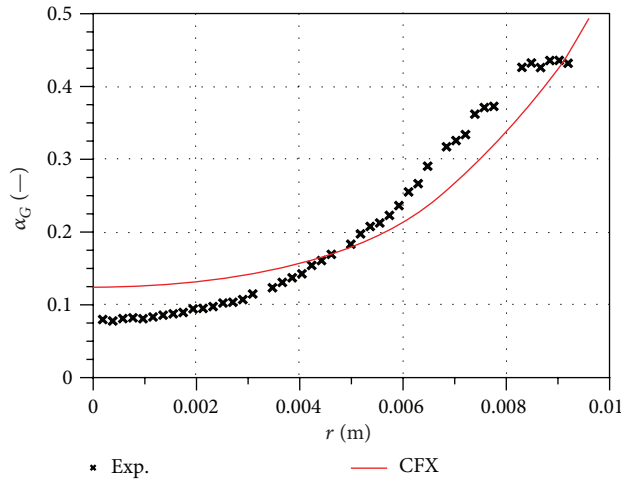
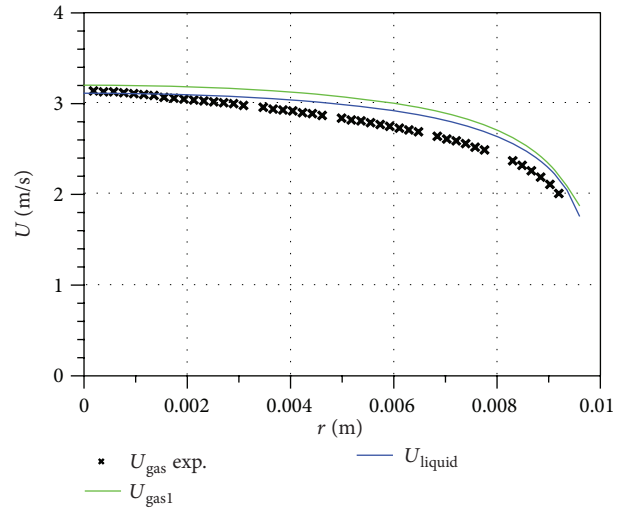


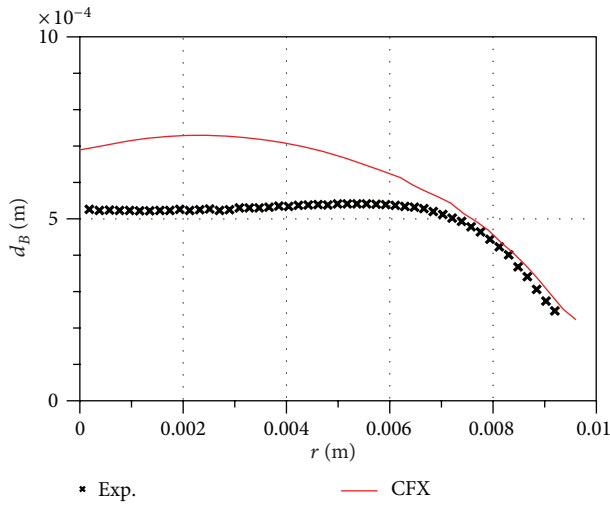
FIGURE 5: Radial profiles of bubble size for different coefficients F_B and F_C .



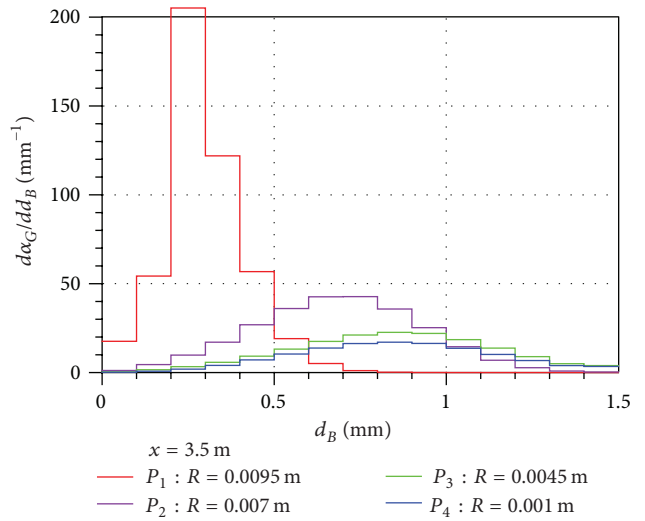
(a) Gas volume fraction



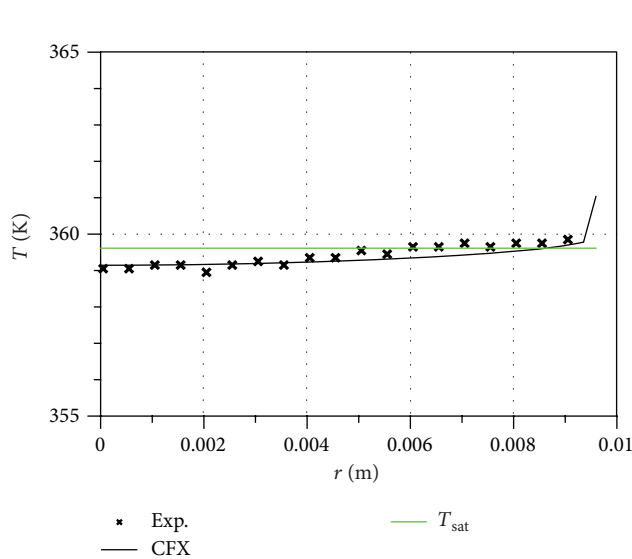
(b) Gas and liquid velocities



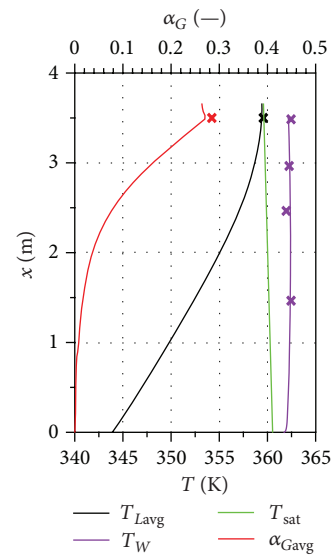
(c) Radial bubble size profile



(d) Bubble size distribution at four points



(e) Temperature



(f) Cross-sectionally averaged values

FIGURE 6: Comparison of measured and calculated values for P26-G2-Q74-T16: $P = 2.62 \text{ MPa}$, $G = 2 \cdot 10^3 \text{ kg m}^{-2} \text{ s}^{-1}$, $T_{in} = 70.7^\circ \text{C}$.

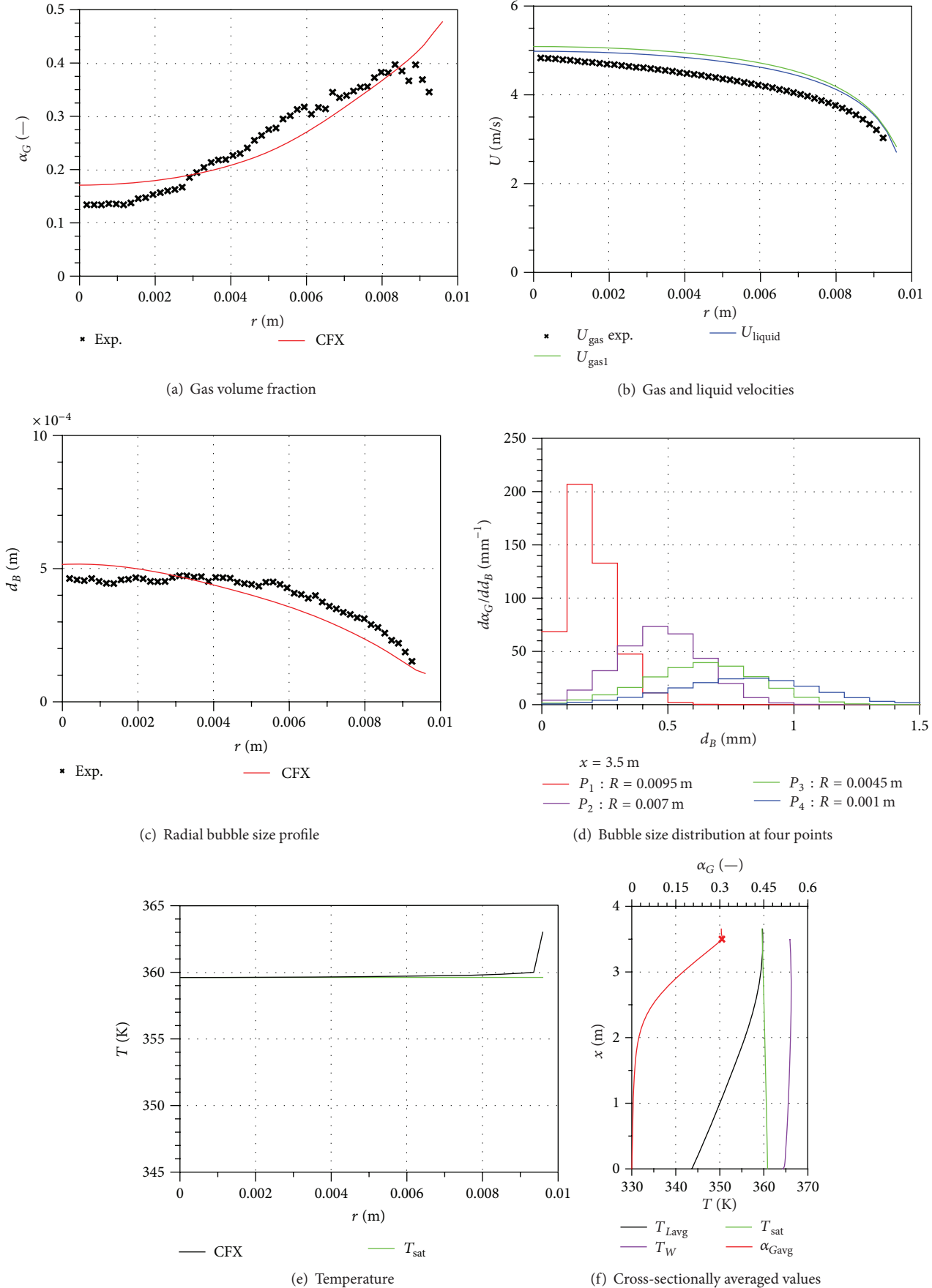
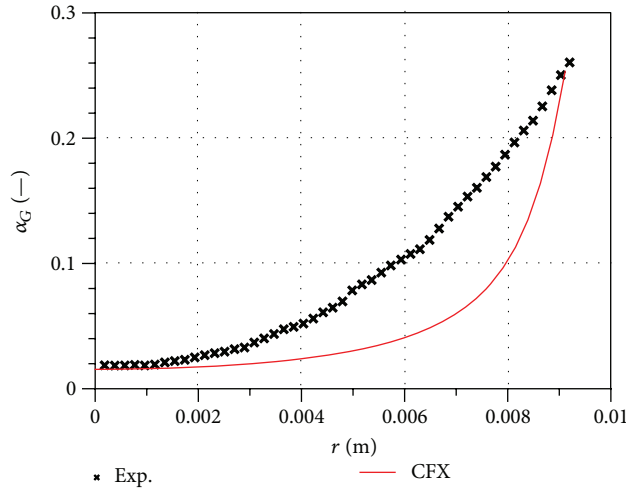
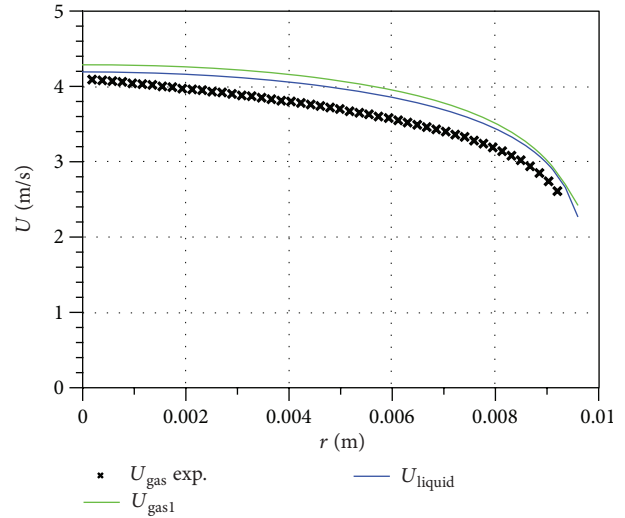


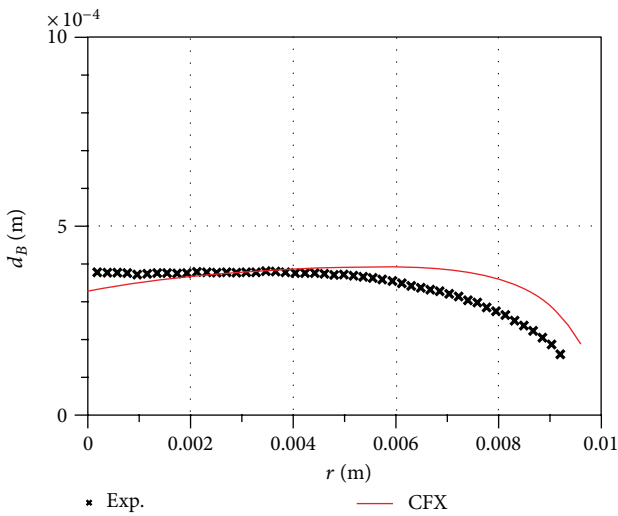
FIGURE 7: Comparison of measured and calculated values for P26-G3-Q118-T16: $P = 2.62$ MPa, $G = 3 \cdot 10^3$ kg m⁻² s⁻¹, $T_{in} = 70.73^\circ$ C.



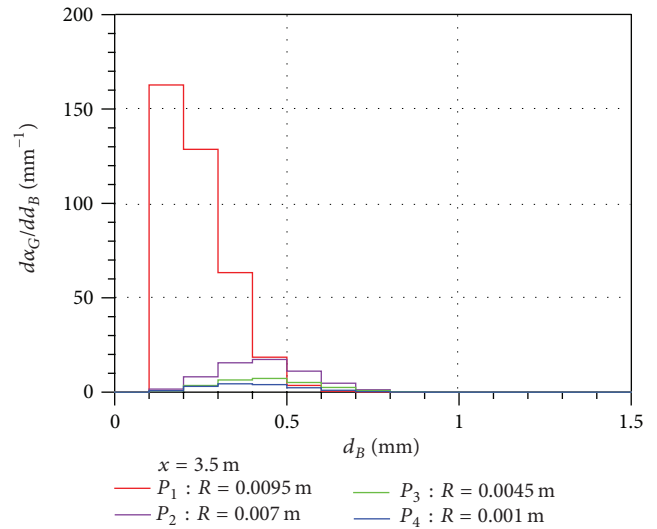
(a) Gas volume fraction



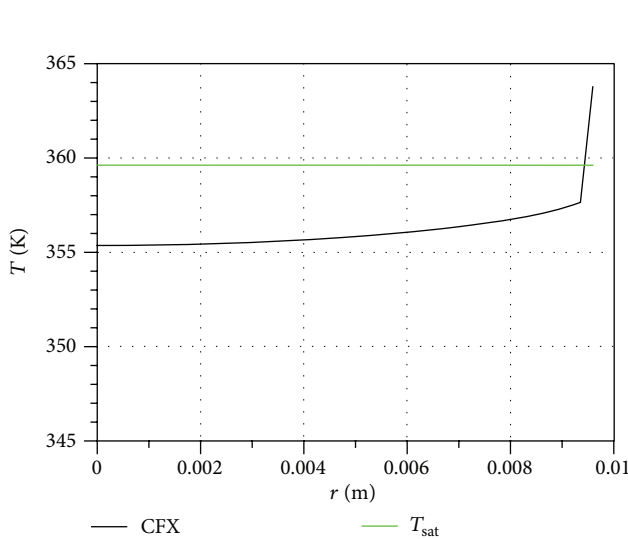
(b) Gas and liquid velocities



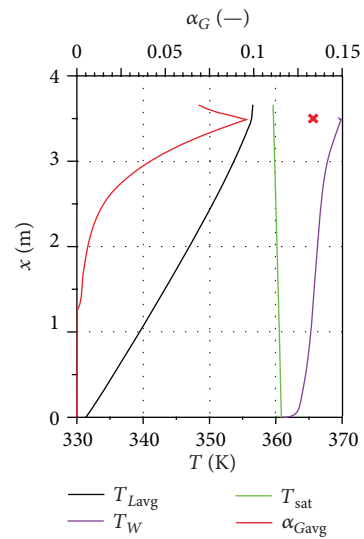
(c) Radial bubble size profile



(d) Bubble size distribution at four points



(e) Temperature



(f) Cross-sectionally averaged values

FIGURE 8: Comparison of measured and calculated values for P26-G3-Q148-T28: $P = 2.62 \text{ MPa}$, $G = 3 \cdot 10^3 \text{ kg m}^{-2} \text{ s}^{-1}$, $T_{in} = 58.2^\circ\text{C}$.

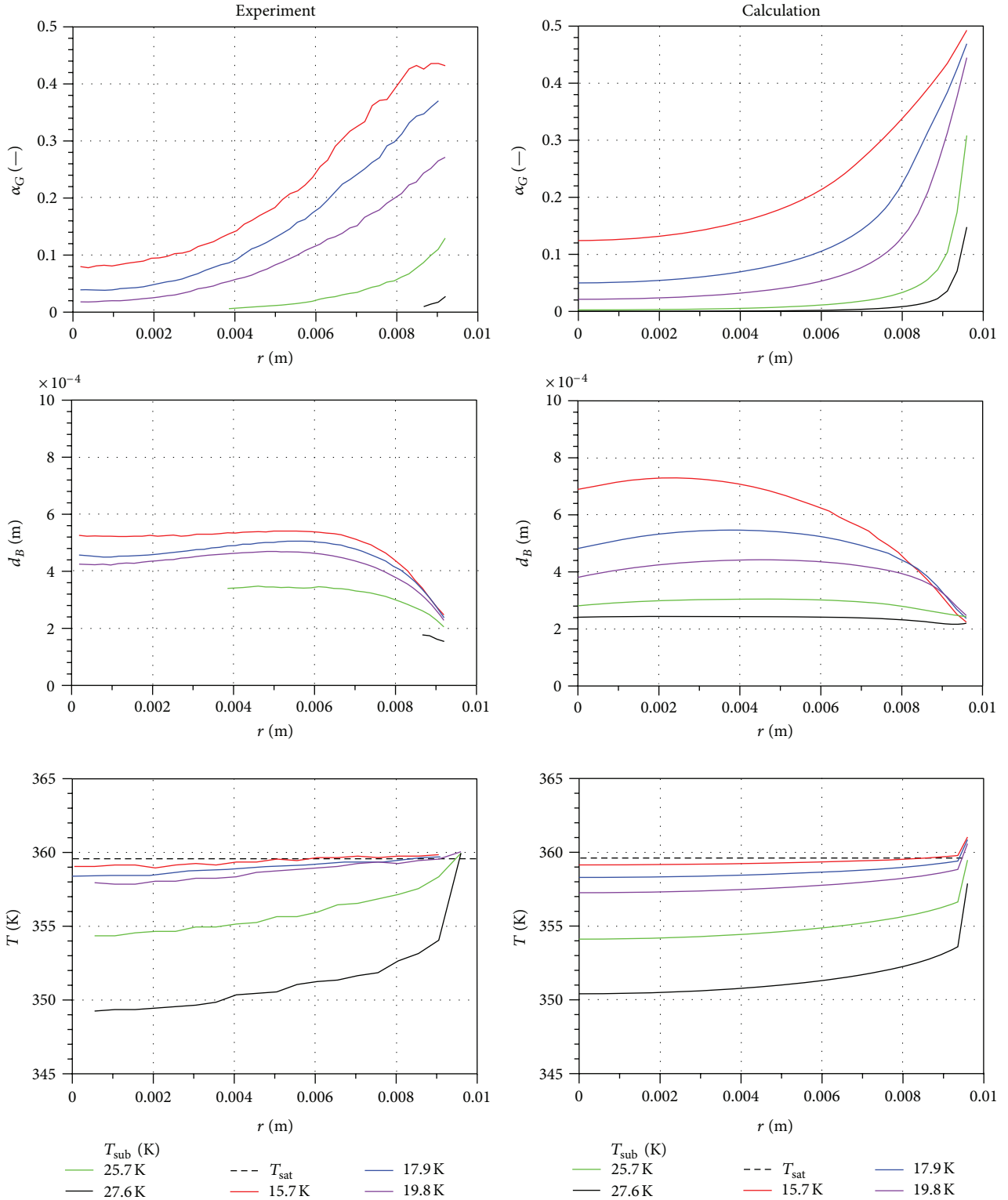


FIGURE 9: Gas volume fraction, bubble size, and liquid temperature profiles for test series P26-G2-Q74-Txx.

calibration factors had to be introduced, which need to be adjusted according to the experimental condition. In this way the suitability of the general model framework could be demonstrated in principle. For a trusted prediction, further

development of the coalescence and break-up models is necessary.

Bubble coalescence and breakup are heavily influenced by two-phase flow turbulence. Unfortunately in the literature,

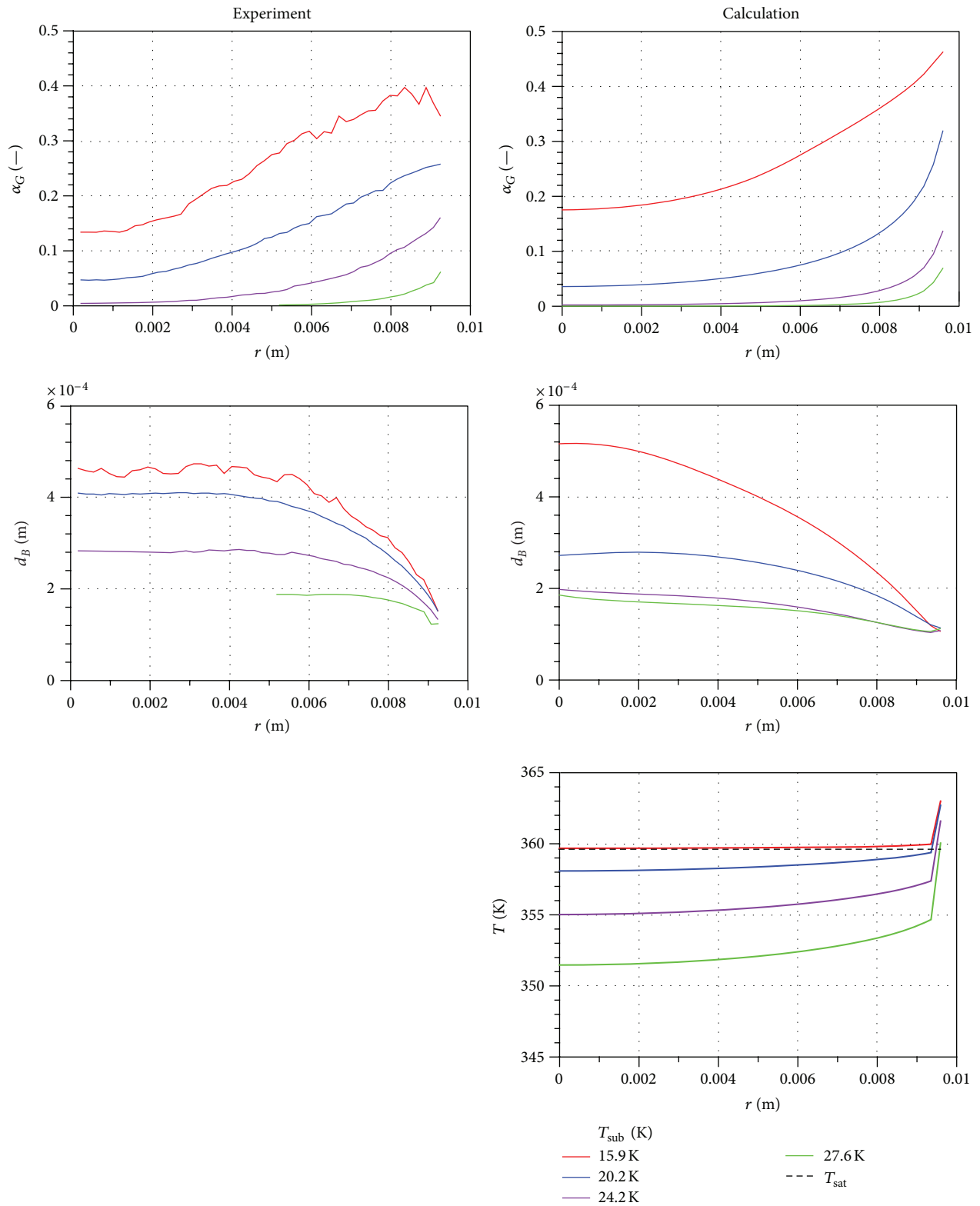


FIGURE 10: Gas volume fraction, bubble size, and liquid temperature profiles for test series P26-G3-Q118-Txx.

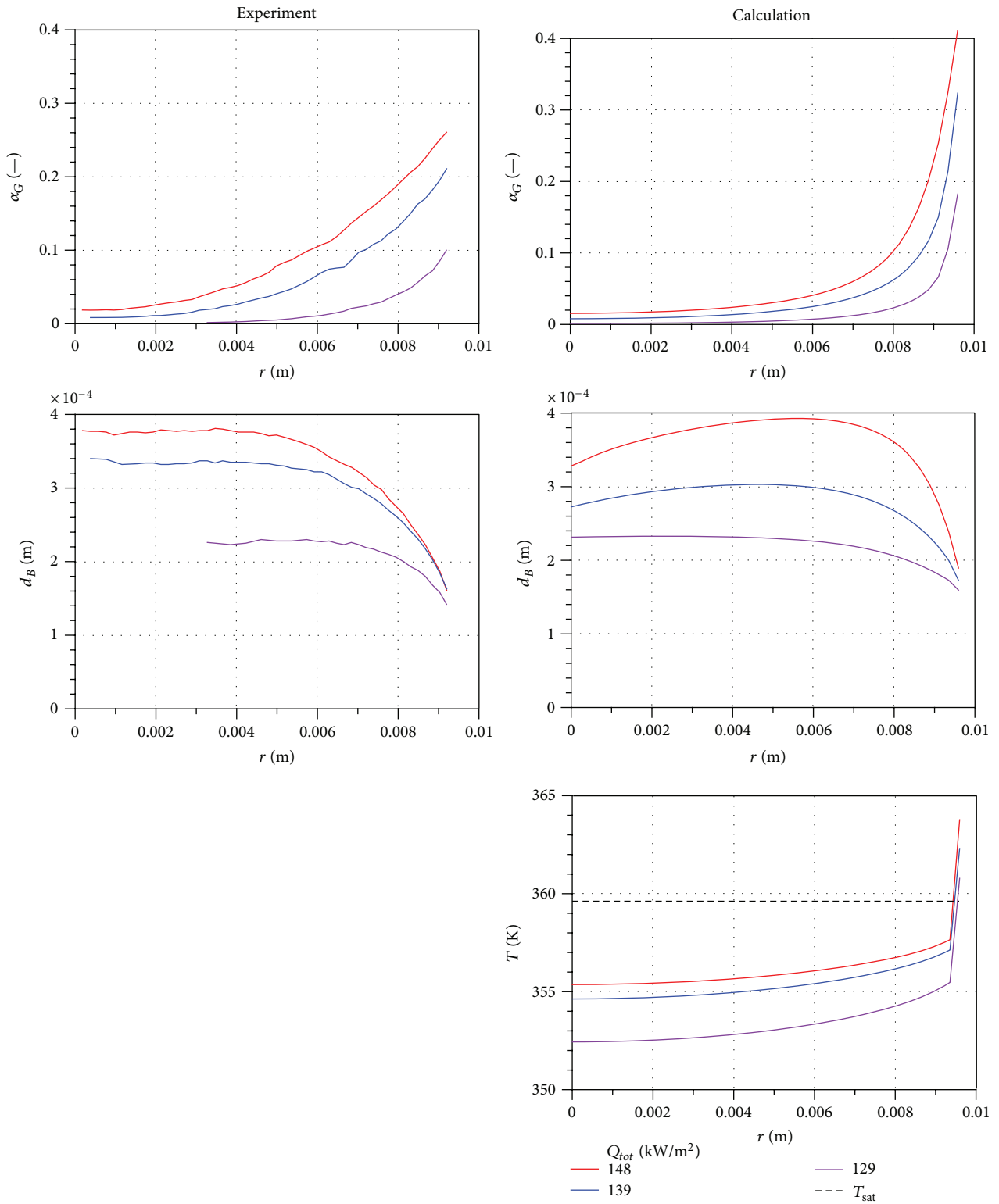


FIGURE 11: Gas volume fraction, bubble size, and liquid temperature profiles for test series P26-G3-Qxx-T28.

only few measurements of turbulent characteristics of two phase flow can be found and even less when boiling occurs. Furthermore, models of bubble-induced turbulence working well for air/water flow may fail for steam/water flow at higher pressure or for refrigerants. In the present work, the selection of a specific model for bubble effects on the turbulence is confirmed mainly by plausibility of the final results. Hence, a more systematic investigation of approaches to modeling bubbly turbulence would be desirable.

Finally, looking carefully at the figures showing the gas volume fraction profiles in the near wall region, the calculated gas volume fraction is systematically too large. Reasons could be a missing force pushing the bubbles away from the wall or the neglect of swarm effects in the models of drag and lift forces even at gas volume fractions around 50%. Furthermore, the application of the simple heat transfer correlation of Ranz and Marshall [46] might be questionable. In transferring models used successfully for adiabatic air/water flows to the DEBORA tests, it should be noted that bubbles are much smaller here which may require changes beyond simple recalibration of parameters.

Overall, our results confirm the great potential of the Euler/Euler two-phase flow and heat flux partitioning models for the simulation of subcooled flow boiling in industrial applications while at the same time highlighting the need for specific model improvements in order to achieve highly accurate quantitative predictions.

Nomenclature

Notation

A_I :	Interfacial area density
C_B :	Bubble-induced turbulence coefficient [17] model
C_D :	Drag coefficient
C_L :	Lift coefficient
C_p :	Specific heat capacity at constant pressure ($\text{J K}^{-1} \text{kg}^{-3}$)
C_{TD} :	Turbulent dispersion coefficient
C_{VM} :	Virtual mass force coefficient
C_W :	Wall force coefficient
C_{μ} :	Shear-induced turbulence coefficient (k - ε model)
d_B :	Bulk bubble diameter (m)
d_{\perp} :	Bubble diameter perpendicular to main motion (m)
d_W :	Bubble detachment diameter (m)
D :	Pipe diameter (m)
Eo :	Eötvös' number
f :	Bubble detachment frequency (Hz)
F_D :	Drag force (N m^{-3})
F_L :	Lift force (N m^{-3})
F_{TD} :	Turbulent dispersion force (N m^{-3})
F_{VM} :	Virtual mass force (N m^{-3})
F_W :	Wall force (N m^{-3})
g :	Acceleration of gravity (m s^{-2})

h_C :	Heat transfer coefficient for single-phase convection ($\text{W m}^{-2} \text{K}^{-1}$)
h_{LG} :	Heat transfer coefficient for bulk evaporation/condensation ($\text{W m}^{-2} \text{K}^{-1}$)
h_Q :	Heat transfer coefficient for quenching ($\text{W m}^{-2} \text{K}^{-1}$)
H :	Specific enthalpy (J kg^{-3})
Ja :	Jakob's number
k :	Thermal conductivity ($\text{W m}^{-1} \text{K}^{-1}$)
k :	Turbulent kinetic energy ($\text{m}^2 \text{s}^{-2}$)
L :	Length scale (m)
\dot{m} :	Massflux
Mo :	Morton's number
N :	Nucleation site density (m^{-3})
p :	Pressure (Pa)
Pr :	Prandtl number
Q_{tot} :	Wall heat flux (W m^{-2})
Q_C :	Heat flux due to single-phase convection (W m^{-2})
Q_Q :	Heat flux due to quenching (W m^{-2})
Q_E :	Heat flux due to evaporation (W m^{-2})
r :	Radial coordinate (m)
Re :	Reynolds' number
s :	Hydrodynamic wall roughness (m)
t :	Time (s)
t_{wait} :	Waiting time (s)
T :	Temperature (K)
T_{sat} :	Saturation temperature (K)
T_{sub} :	Liquid subcooling (K)
T_{sup} :	Wall superheat (K)
T_W :	Wall temperature (K)
\mathbf{u} :	Velocity (m s^{-1})
u_{τ} :	Friction velocity (m s^{-1})
U :	Velocity scale (m s^{-1})
V :	Volume (m^3)
x :	Axial coordinate (m)
y :	Distance to the wall (m)
α :	Volume fraction
δ :	Viscous length scale (m)
ε :	Turbulent dissipation rate ($\text{m}^2 \text{s}^{-3}$)
ΔT :	Temperature scale (K)
μ :	Dynamic viscosity ($\text{kg m}^{-1} \text{s}^{-1}$)
ν :	Kinematic viscosity ($\text{m}^2 \text{s}^{-1}$)
ρ :	Density (kg m^{-3})
σ :	Surface tension (N m^{-1})
τ_w :	Wall shear stress (N m^{-2}).

Index

B :	Bulk
C :	Due to single-phase convection
E :	Due to evaporation
G :	Gas
I :	Interface
L :	Liquid
Q :	Due to quenching
sat:	Saturation

tot: Total
 W: Wall
 +: Nondimensional.

Acknowledgment

This work is funded by the Federal Ministry of Education and Research (Contract no. 02NUK010A).

References

- [1] D. A. Drew and S. L. Passman, *Theory of Multicomponent Fluids*, Springer, 1998.
- [2] G. H. Yeoh and J. Y. Tu, *Computational Techniques for Multiphase Flows—Basics and Applications*, Elsevier Science and Technology, 2010.
- [3] M. Ishii and T. Hibiki, *Thermo-Fluid Dynamics of Two-Phase Flow*, Springer, 2nd edition, 2011.
- [4] N. Kurul and M. Z. Podowski, “Multidimensional effects in forced convection subcooled boiling,” in *Proceedings of the 9th International Heat Transfer Conference*, Jerusalem, Israel, 1990.
- [5] N. Kurul and M. Podowski, “On the modeling of multidimensional effects in boiling channels ANS,” in *Proceedings of the 27th National Heat Transfer Conference*, Minneapolis, Minn, USA, 1991.
- [6] E. Krepper, B. Končar, and Y. Egorov, “CFD modelling of subcooled boiling-concept, validation and application to fuel assembly design,” *Nuclear Engineering and Design*, vol. 237, no. 7, pp. 716–731, 2007.
- [7] G. G. Bartolomej and V. M. Chanturiya, “Experimental study of true void fraction when boiling subcooled water in vertical tubes,” *Thermal Engineering*, vol. 14, pp. 123–128, 1967.
- [8] E. Manon, *Contribution à l'analyse et à la modélisation locale des écoulements bouillants sous-saturés dans les conditions des Réacteurs à Eau sous Pression [Ph.D. thesis]*, Ecole Centrale Paris, 2000.
- [9] J. Garnier, E. Manon, and G. Cubizolles, “Local measurements on flow boiling of refrigerant 12 in a vertical tube,” *Multiphase Science and Technology*, vol. 13, no. 1-2, pp. 1–111, 2001.
- [10] E. Krepper and R. Rzehak, “CFD for subcooled flow boiling: simulation of DEBORA experiments,” *Nuclear Engineering and Design*, vol. 241, pp. 3851–3866, 2011.
- [11] E. Krepper, R. Rzehak, C. Lifante, and T. Frank, “CFD for subcooled flow boiling: coupling wall boiling and population balance models,” *Nuclear Engineering and Design*, vol. 255, pp. 330–346, 2013.
- [12] W. Yao and C. Morel, “Prediction of parameters distribution of upward boiling two-phase flow with two-fluid models,” in *proceedings of the 10th International Conference on Nuclear Engineering (ICONE '10)*, pp. 801–808, Arlington, Va, USA, April 2002.
- [13] W. Yao and C. Morel, “Volumetric interfacial area prediction in upward bubbly two-phase flow,” *International Journal of Heat and Mass Transfer*, vol. 47, no. 2, pp. 307–328, 2004.
- [14] M. Bucker, A. Guelfi, S. Mimouni, P. Péturaud, D. Bestion, and E. Hervieu, “Towards the prediction of local thermal-hydraulics in real PWR core conditions using neptune_CFD software,” in *Proceedings of the Workshop on Modeling and Measurements of Two-Phase Flows and Heat Transfer in Nuclear Fuel Assemblies*, pp. 1784–1793, Stockholm, Sweden, October 2006.
- [15] F. R. Menter, “Two-equation eddy-viscosity turbulence models for engineering applications,” *AIAA journal*, vol. 32, no. 8, pp. 1598–1605, 1994.
- [16] F. R. Menter, “Review of the shear-stress transport turbulence model experience from an industrial perspective,” *International Journal of Computational Fluid Dynamics*, vol. 23, no. 4, pp. 305–316, 2009.
- [17] Y. Sato, M. Sadatomi, and K. Sekoguchi, “Momentum and heat transfer in two-phase bubble flow-I. Theory,” *International Journal of Multiphase Flow*, vol. 7, no. 2, pp. 167–177, 1981.
- [18] M. S. Politano, P. M. Carrica, and J. Converti, “A model for turbulent polydisperse two-phase flow in vertical channels,” *International Journal of Multiphase Flow*, vol. 29, no. 7, pp. 1153–1182, 2003.
- [19] T. Wintterle, *Development of a numerical boundary condition for the simulation of nucleate boiling at heated walls [Diploma thesis]*, University Stuttgart, 2004, IKE-8-D-014.
- [20] B. A. Kader, “Temperature and concentration profiles in fully turbulent boundary layers,” *International Journal of Heat and Mass Transfer*, vol. 24, no. 9, pp. 1541–1544, 1981.
- [21] H. C. Ünal, “Maximum bubble diameter, maximum bubble-growth time and bubble-growth rate during the subcooled nucleate flow boiling of water up to 17.7 MN/m²,” *International Journal of Heat and Mass Transfer*, vol. 19, no. 6, pp. 643–649, 1976.
- [22] R. H. S. Winterton, “Flow boiling: prediction of bubble departure,” *International Journal of Heat and Mass Transfer*, vol. 27, no. 8, pp. 1422–1424, 1984.
- [23] L. Z. Zeng, J. F. Klausner, D. M. Bernhard, and R. Mei, “A unified model for the prediction of bubble detachment diameters in boiling systems-II. Flow boiling,” *International Journal of Heat and Mass Transfer*, vol. 36, no. 9, pp. 2271–2279, 1993.
- [24] S. Kandlikar, V. Mizo, and M. Cartwright, “Investigation of bubble departure mechanism in subcooled flow boiling of water using high-speed photography,” in *Proceedings of the Convective Flow Boiling International Conference*, April 1995.
- [25] J. F. Klausner, R. Mei, and L. Z. Zeng, “Predicting stochastic features of vapor bubble detachment in flow boiling,” *International Journal of Heat and Mass Transfer*, vol. 40, no. 15, pp. 3547–3552, 1997.
- [26] R. Situ, T. Hibiki, M. Ishii, and M. Mori, “Bubble lift-off size in forced convective subcooled boiling flow,” *International Journal of Heat and Mass Transfer*, vol. 48, no. 25-26, pp. 5536–5548, 2005.
- [27] N. Basu, G. R. Warrier, and V. K. Dhir, “Wall heat flux partitioning during subcooled flow boiling: part 1—model development,” *Journal of Heat Transfer*, vol. 127, no. 2, pp. 131–140, 2005.
- [28] P. Griffith and J. Wallis, “The role of surface conditions in nucleate boiling,” *Chemical Engineering Progress Symposium Series*, 1960.
- [29] K. T. Hong, H. Imadojemu, and R. L. Webb, “Effects of oxidation and surface roughness on contact angle,” *Experimental Thermal and Fluid Science*, vol. 8, no. 4, pp. 279–285, 1994.
- [30] V. I. Tolubinsky and D. M. Kostanchuk, “Vapour bubbles growth rate and heat transfer intensity at subcooled water boiling, Heat Transfer 1970,” in *Proceedings of the 4th International Heat Transfer Conference*, vol. 5, no. B-2. 8, 1970.
- [31] N. I. Kolev, “Uniqueness of the elementary physics driving heterogeneous nucleate boiling and flashing,” *Nuclear Engineering and Technology*, vol. 38, p. 175, 2006.

- [32] S. F. Jones, G. M. Evans, and K. P. Galvin, "Bubble nucleation from gas cavities—a review," *Advances in Colloid and Interface Science*, vol. 80, no. 1, pp. 27–50, 1999.
- [33] G. Mitrovic and K. Stephan, "Gleichgewichtsradien von Dampfblasen und Flüssigkeitstropfen," *Wärme-Und Stoffübertragung*, vol. 13, p. 171, 1980.
- [34] C. Y. Han and P. Griffith, "The mechanism of heat transfer in nucleate pool boiling—Part I. Bubble initiation, growth and departure," *International Journal of Heat and Mass Transfer*, vol. 8, no. 6, pp. 887–904, 1965.
- [35] J. T. Cieslinski, J. Polewski, and J. A. Szymczyk, "Flow field around growing and rising vapour bubble by piv measurement," *Journal of Visualization*, vol. 8, no. 3, pp. 209–216, 2005.
- [36] R. Cole, "A photographic study of pool boiling in the region of the critical heat flux," in *AICHE Journal*, vol. 6, pp. 533–542, 1960.
- [37] H. J. Ivey, "Relationships between bubble frequency, departure diameter and rise velocity in nucleate boiling," *International Journal of Heat and Mass Transfer*, vol. 10, no. 8, pp. 1023–1040, 1967.
- [38] W. C. B. V. Ceumern-Lindenstjerna, "Bubble departure diameter and release frequencies during nucleate pool boiling of water and aqueous NaCl solutions," in *Heat Transfer in Boiling*, E. Hahne and U. Grigull, Eds., Academic Press and Hemisphere, 1977.
- [39] B. B. Mikic and W. M. Rohsenow, "A new correlation of pool-boiling data including the fact of heating surface characteristics," *ASME Journal of Heat Transfer*, vol. 91, pp. 245–250, 1969.
- [40] V. H. Del Valle and D. B. R. Kenning, "Subcooled flow boiling at high heat flux," *International Journal of Heat and Mass Transfer*, vol. 28, no. 10, pp. 1907–1920, 1985.
- [41] T. Frank, P. J. Zwart, E. Krepper, H. M. Prasser, and D. Lucas, "Validation of CFD models for mono- and polydisperse air-water two-phase flows in pipes," *Nuclear Engineering and Design*, vol. 238, no. 3, pp. 647–659, 2008.
- [42] E. Krepper, D. Lucas, T. Frank, H. M. Prasser, and P. J. Zwart, "The inhomogeneous MUSIG model for the simulation of polydispersed flows," *Nuclear Engineering and Design*, vol. 238, no. 7, pp. 1690–1702, 2008.
- [43] H. Luo and H. F. Svendsen, "Theoretical model for drop and bubble breakup in turbulent dispersions," *AICHE Journal*, vol. 42, no. 5, pp. 1225–1233, 1996.
- [44] M. J. Prince and H. W. Blanch, "Bubble coalescence and breakup in air-sparged bubble columns," *AICHE Journal*, vol. 36, no. 10, pp. 1485–1499, 1990.
- [45] D. Lucas, T. Frank, C. Lifante, P. Zwart, and A. Burns, "Extension of the inhomogeneous MUSIG model for bubble condensation," *Nuclear Engineering and Design*, vol. 241, pp. 4359–4367, 2011.
- [46] W. E. Ranz and W. R. Marshall, "Evaporation from drops," *Chemical Engineering Progress*, vol. 48, no. 3, pp. 141–146, 1952.
- [47] E. Krepper, M. Beyer, D. Lucas, and M. Schmidtke, "A population balance approach considering heat and mass transfer—Experiments and CFD simulations," *Nuclear Engineering and Design*, vol. 241, no. 8, pp. 2889–2897, 2011.
- [48] C. Lifante, F. Reiterer, Th. Frank, and A. Burns, "Coupling of wall boiling with discrete population balance model," in *Proceedings of the 14th International Topical Meeting on Nuclear Reactor Thermalhydraulics (NURETH '14)*, pp. 25–30, Toronto, Canada, September 2011.
- [49] A. A. Troshko and Y. A. Hassan, "A two-equation turbulence model of turbulent bubbly flows," *International Journal of Multiphase Flow*, vol. 27, no. 11, pp. 1965–2000, 2001.
- [50] S. Lee, R. Lahey Jr., and O. Jones, "The prediction of two-phase flow turbulence and phase distribution using a k-e model," *Japanese Journal of Multiphase Flow*, vol. 3, p. 335, 1989.
- [51] D. Pflieger and S. Becker, "Modelling and simulation of the dynamic flow behaviour in a bubble column," *Chemical Engineering Science*, vol. 56, no. 4, pp. 1737–1747, 2001.
- [52] F. Ramstorfer, B. Breitschädel, H. Steiner, and G. Brenn, "Modelling of the near-wall liquid velocity field in subcooled boiling flow," in *Proceedings of the ASME Summer Heat Transfer Conference (HT '05)*, pp. 323–332, San Francisco, Calif, USA, July 2005.
- [53] B. Končar and M. Borut, "Wall function approach for boiling two-phase flows," *Nuclear Engineering and Design*, vol. 240, no. 11, pp. 3910–3918, 2010.
- [54] F. M. White, *Viscous Fluid Flow*, McGraw-Hill, 1991.
- [55] S. B. Pope, *Turbulent Flow*, 2000.
- [56] M. Ishii and N. Zuber, "Drag coefficient and relative velocity in bubbly, droplet or particulate flows," *AICHE Journal*, vol. 25, no. 5, pp. 843–855, 1979.
- [57] A. Tomiyama, H. Tamai, I. Zun, and S. Hosokawa, "Transverse migration of single bubbles in simple shear flows," *Chemical Engineering Science*, vol. 57, no. 11, pp. 1849–1858, 2002.
- [58] A. D. Burns, T. Frank, I. Hamill, and J. M. Shi, "The Favre averaged drag model for turbulence dispersion in Eulerian multi-phase flows," in *Proceedings of the 5th International Conference on Multiphase Flow (ICMF '04)*, Yokohama, Japan, 2004.
- [59] I. Zun, "The transverse migration of bubbles influenced by walls in vertical bubbly flow," *International Journal of Multiphase Flow*, vol. 6, no. 6, pp. 583–588, 1980.
- [60] M. Schmidtke, *Investigation of the dynamics of fluid particles using the Volume of Fluid Method [Ph.D. thesis]*, University Paderborn, 2008.
- [61] R. M. Wellek, A. K. Agrawal, and A. H. P. Skelland, "Shapes of liquid drops moving in liquid media," *AICHE Journal*, vol. 12, pp. 854–860, 1966.
- [62] D. Lucas, E. Krepper, and H. M. Prasser, "Use of models for lift, wall and turbulent dispersion forces acting on bubbles for polydisperse flows," *Chemical Engineering Science*, vol. 62, no. 15, pp. 4146–4157, 2007.
- [63] D. Lucas and E. Krepper, "CFD models for polydispersed bubbly flows," 2007, Forschungszentrum Dresden, FZD-486.
- [64] ANSYS, *ANSYS CFX-Solver Theory Guide*, Release 13 ANSYS, 2010.

Research Article

Bubble Departure Diameter Prediction Uncertainty

Marko Matkovič and Boštjan Končar

Jozef Stefan Institute, Jamova 39, 1000 Ljubljana, Slovenia

Correspondence should be addressed to Marko Matkovič, marko.matkovic@ijs.si

Received 25 May 2012; Accepted 11 December 2012

Academic Editor: Dominique Bestion

Copyright © 2012 M. Matkovič and B. Končar. This is an open access article distributed under the Creative Commons Attribution License, which permits unrestricted use, distribution, and reproduction in any medium, provided the original work is properly cited.

This paper presents quality assessment of a mechanistic modelling for bubble departure diameter prediction during pool boiling condition. In contrast to flow boiling process only buoyancy force with opposing surface tension force was considered as the responsible mechanisms for bubble departure. Indeed, inertia from the fluid flow around the bubble and the growth force, which describes momentum change due to the evaporation at the bubble base and condensation at the top of the bubble, were all neglected. Besides, shear lift force and quasi-steady drag force as the dominant inertia driven forces were also neglected in the assessment. Rather than trying to model bubble dynamics as precise as possible by properly addressing all the relevant mechanisms available, the work focuses on prediction accuracy of such approach. It has been shown that inlet boundary conditions with realistic experimental accuracy may lead to a significant uncertainty in the prediction of bubble departure diameter, which is intrinsically connected to the uncertainty of most heat partitioning and CHF models.

1. Introduction

Boiling process is so widely met in everyday life that one often forgets to deal with one of the most complex phenomena in energy and process engineering. Precise and accurate prediction of boiling heat transfer is crucial both in terms of rational use of energy as well as from the standpoint of safe operation of such systems. With reference to the nuclear engineering applications an accurate prediction of the governing mechanisms would have significantly decreased exergy losses during flow boiling heat transfer. A reliable prediction of the critical heat flux on the other hand could have not only increased the nominal power of the steam generators at PWR but it would have improved safety issues in those systems as well. Regarding boiling a significant amount of research activity has been carried out for the past 60 years mainly with the purpose of quantitative evaluation of the mechanisms involved. Many researchers studied heat transfer mechanisms at subcooled flow conditions and proposed the modelling approach that considers the flow boiling heat transfer as a superposition of the liquid-phase convective heat transfer and the evaporation heat transfer mechanisms [1, 2]. Wall heat flux during the subcooled

flow nucleate boiling was thus partitioned for different heat transfer mechanisms of the boiling process. In this context, part of the heat flux, which is responsible for evaporation, was studied profoundly through active nucleation sites and their surface density, and the frequency of bubble formation and their diameter at departure. There are quite some models available in the open literature for bubble growth and its diameter prediction at departure. Bubble departure diameter prediction, which was published by Fritz [3] for instance, takes into account a balance between buoyancy force and surface tension force only. One of the first models to determine maximum bubble volume is often inconsistent with experimental measurements particularly at high values of reduced pressures. Consequential development of new models often led to different or even conflicting influential parameters. Cole and Rohsenow [4] proposed correlation for calculation of bubble departure diameter at low pressure for boiling water and other liquids by introduction of the two distinct leading constants. They also introduced the bubble size dependence on the modified Jacob number. In search for efficient model for bubble departure diameter prediction Tolubinski and Kostanchuk [5] studied different surfaces and wall temperature overheating. While Kocamustafaogullari

[6] tried to include various reduced pressures in his studies Gorenflo et al. [7] focused on high specific heat flow rates at elevated saturation pressure. They highlighted the significance of thermal diffusivity and Jacob number, but ignored the impact of the density ratio of competing phases. Despite extensive efforts by researchers to date rather modest progress has been achieved in identifying and predicting the growth mechanisms and dynamics of bubbles. The main reason for the lack of new knowledge is limited understanding of the temperature and velocity fields in the boiling boundary layer influenced by the bubble dynamics. There the parameters are evolving rapidly in time and space, which made these measurements inaccessible until recent time. Besides, wetting angle and the mutual interaction between the bubbles are also deficiently studied. On one hand there are new experimental techniques available for heat transfer and fluid flow measurements within wall boundary layer [8] while on the other hand new approaches based on direct numerical simulations seem to become more and more important for better understanding of the two-phase flow and heat transfer mechanisms [9].

Aim of the present inquiry is the qualitative evaluation of the bubble departure diameter modelling. To start with, prediction uncertainty of bubble departure and bubble growth diameters during pool boiling test conditions has been analysed. Buoyancy with opposing surface tension force is here assumed to be the responsible mechanisms for bubble departure even though shear lift force and quasi-steady drag force are believed the influential inertia driven forces as well. They act together with the buoyancy force against the surface tension force that is the only mechanism responsible for keeping the bubbles attached on the wall. In fact, bubble diameter tends to favour buoyancy force versus surface tension force. The bigger is the density ratio and the bigger is the gravity acceleration at reference surface tension, the smaller is the required bubble diameter at departure. However, the dominant inertia driven forces (shear lift force and quasi-steady drag force), as well as the growth force or so-called unsteady drag force, which describes momentum change due to evaporation at the bubble base and condensation at the top of the bubble, were all neglected in the assessment. At this point, rather than including all driving mechanisms for bubble modelling, the work focuses on the prediction accuracy of bubble departure diameter during the pool boiling phenomenon. Therefore, uncertainty analyses of bubble growth and bubble departure diameter modelling have been carried out.

2. Modelling Background

One of the key parameters for characterizing the flow boiling phenomenon is usually addressed to the diameter to which a bubble grows before departure. On this subject, a large number of correlations and mechanistic approaches have been proposed in the literature. Almost eight decades ago Fritz [3] calculated the maximum volume for vapour bubbles by compensating the buoyancy force that acts to lift the bubbles away from the heating surface with the surface

tension force, which holds the bubbles attached on the surface. He formulated the two driving mechanisms and the surface wettability (contact angle ϕ , given in $^\circ$) in a rather simple correlation depicted in (1). The bubble departure diameter is increasing with the contact angle and with the surface tension while it decreases with gravity and density difference that define buoyancy potential. The expression in the square root is hereafter

$$D_{BD} = 0.0208 \cdot \phi \cdot \sqrt{\frac{\sigma}{g \cdot (\rho_l - \rho_v)}} \quad (1)$$

addressed the characteristic length. The importance of the contact angle (Figure 1) has been confirmed also experimentally several times. Most recently, Nam et al. [10] demonstrated by the use of superhydrophilic surface with artificial nucleation sites a significant decrease of bubble departure diameter with decreasing contact angle. In order to balance the evaporation rate with smaller bubbles their generation has to become more numerous. In fact, different wettability does not only affect the bubble departure diameter but it has a significant impact on the release frequency as well. Moreover, boiling surface and wall material to a certain depth have been shown to have an important role in heat partitioning during the boiling heat transfer and affect the occurrence of the critical heat flux phenomenon [11]. Figure 2 demonstrates how different contact angles affect bubble growth and bubble dynamics on boiling surfaces. In the absence of fluid motion the terminal diameter of a growing bubble (at a given contact angle) before departure from the boiling surface is obtained from the equilibrium of buoyancy and surface tension forces (Figure 2). Bubble departure diameter is yet to be deduced from the volume of the spherical cap of the growing bubble just before departure. Intuitively, the shallower the cap the bigger discrepancy between the size of the growing bubble and the bubble departure diameter is expected. Rather high void fraction is also expected in the near proximity to the liquid repellent surfaces as they spread the generated vapour on larger area. Intense wall superheat is therefore expected and may lead to an early occurrence of a dry-out phenomenon as the boiling surface encased in an insulated vapour blanket tends to remove heat less efficiently from the source compared to the well wetting surface.

Nevertheless, there are many other forces acting on the bubbles attached to the heating surface. If the liquid flows around the bubble two additional forces may appear instantaneously. Interphase drag presents the response of the bubble geometry on the wall to the resistance of the fluid flow. This force is proportional to a projected area of the vapour bubble in the direction of the flow, to the liquid density, to a drag coefficient, and to the square of the liquid velocity. Of course, any force that is acting on the vapour slug may distort its shape causing the drag coefficient and the projected area to change (Figure 3). On the other hand, the liquid flow above the vapour bubble induces also the lift force that acts perpendicular to the direction of the relative motion. Here, the presence of a rotational continuous phase plays an important role. Another important force during

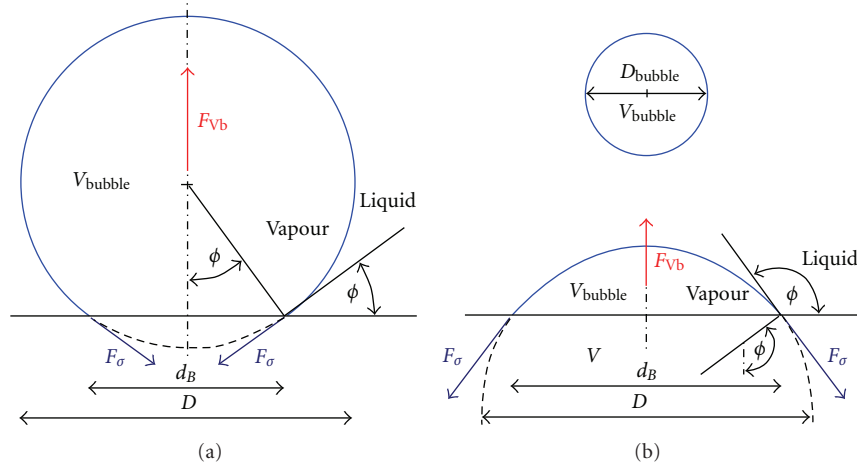


FIGURE 1: Spherical bubble in stagnant fluid on hydrophilic (a) and hydrophobic surface (b). D stands for virtual bubble (sphere) defined with vapour slug interface curvature while D_{bubble} stands for bubble departure diameter.

the intense vaporisation or/and intense condensation occurs due to the momentum transfer between the liquid and the vapour phase (Figure 3). Other agents, such as external force, virtual mass force, and wall lubrication force on the moving bubbles, may also take place during bubble growth and after departure.

Considering the Fritz [3] correlation, the equilibrium equation for the surface tension and the buoyancy force for the spherical bubble on the heating surface (Figure 1) can be written as

$$\begin{aligned} & \sigma \cdot \pi \cdot D \cdot \sin \phi \\ &= (\rho_l - \rho_v) \cdot g \cdot \frac{\pi \cdot (2 + 3 \cos \phi - \cos^3 \phi)}{24} \cdot D^3. \end{aligned} \quad (2)$$

Hence bubble's sphere diameter can be expressed as

$$D = \sqrt{\frac{24 \cdot \sin \phi}{(2 + 3 \cos \phi - \cos^3 \phi)} \cdot \frac{\sigma}{(\rho_l - \rho_v) \cdot g}}. \quad (3)$$

Introducing the sphere volume to the vapour volume ratio, the base diameter to the sphere diameter ratio ($\sin \Phi$), and the characteristic length into the equation above, one gets

$$D = \sqrt{6 \cdot \frac{V}{V_{\text{bubble}}} \cdot \sin \phi \cdot l_0}. \quad (4)$$

Assumption of the spherical bubble formation is justified with small vapour volumes generated on the heated surface. The smaller is the bubble, the higher is the relative pressure within the bubble. In fact, the smaller is the vapour volume, the more dominant is the surface tension force responsible for shaping the spherical bubble. As long as the generated vapour remains in contact with a solid wall, the slug takes over the shape of a spherical cup with considerably bigger sphere diameter particularly when hydrophobic surfaces are considered. Since the volume of the departing bubble is the

same as the one of the spherical cup its diameter can be calculated as

$$D_{\text{bubble}} = D \cdot \left(\frac{2 + 3 \cos \phi - \cos^3 \phi}{4} \right)^{1/3}. \quad (5)$$

Rearranging (3) and (4) into (5) gives a more general expression for calculation of the bubble departure diameter that depends on the characteristic length and the contact angle:

$$D_{\text{bubble}} = l_0 \cdot \left(\frac{864 \cdot \sin^3 \phi}{2 + 3 \cos \phi - \cos^3 \phi} \right)^{1/6}. \quad (6)$$

Equations (3) and (4) calculate virtual sphere diameter associated to the bubble interface curvature just before departure. Bubble departure diameter D_{bubble} calculated in (5) and (6) together with the diameter of "sphere" is plotted in Figure 4 along with the data obtained from the Fritz correlation. Calculated results give rather different absolute values but they all show the tendency of increasing bubble diameter with contact angle. In fact, the more hydrophilic surface we adopt the smaller is the contact angle and thus the smaller is the surface tension force component acting toward the wall. The propensity of the hydrophilic surface to wet the exposed area with the liquid tends to displace bubbles at smaller size. Indeed, the smaller is the contact angle the smaller is the discrepancy between the calculated diameter of the growing bubble (virtual sphere) and the departing bubble. Despite monotonous increase of the bubble departure diameter with the contact angle, the geometry change from the growing bubble into the departing bubble becomes more significant at bigger contact angles. Therefore, prediction uncertainty has been analysed in order to validate the prediction capability of (4) and (6) over entire

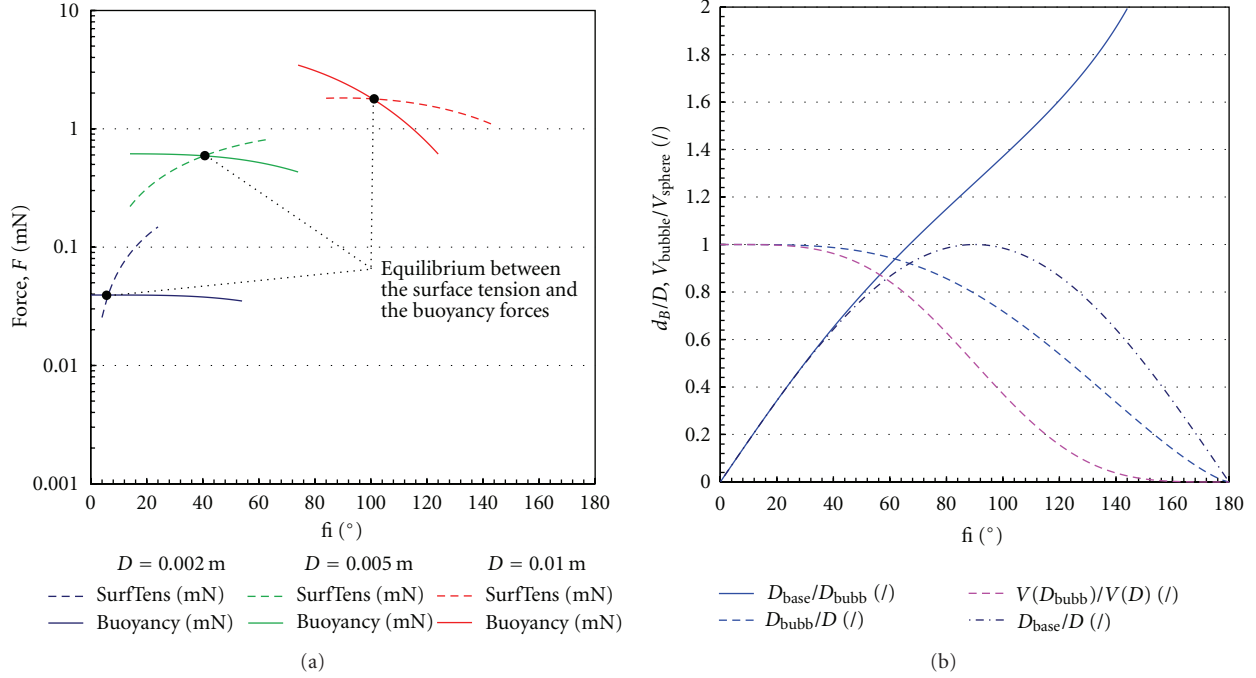


FIGURE 2: Surface tension and buoyancy force profiles for three different (virtual) bubble diameters over entire span of contact angles (a), and comparison of characteristic relative quantities (b).

span of contact angles. In this context, overall uncertainty has been calculated as

$$\delta D_{\text{bubble}} = \sqrt{\sum_{i=1}^n \left(\frac{\partial D_{\text{bubble}}(x_i)}{\partial x_i} \cdot \delta x_i \right)^2}, \quad (7)$$

where partial derivatives of bubble departure diameter were derived as follows:

$$\begin{aligned} \frac{\partial D_{\text{bubble}}}{\partial \phi} &= \frac{1}{2} \cdot 864^{1/6} \cdot \left(\frac{\sin^3 \phi}{2 + 3 \cos \phi - \cos^3 \phi} \right)^{7/6} \\ &\quad \cdot \left(\frac{\cos \phi \cdot (2 + 3 \cos \phi - \cos^3 \phi)}{\sin^4 \phi} + 1 \right) \cdot l_0, \\ \frac{\partial D_{\text{bubble}}}{\partial \sigma} &= \frac{1}{2} \cdot \left(\frac{864 \cdot \sin^3 \phi}{2 + 3 \cos \phi - \cos^3 \phi} \right)^{1/6} \cdot l_0 \cdot \frac{1}{\sigma}, \\ \frac{\partial D_{\text{bubble}}}{\partial \Delta \rho} &= -\frac{1}{2} \cdot \left(\frac{864 \cdot \sin^3 \phi}{2 + 3 \cos \phi - \cos^3 \phi} \right)^{1/6} \cdot l_0 \cdot \frac{1}{(\rho_L - \rho_V)}, \\ \frac{\partial D_{\text{bubble}}}{\partial g} &= -\frac{1}{2} \cdot \left(\frac{864 \cdot \sin^3 \phi}{2 + 3 \cos \phi - \cos^3 \phi} \right)^{1/6} \cdot l_0 \cdot \frac{1}{g}. \end{aligned} \quad (8)$$

Error band for a given surface contact angle was estimated to be 3° whereas the variations in the surface tension and liquid to vapour density difference were obtained from the fluid property deviation associated to the measured temperature uncertainty of 0.3°C . Indeed, density difference and surface tension variations for boiling water at atmospheric pressure

were calculated as 10 kg m^{-3} and 0.64 mN m^{-1} , respectively, while gravity variation was assumed 0.026 m s^{-2} . However, a negligible contribution from the gravity associated variations can be observed in the Figure 5.

Further to the critical assessment of the bubble departure diameter calculation similar analysis has been performed to estimate the reliability of the growing bubble (sphere) diameter prediction. Uncertainty values are plotted in Figures 4 and 5 for both bubble departure diameter and the diameter of the virtual sphere. Relative uncertainty of the spherical cup geometry prediction is monotonously decreasing and settles just beneath 1% at the highest contact angles, whereas the bubble departure diameter prediction error encounters global minimum of around 1.5% at moderately water repellent surfaces (Figure 5).

It can be seen from Figure 5 that prediction of the bubble departure diameter seems to give lower uncertainty values as compared to the growing bubble geometry but for the highest contact angles. In fact, the bubble departure diameter for the present boundary conditions (boiling water, 1 bar) is most accurately predicted on the hydrophobic surfaces with contact angles around 110° . Interestingly, deviation from defining the exact contact angles and the accurate fluid properties has a rather different effect on the final prediction accuracy of either bubble departure diameter or bubble growth geometry. Contact angle variation at the small nominal values, for example, has strong impact on both overall geometry uncertainties. On the contrary to the similar trend of the bubble departure diameter prediction capability at high contact angles, a negligible influence of the contact angle uncertainty is found at the highest nominal

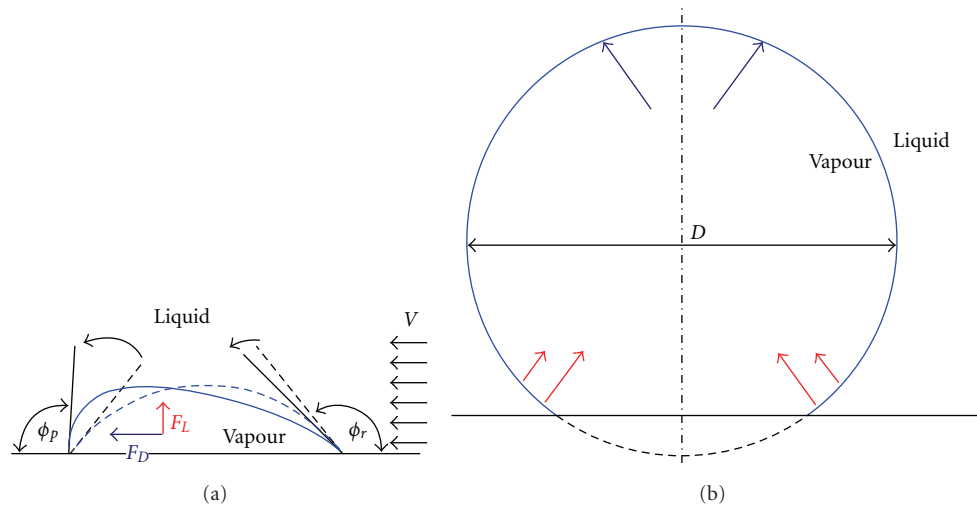


FIGURE 3: Demonstration of a drag force and a lift force acting on a vapour slug (a), and momentum change due to the evaporation and condensation on the liquid vapour interface within the bubble (b).

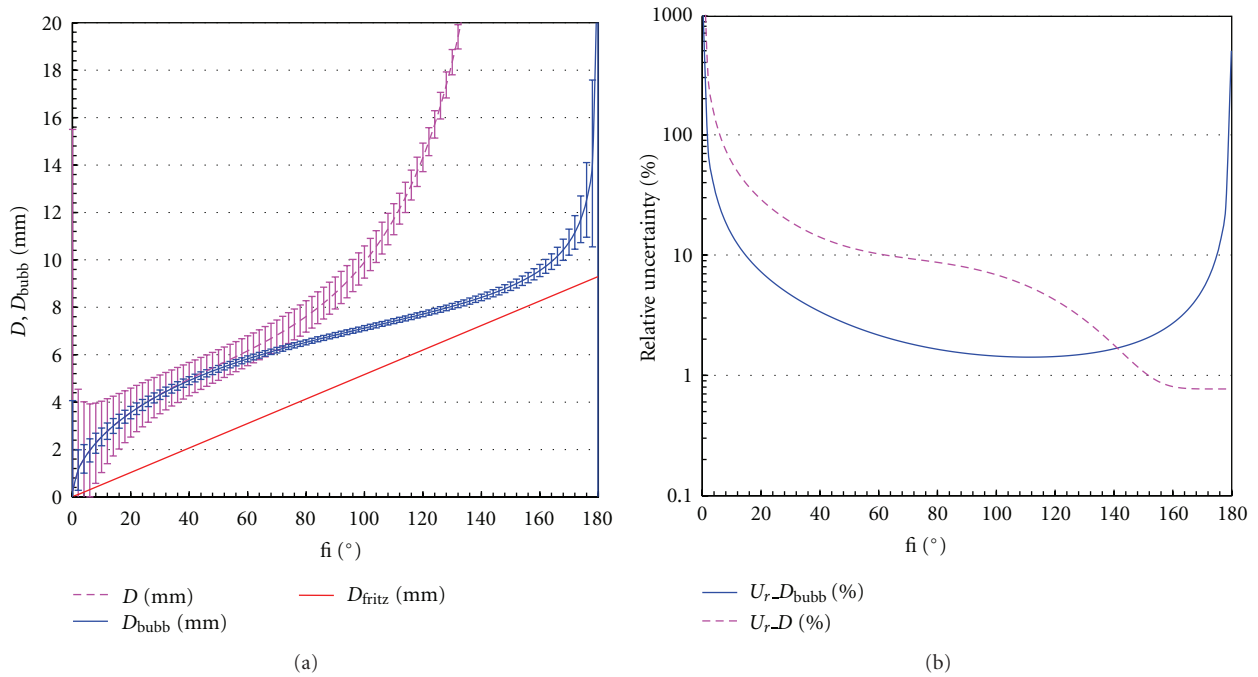


FIGURE 4: Calculated diameters with error bars for growing bubble (virtual sphere) and departing bubble with diameter calculated from Fritz correlation (a). Relative uncertainty of the calculated bubble departure diameter and virtual sphere diameter (b).

values when spherical cup geometry is analysed. Moreover, the smallest influence of the contact angle variation on the overall bubble departure diameter prediction uncertainty can be expected for moderate contact angles. It can be seen from Figure 5 that overall prediction uncertainty of the bubble departure diameter is entirely controlled with contact angle uncertainty. However, the same observation, but for the highest contact angles, can be drawn for calculated virtual sphere diameter. There, the surface tension and the density variation seem to take over the dominant contribution

to overall uncertainty. Finally, gravity variation has been shown to have insignificant impact on the overall prediction uncertainty for growing and departing bubbles and over entire range of heating surfaces.

Figure 4 shows calculated bubble departure diameters by Fritz [3] and by (6) as well as the diameter of the growing bubble (virtual sphere). Error bars are depicting overall uncertainty values for the two geometries. It can be seen from Figure 4 that prediction ranges for bubble diameters calculated with either (4) or (6) are overlapping for contact

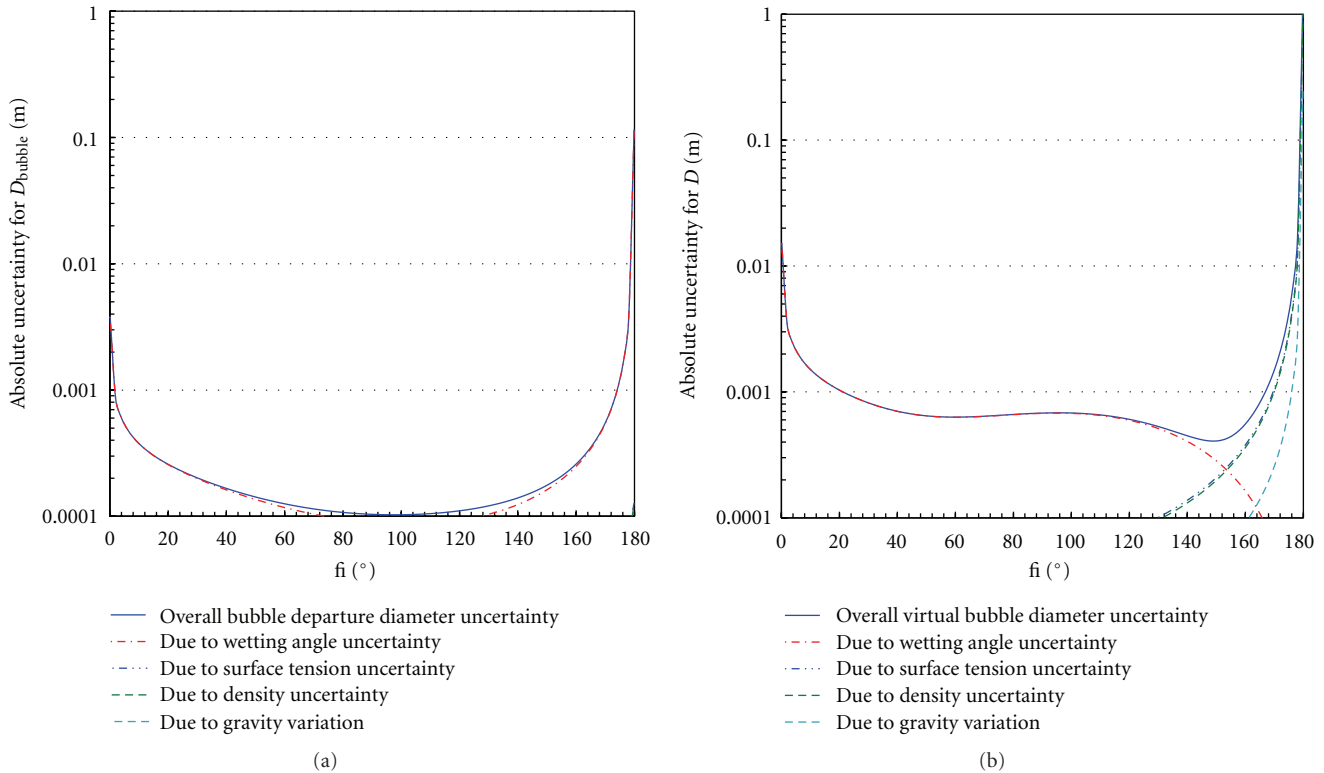


FIGURE 5: Calculated uncertainty values for bubble departure diameter (a) and the diameter of the virtual sphere defined by the spherical cup (b).

angles smaller than 75° . Indeed, care must be taken at water repellent surfaces, to address appropriate bubble geometry in the calculus. Nevertheless, correlations based on mechanistic modelling of the two dominant mechanisms are not deemed highly effective for extreme contact angles.

3. Conclusion

Present paper presents qualitative estimation of the bubble departure diameter prediction modelling through the calculated uncertainty values over a wide range of test conditions. Despite some new notations of force balance the aim of this study is not to offer another correlation for bubble diameter prediction but to give critical arguments for quality assessment of the existing modelling. In fact, the main purpose of the present work was to offer a methodological approach that would help estimating the prediction constraints of the chosen correlations. It has been shown that the inlet boundary conditions with a realistic experimental accuracy may lead to a significant deviation in prediction of bubble departure and bubble growth diameters even in the absence of the fluid motion. Uncertainty values for bubble departure diameter correlation were calculated below 3% for most of the heating surfaces. On the other hand, despite monotonously decreasing relative uncertainty of the growing bubble (virtual sphere), it gives higher uncertainty values for most contact angles but on highly water repellent surfaces. Intuitively one can expect that

introduction of new driving mechanisms in the modelling would further increase the prediction uncertainty.

References

- [1] R. T. Lahey, "A mechanistic Subcooled boiling model," in *Proceedings of the 6th International Heat Transfer Conference*, vol. 1, Toronto, Canada, 1978.
- [2] N. Kurul and M. Z. Podowski, "Multidimensional effects in forced convection subcooled boiling," in *Proceedings of the 9th International Heat Transfer Conference*, Jerusalem, Israel, 1990.
- [3] W. Fritz, "Maximum volume of vapor bubbles," *Physikalische Zeitschrift*, vol. 36, pp. 379–384, 1935.
- [4] R. Cole and W. Rohsenow, "Correlation of bubble departure diameters for boiling of saturated liquids," *Chemical Engineering Progress*, vol. 65, pp. 211–213, 1969.
- [5] V. I. Tolubinski and D. M. Kostanchuk, "Vapor bubbles growth rate and heat transfer intensity at subcooled water boiling," in *Proceedings of the 4th International Heat Transfer Conference*, vol. 5, Paper no. B2.8, Paris-Versailles, France, 1970.
- [6] G. Kocamustafaogullari, "Pressure dependence of bubble departure diameter for water," *International Communications in Heat and Mass Transfer*, vol. 10, no. 6, pp. 501–509, 1983.
- [7] D. Gorenflo, V. Knabe, and V. Bieling, "Bubble density on surfaces with nucleate boiling-it's influence on heat transfer and burnout heat fluxes at elevated saturation pressures," in *Proceedings of the 8th International Heat Transfer Conference*, vol. 4, pp. 1995–2000, Hemisphere, Wash, USA, 1986.
- [8] C. E. Estrada-Perez and Y. A. Hassan, "PTV experiments of subcooled boiling flow through a vertical rectangular

- channel,” *International Journal of Multiphase Flow*, vol. 36, no. 9, pp. 691–706, 2010.
- [9] V. K. Dhir, “Mechanistic prediction of nucleate boiling heat transfer—achievable or a hopeless task?” *Journal of Heat Transfer*, vol. 128, no. 1, pp. 1–12, 2006.
- [10] Y. Nam, E. Aktinol, V. K. Dhir, and Y. S. Ju, “Single bubble dynamics on a superhydrophilic surface with artificial nucleation sites,” *International Journal of Heat and Mass Transfer*, vol. 54, no. 7-8, pp. 1572–1577, 2011.
- [11] G. J. Kirby, R. Stainiforth, and L. H. Kinner, “A visual study of forced convection boiling—2: flow patterns and burnout for a round test section,” Tech. Rep. AEEW-R-506, UKAEA, Winfrith, UK, 1967.

Research Article

CHF Phenomena by Photographic Study of Boiling Behavior due to Transient Heat Inputs

Jongdoc Park,¹ Katsuya Fukuda,² and Qiusheng Liu²

¹*Oshima National College of Maritime Technology, 1091-1 Komatsu, Suo-Oshima-cho, Oshima-gun, Yamaguchi 742-2106, Japan*

²*Graduate School of Maritime Sciences, Kobe University, 5-1-1 Fukueminami, Higashinada, Kobe 658-0022, Japan*

Correspondence should be addressed to Jongdoc Park, park@oshima-k.ac.jp

Received 7 May 2012; Revised 31 August 2012; Accepted 18 September 2012

Academic Editor: Eckhard Krepper

Copyright © 2012 Jongdoc Park et al. This is an open access article distributed under the Creative Commons Attribution License, which permits unrestricted use, distribution, and reproduction in any medium, provided the original work is properly cited.

The transient boiling heat transfer characteristics in a pool of water and highly wetting liquids such as ethanol and FC-72 due to an exponentially increasing heat input of various rates were investigated using the 1.0 mm diameter experimental heater shaped in a horizontal cylinder for wide ranges of pressure and subcooling. The trend of critical heat flux (CHF) values in relation to the periods was divided into three groups. The CHF belonging to the 1st group with a longer period occurs with a fully developed nucleate boiling (FDNB) heat transfer process. For the 2nd group with shorter periods, the direct transition to film boiling from non-boiling occurs as an explosive boiling. The direct boiling transition at the CHF from non-boiling regime to film boiling occurred without a heat flux increase. It was confirmed that the initial boiling behavior is significantly affected by the property and the wettability of the liquid. The photographic observations on the vapor bubble behavior during transitions to film boiling were performed using a high-speed video camera system.

1. Introduction

Understanding of the transient boiling heat transfer and CHF phenomena caused by increasing heat inputs in subcooling water at high pressures is necessary to predict the likelihood of a severe, design-based accident in a water-cooled nuclear reactor. The typical trend of the CHF values in relation to the heat generation rates shown with period is as follows: the CHF gradually increases to a maximum value from a steady-state CHF, and then the CHF quickly decreases to a minimum value, and finally, the CHF again increases, accompanied by a decrease in period. The steady-state CHF corresponds to the CHF due to the heat input with a period τ of 20 s. This trend suggests that there exists another mechanism of CHFs for shorter periods different from the thermal-hydrodynamic instability (HI) model firstly suggested by Kutateladze [1] and Zuber [2]. The CHFs for the shorter periods at which direct or semi direct transitions to film boiling occurred in transient conduction regime due to a quasi-steadily increasing or increasing heat input for the liquids including water. A direct transition from non-boiling convective regime to film boiling one was reported by

Avksentyuk and Mamontova [3] and Kutateladze et al. [4] in liquid metals and wetting liquids as some peculiarities of CHF. However, A few key aspects of the complex CHF phenomena for the heat inputs with short periods are as yet not fully understood.

The direct transition from a non-boiling regime such as natural convection and transient conduction regimes to film boiling without nucleate boiling was observed by Sakurai et al. [5, 6]. They carried out the experiments of the CHFs for the heat inputs with various periods on a platinum horizontal cylinder in liquid nitrogen at various pressures and found that direct transition to film boiling occurred in transient conduction regime. The transition mechanism to film boiling was confirmed by a photographic study on the vapor bubble and vapor film behavior on the cylinder surface by Sakurai et al. [7]. They concluded by the photographs that the semi-direct transition from conduction regime to film boiling with nucleate boiling due to the rapidly increasing heat inputs in water occurs due to heterogeneous spontaneous nucleation (HSN) in originally flooded cavities with or without nucleate boiling at around the lower limit of HSN surface superheat.

The measured CHF related to subcoolings for water, liquid nitrogen, and liquid helium with pressures as a parameter disagreed with the corresponding values derived from the existing correlations given by Kutateladze [1] based on the model of CHF resulting from hydrodynamic instability. However, those data were well described by the newly derived subcooled pool boiling CHF correlations derived by Sakurai et al. [6] by assuming that CHFs occur due to the hydrodynamic instability (HI), or the heterogeneous spontaneous nucleation (HSN) in originally flooded cavities with liquid on the experimental heater surface. Chang et al. [8] measured CHF and corresponding surface superheat at which the transition from natural convection regime to film boiling in a pool of FC-87 occurs and also measured minimum film boiling heat flux and corresponding surface superheat. They concluded that the film boiling incipience at the transition point and minimum film boiling at collapse point occur due to the lower limit of HSN in wetting liquid of FC-72 and FC-87. Fukuda et al. [9] investigated the effect of the surface conditions of the platinum experimental cylinders in a pool of water on the two different surface conditions with mirror surface (MS) finished using alumina suspension and rough surface (RS) finished using the #3 emery paper. As the result, it was confirmed that the photographs of vapor bubbles and film behavior during transitions to film boiling in water were not different with each other not only for quasi-steadily increasing heat input but also for rapidly increasing one. Recently, the pool boiling CHF for various liquids using a 1.0 mm diameter platinum horizontal cylinder was measured to investigate the boiling behavior of transient phenomena [10]. It was confirmed that the vapor film behavior during transition to fully developed nucleate boiling or direct transition at the CHF to film boiling was significantly affected by the properties of boiling liquid and the wettability between liquids and surface of heater. However the mechanism has not been clarified yet.

The present work is to make clear the transition phenomena to film boiling at steady and transient CHF in nonwetting and wetting liquids. The generalized phenomena for the transitions to film boiling from single-phase conduction or transient conduction and fully or insufficiently developed nucleate boiling due to exponential heat generation rates for wide range of subcoolings and pressures were investigated in water, ethanol, and FC-72, adding the photographic approach on the vapor bubble and vapor film behavior on the cylinder surface by using a high-speed video camera.

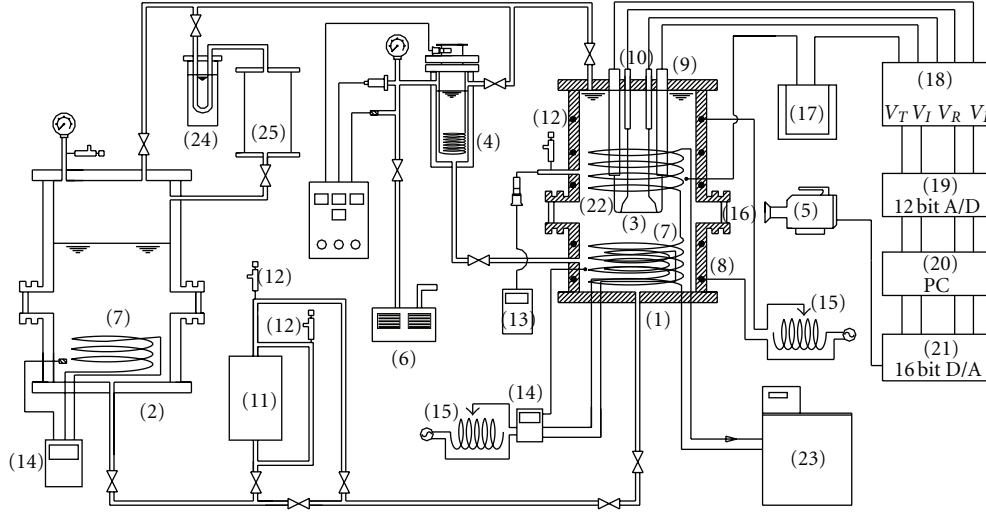
2. Experimental Apparatus and Method

2.1. Pool Boiling Apparatus. The schematic diagram of the experimental apparatus is shown in Figure 1. It mainly consists of a boiling vessel, an experimental heater shaped in a horizontal cylinder, a pressurizer, a device to control the heat generation rate, a data measurement and processing system, and a high-speed video camera.

The boiling vessel has inspection windows and is made of stainless steel; it has an inner diameter of 200 mm and a height of 600 mm. The experimental heater is made of platinum wire and is a diameter of 1.0 mm which is horizontally

mounted in the vessel. The effective length of the heater between the potential taps is about 31 mm. The heater was annealed in order to maintain an even properties and its electrical resistance versus temperature relation was calibrated in water and glycerin baths using a precision double bridge circuit. The calibration accuracy was estimated to be within ± 0.5 K.

2.2. Experimental Method and Procedure. The experimental heater was heated electrically by using a fast response, direct current source (max. 700 A) controlled by a digital computer so as to give a desired time function for the heat input. The average temperature of the heater was measured by resistance thermometry using the heater itself. A double bridge circuit with the heater as a branch was first balanced at the bulk liquid temperature. The output voltages of the bridge circuit, together with the voltage drops across the potential taps of the heater and across a standard resistance, were amplified and passed through analog-to-digital (A/D) converters installed in the computer. These voltages were simultaneously sampled at a constant time interval that was changed depending on the period. The fastest sampling speed of the A/D converter is $5 \mu\text{s}/\text{channel}$. The average temperature between the potential taps was obtained by using the previously calibrated resistance-temperature relation. The heat generation rate of the heater was determined from the current to the heater and the voltage difference between potential taps on the heater. The surface temperature was obtained by solving the conduction equation in the heater under the conditions of the average temperature and heat generation rate. The instantaneous surface heat flux was obtained from the heat balance equation for a given heat generation rate. The CHF was determined at a start point where the average temperature rapidly increases up to the preset temperature by using a burnout detector. The analog computer computes the instantaneous mean temperature of the heater and it cuts off the power supply automatically. The experimental error was estimated to be about ± 1 K in the heater surface temperature and $\pm 2\%$ in the heat flux. A high-speed video camera system (1000 frames/s with a rotary shutter exposure of $1/10000$ s) was used to observe the boiling phenomena and to confirm the start of boiling on the heater surface. The liquid used in the experiment was degassed by keeping them boiling at least for 30 minutes in the liquid feed tank. Vapor was recovered to the pool with a water-cooled condenser. The liquid was fully filled in the boiling vessel with the free surface only in the pressurizer and liquid feed tank. Liquid temperatures in the boiling vessel and in the pressurizer were separately controlled to realize the desired saturated and subcooled conditions. Each heat flux and surface superheat was calculated by the data processing system according to time. The heat input was raised with exponential function, $Q = Q_0 \exp(t/\tau)$. Q_0 is initial heat generation rate, t is time, and τ is period. Period τ is an e-fold time that corresponds to heat generation rate with the exponential increasing rate. In this study, heat transfer processes for the periods longer than 10 s are considered as quasi-steady-state one, because the non-boiling region well agreed with natural convection curve, and all CHFs



- | | |
|-----------------------------|-----------------------------|
| (1) Boiling vessel | (14) Temperature controller |
| (2) Auxiliary tank | (15) Slide rheostat |
| (3) Experimental heater | (16) Observation window |
| (4) Pressurizer | (17) Cold junction |
| (5) High-speed video camera | (18) Heating system |
| (6) Vacuum pump | (19) A/D converter |
| (7) Sheathed heater | (20) Personal computer |
| (8) Microheater | (21) D/A converter |
| (9) Current conductor | (22) Spiral cooling tube |
| (10) Potential conductor | (23) Cooler |
| (11) Pressure pump | (24) Condenser |
| (12) Pressure relief valve | (25) Receive tank |
| (13) Pressure gauge | |

FIGURE 1: Schematic diagram of experimental apparatus.

TABLE 1: Experimental condition.

Parameter	Condition
Heater	Platinum wire
Liquid	Ethanol, water, FC-72
Pressure	101.3 kpa–1082 kpa
Subcooling	0 K–60 K
Period	0.005 s–20 s

measured for the heat inputs with periods longer than 10 s are almost the same. Table 1 shows the experimental conditions.

2.3. Typical Boiling Heat Transfer Process. Figure 2 shows typical changes in the wall temperature of platinum wire, T_w , and heat flux, q , with time for an exponential heat generation rate, Q , with a period of 8.2 s at a pressure of 494 kPa under saturated conditions in ethanol. The heat flux, q , increases with an exponential increase in the heat generation rate, Q .

After the point when boiling begins, q_{in} , the heat flux, shows a rapid overheating and decrease regime caused by a bump of vapor bubbles and liquid flow on the cylinder surface. The q increases again exponentially to reach the critical heat flux point, q_{cr} (=CHF). T_w also increases with an increase in Q . T_w continues to increase up to T_{ov} (called the overshoot point) then rapidly decreases before increasing once again, this time at a low rate. When q reaches CHF, T_w rapidly increases with time.

Figure 3 shows the typical boiling curve on a graph of $\log q$ versus $\log \Delta T_{sat}$ for the experimental run shown in Figure 2. The surface superheat ΔT_{sat} is defined by the difference between the surface temperature, T_w , of the heater and the saturation temperature, T_{sat} , of liquid corresponding to the system pressure. As shown in the figure, heat flux, q , increases at a rate on the natural convection curve [11] in a non-boiling regime. After q_{in} , the incipience of boiling, the surface superheat rapidly decreases, and q increases along the fully-developed nucleate boiling (FDNB) regime and reaches the CHF point, q_{cr} . At that point, the transition to film boiling occurs.

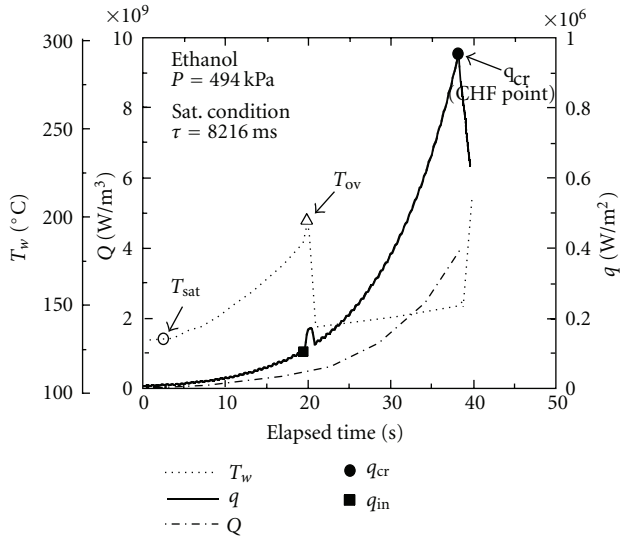


FIGURE 2: Illustrative time traces of heat generation rate, Q ; wall temperature of wire, T_w ; and heat flux, q .

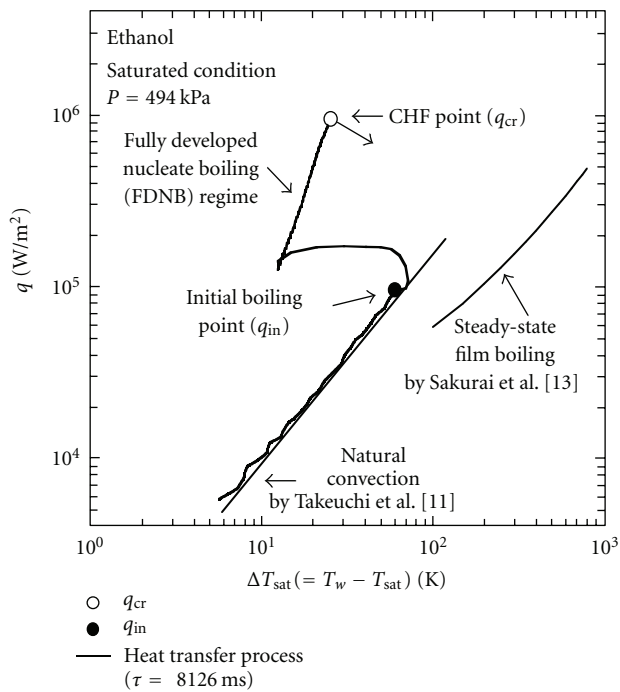


FIGURE 3: Boiling heat transfer process from non-boiling to fully developed nucleate boiling.

3. Experimental Results and Discussion

3.1. Typical Boiling Heat Transfer in Ethanol

3.1.1. Direct Transition Phenomenon. Figure 4 shows the transient phenomenon on a graph of heat flux, q , versus surface superheat, ΔT_{sat} , at a pressure of 101.3 kPa and a period of 0.1 s in saturated ethanol. The surface superheat ΔT_{sat} is defined by the difference between the surface temperature,

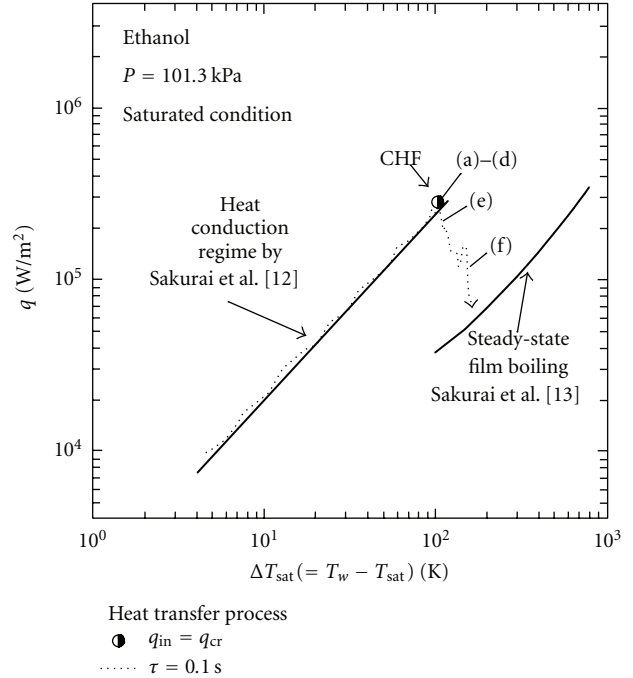


FIGURE 4: Boiling heat transfer processes from non-boiling to film boiling under saturated condition in ethanol. Photographs shown in Figure 5 were taken at points of Figures 5(a) to 5(f) on the graph.

T_w , of the heater and the saturation temperature, T_{sat} , of liquid corresponding to the system pressure. The heat conduction curve derived by Sakurai and Shiotsu [12], and the steady-state film boiling curve derived by Sakurai et al. [13] are also shown in the figure for comparison. The boiling process caused by an exponentially increasing heat input with a period of 0.1 s at atmospheric pressure shows that the q value increases along the natural convection heat transfer curve, and the boiling occurs at a surface superheat point of 100 K, and then shows a transition directly to film boiling without passing the nucleate boiling. The initial boiling temperature gradually decreased with an increase in system pressure based on experimental data. It is considered that the direct boiling transition on the heater surface from non-boiling to film boiling is due to the heterogeneous spontaneous nucleation (HSN) in previously flooded cavities on heater surface as suggested by Sakurai et al. [5, 6, 14].

Figure 5 gives a series of subsequent photographs from the moment of onset of a vapor phase to film boiling on a surface at a pressure of 101.3 kPa in saturated ethanol. Figure 5(a) is the onset of boiling on the cylinder. Figure 5(b) taken at 1 ms after the first one shows a vapor tube due to the explosive-like HSN in flooded cavities, and it covers the whole cylinder surface by the large vapor tube. Figure 5(c) taken at 2 ms after the first one shows thick vapor film concentrically covering the cylinder. The vapor bubbles are very rapidly growing and completely covering the surface of the cylinder within just a few milliseconds. The temperature difference of the surface superheat corresponding to Figures 5(a) to 5(c) is almost the same. Figure 5(d) taken

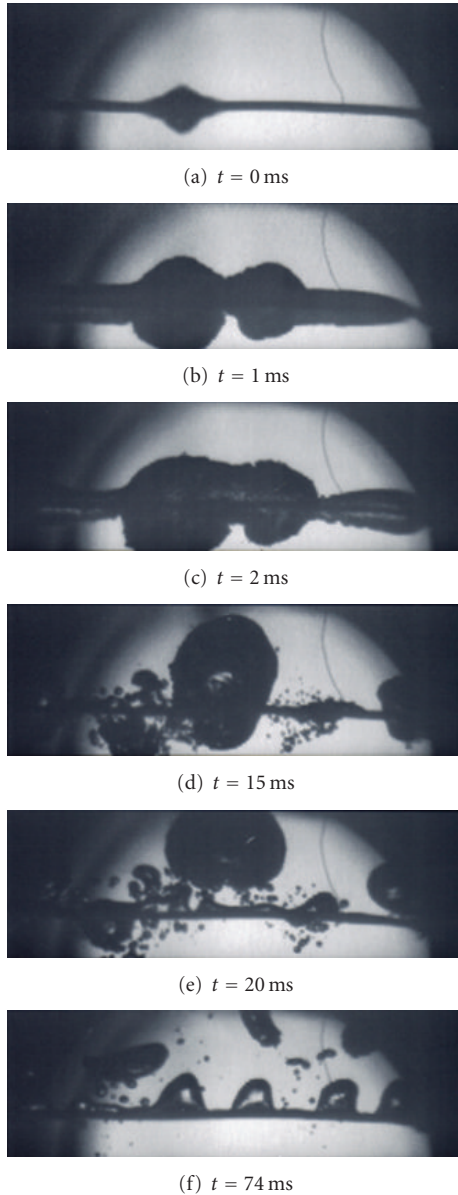


FIGURE 5: Vapor film behavior during direct transition to film boiling for a period of 0.1 s at a pressure of 101.3 kPa in saturated ethanol.

at 15 ms after the first one shows that the vapor bubbles collapse from the boiling initiation bubbles. Then, large vapor bubbles are broken away from the large vapor film by buoyancy force and move upward as shown in Figure 5(e). After detachment of the large vapor bubbles, solid-liquid contacts occur, and then new thin vapor film with the Taylor unstable wave on the upper part of the vapor-liquid interface covering the cylinder is formed by the explosive-like HSN on the places of solid-liquid contact and thin film boiling. At this moment the surface temperature starts increasing rapidly as a result of heat transfer deterioration. As shown in Figure 5(f), the behavior of vapor-liquid interface in film boiling on the cylinder similar to that for steady-state

film boiling on the cylinder is clearly observed after the detachment of large vapor bubbles.

3.1.2. Boiling Behavior for Wide Range of Pressures under Saturated Condition. Figure 6 shows vapor film behavior during transition to CHF at each pressure in saturated ethanol. A vertical axis shows heat flux until it reaches the critical heat flux, q_{cr} . It was compared when the fully developed nucleate boiling was occurred with quasi-steadily increasing heat input given by exponential time function. After the incipience of boiling, the tendency to become large vapor bubbles gradually from small ones is almost the same. And it can be confirmed that the diameter of vapor bubbles is small as it becomes high pressure. In 101.3 and 494 kPa, the large vapor tube-like explosive boiling is formed rapidly at initiation of boiling. In high pressure 1082 kPa, such a phenomenon did not occur but bubbles had spread smoothly from the center. It is because the boiling initiation superheat temperature at low pressure is high compared with that at high-pressure. It is considered that the bubbles are growing rapidly because the large quantity of heat is supplied suddenly from the thick superheated liquid layer covering the cylinder in low-pressure. That is why there is a tendency of foaming from a smaller bubble nucleus while the latent heat of vaporization becomes low, as it becomes high pressure (Sakurai et al. [14]).

The critical heat flux (CHF) in saturated condition was well dependent on system pressure. The diameter of bubbles becomes small by the increase in pressure, and then the supply of liquid to a heating surface becomes better so that transitions to film boiling occurred in higher heat flux.

3.1.3. Boiling Behavior for Wide Range of Subcoolings at the Pressure of 494 kPa. Figure 7 shows the vapor film behavior during transition to CHF for comparison to each subcooling at a fixed system pressure. It turns out that the vapor bubbles are formed and crushed immediately by low temperature of bulk liquid as the subcooling becomes high. And while heat flux goes up, the natural convection has occurred intensely as shown in the figure.

CHF was well dependent on the subcooling. As it becomes higher in subcooling, the sensible heat in order that it raises liquid temperature to the saturation temperature corresponding to the system pressure becomes more required, so that CHF becomes high. Moreover, since the diameter of bubbles becomes small, a heat input continues until the bubbles coalesce in the nucleate boiling region to form coalesced bubbles and transition to film boiling occurs. Therefore, it is thought that CHF increases as it becomes higher in subcooling.

3.2. Typical Boiling Heat Transfer in Water

3.2.1. Heat Transfer Processes under Saturated Condition in Water. Typical boiling heat transfer processes due to exponentially increasing heat inputs in water are shown in Figure 8 on a graph of heat flux, q , versus surface superheat, ΔT_{sat} . The steady-state natural convection curve derived by Takeuchi et al. [11], the heat conduction curve derived by

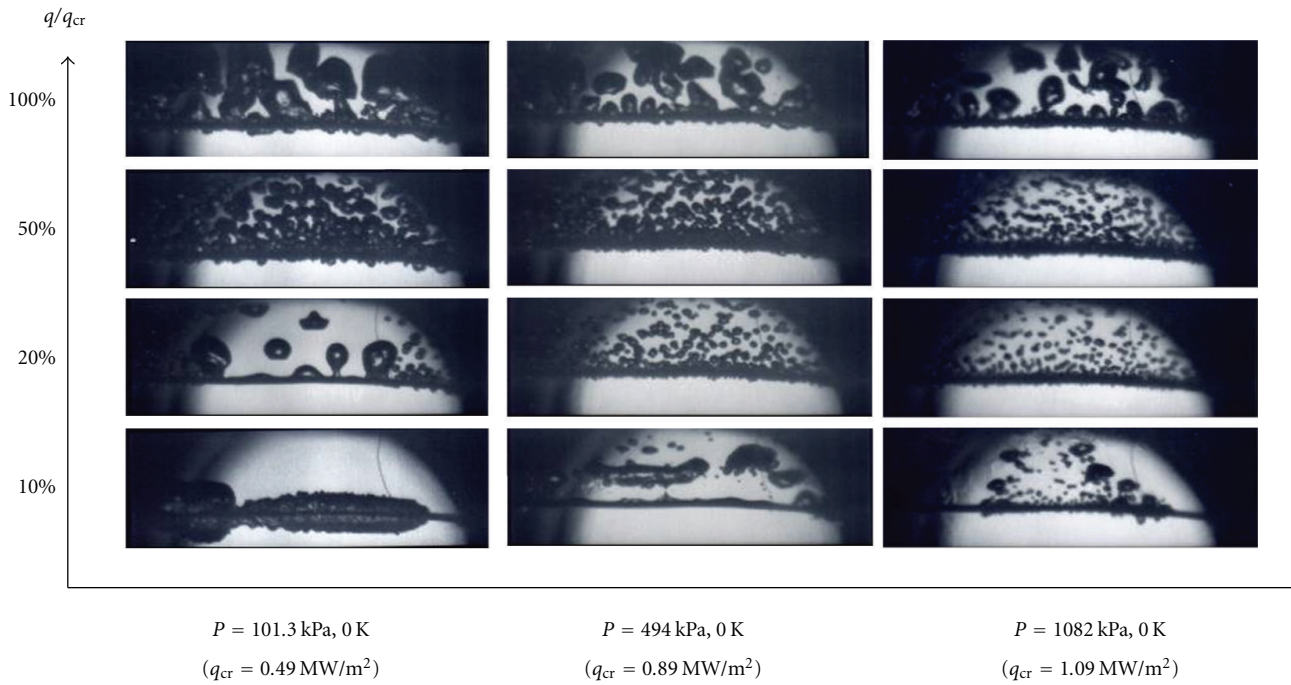


FIGURE 6: Vapor film behavior during transition to CHF at pressures of 101.3, 494, and 1082 kPa in saturated ethanol due to quasi-steadily increasing heat input given by exponential time function.

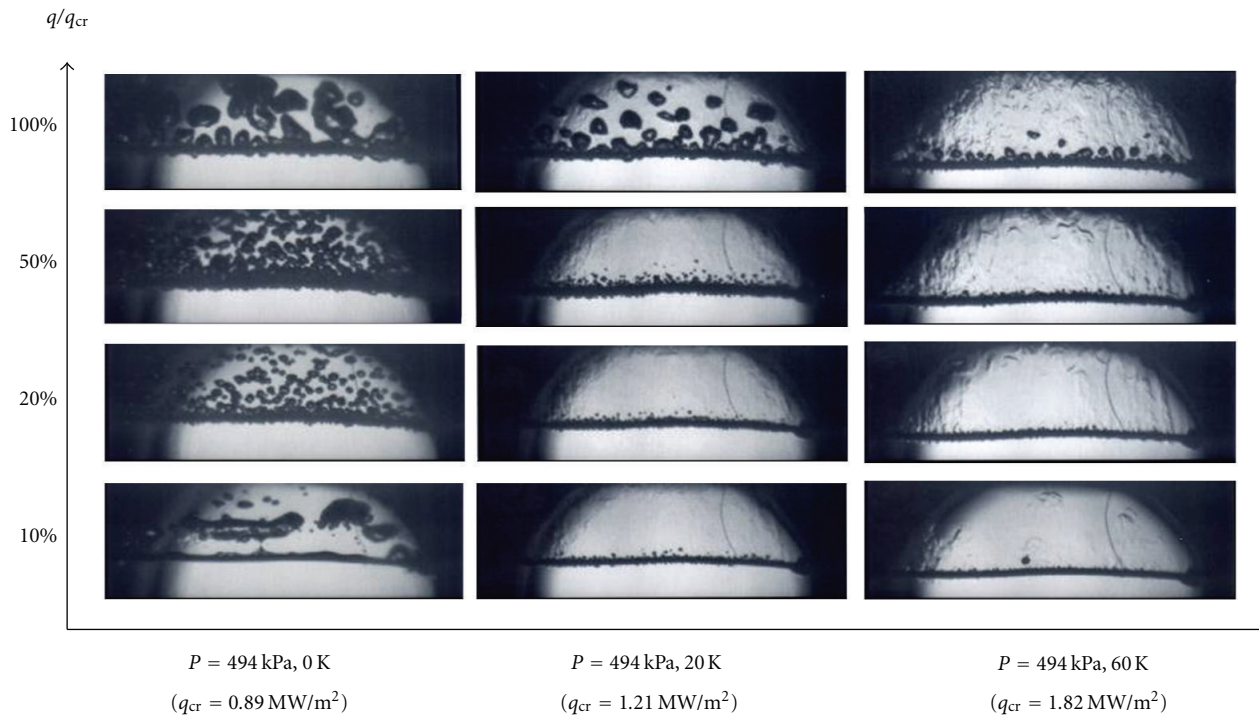


FIGURE 7: Vapor film behavior during transition to CHF at a pressure of 494 kPa for subcoolings of 0, 20 and 60 K in ethanol due to quasi-steadily increasing heat input given by exponential time function.

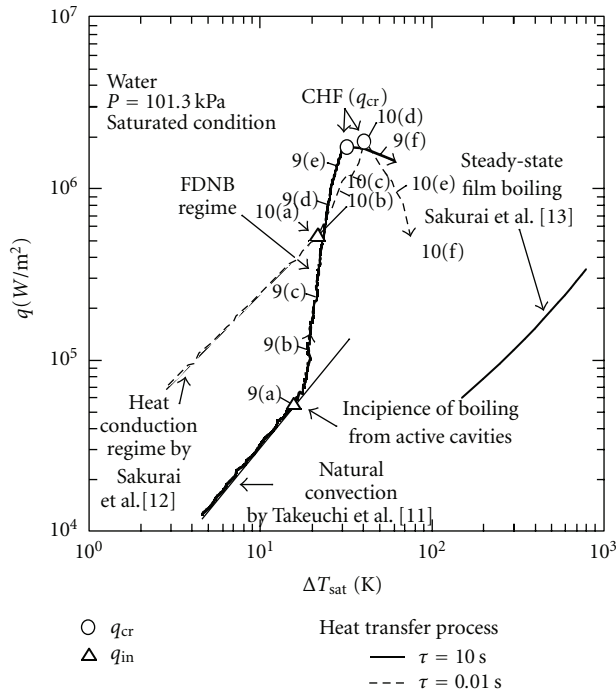


FIGURE 8: Heat transfer process for period $\tau = 10$ s and 0.01 s at atmospheric pressure in saturated water. Photographs shown in Figures 9 and 10 were taken at points of Figures 9(a) to 9(f) and Figures 10(a) to 10(f) on the graph, respectively.

Sakurai and Shiotsu [12] and the steady-state film boiling curve derived by Sakurai et al. [13] are also shown in the figure for comparison.

The heat transfer processes for periods of 10 s and 0.01 s at a pressure of 101.3 kPa are shown in the figure. The processes from non-boiling to film boiling are completely different from each other from period to period. It can be found that the processes up to initial boiling heat fluxes, q_{in} , are the natural convection regime for period of 10 s, and the heat conduction regime for period of 0.01 s as shown in the figure. It is recognized that the values of initial boiling heat flux, q_{in} , increase with a decrease in period; that is, they depend on the increasing rates of heat inputs. When an exponentially increasing heat input is applied to the heater immersed in the pool of water, the heater surface temperature and the heat flux increased. As shown in the figure, the heat transfer processes up to q_{in} show that heat flux, q , for the period of 10 s increases along the natural convection curve and natural convection heat transfer becomes predominant. As the period shortens, the heat conduction becomes predominant in heat transfer compared with the natural convection.

3.2.2. Photographs of Vapor Film Behavior during Transition to Nucleate Boiling in Water. Figure 9 is taken using a high-speed video camera for the vapor behavior on a horizontal cylinder during transition to nucleate boiling due to a slowly increasing heat input for a period of 10 s. The photographs in the figure are shown to confirm the assumptions where the corresponding points on the heat transfer process curve at

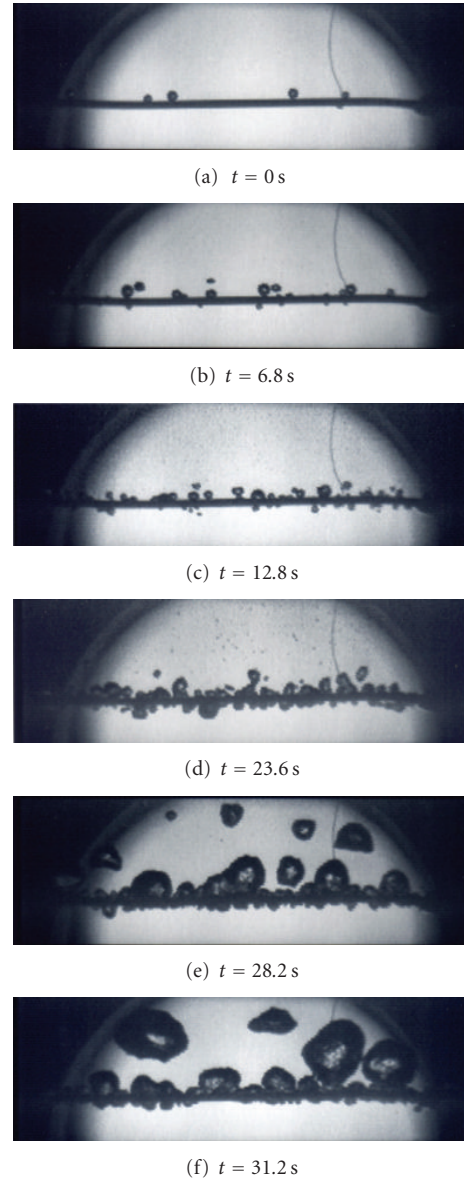


FIGURE 9: Vapor film behavior during transition to fully developed nucleate boiling (FDNB) for a period of 10 s at atmospheric pressure in saturated water.

the points of Figures 9(a) to 9(f) are shown in Figure 8 with a solid line. Figure 9(a) is the onset of boiling and it can be seen with a few initial vapor bubbles. Figures 9(b) and 9(c) are the photographs after the time passage of 6.8 s and 12.8 s from point (a), respectively. It takes a long time for the vapor bubbles to spread to the whole surface of the experimental heater as shown in the figure. The vapor bubbles around the heater occur from active cavities of entrained vapor that cause the increase of heat flux. After incipient boiling at a point which corresponds to the q_{in} , the surface superheat, ΔT_{sat} , does not change so much with an increase in heat input. As shown in Figure 9(d), the small bubble nucleus commences to coalesce in the nucleate boiling region to form coalesced bubbles. The detached coalesced bubbles

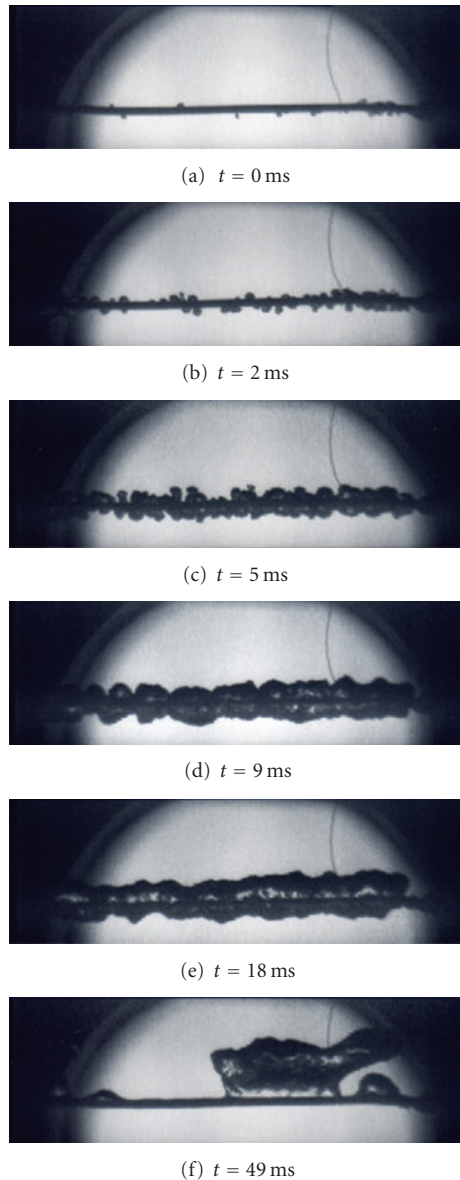


FIGURE 10: Vapor film behavior during semi-direct transition to film boiling for a period of 0.01 s at atmospheric pressure in saturated water.

continuously increase in size with increases in the heat flux at the points of Figures 9(e) to 9(f).

3.2.3. Photographs of Vapor Film Behavior during Semidirect Transition to Film Boiling in Water. Figure 10 shows the semi-direct transition from transient conduction regime to film boiling due to a rapidly increasing heat input for the period of 0.01 s. The CHF almost agrees with the quasi-steady-state CHF for the period of 10 s. The mechanism of semi-direct transition from transient conduction regime to film boiling was not solved for a long time. Sakurai et al. [5, 6] assumed that the mechanism of semi-direct transition to film boiling with slight nucleate boiling from active cavities occurs finally due to the HSN at around the lower limit

of HSN surface superheat in originally flooded cavities; the lower limit value was measured under the condition with prepressurization for a quasi-steadily increasing heat inputs. Figures 10(a) to 10(f) are shown to confirm their process. The corresponding points on the heat transfer curve on the q versus ΔT_{sat} graph for each photograph are shown in Figure 8 with a dashed line. Figure 10(a) is the photograph at point of Figure 10(a), which is the onset of boiling. It shows the cylinder in transient conduction regime with a few initial vapor bubbles. The time, t , beside each photograph shows the elapsed time after the time of first photograph, Figure 10(a). Figure 10(b) is the photograph after a time passage of 2 ms from point (a). Figures 10(b), 10(c), and 10(d) show vapor bubbles around the cylinder occurred from active cavities of entrained vapor which cause the rapid increase of heat flux without the detachment of vapor bubbles. The heat flux for Figure 10(d) is around the CHF. A large vapor film covers the cylinder including all the vapor bubbles from active cavities as shown in Figure 10(d). As seen in Figure 10(e), the large vapor film with the Taylor unstable wave on the top of the vapor film moves upward with a decrease in heat flux and an increase in surface superheat. After that, the large vapor bubbles are separated from the vapor film with the approximate interval of the most dangerous Taylor wave length and levitate in the liquid as seen in Figure 10(f). The heat flux approaches around minimum film boiling heat flux and then increases along the steady-state film boiling heat flux with an increase in surface superheat.

3.3. Typical Boiling Heat Transfer in FC-72

3.3.1. Transient CHF for Period τ under Saturated Condition. Figure 11 shows transient CHF, q_{cr} , for $Q_0 \exp(t/\tau)$ with the periods, τ , ranging from around 30 s down to 0.008 s under saturated FC-72 at atmospheric pressure depending on cylinder surface roughness. Two horizontal experimental heaters of 1.0 mm in diameter were used. One with no surface preparation and the other one is finished by emery paper. They have the different surface roughness of commercially available surface (CS, $R_a = 0.11 \mu\text{m}$) and roughly finished surface (RS, $R_a = 0.24 \mu\text{m}$), respectively.

In the case of CS cylinder, the q_{cr} values gradually increase to the maximum value from the steady state CHF, then quickly decrease to the minimum value, and finally increase again accompanied by a decrease in period τ . They are clearly classified into three groups for the period. First group is for the periods longer than 2 s, second group is for the periods shorter than 0.4 s, and third one is for the period between 2 and 0.4 s. In the case of RS cylinder, however, it can be found that there clearly exists an effect of surface roughness; the direct transitions belonging to the second group q_{cr} occur with remarkable frequency. It means that a range in periods for q_{cr} of the 2nd group is changed depending on the surface roughness.

The CHF belonging to the 1st group with a longer period occurs with a fully-developed nucleate boiling (FDNB) heat transfer process. The steady-state CHF were due to HI. For the 2nd group with shorter periods, the direct transition

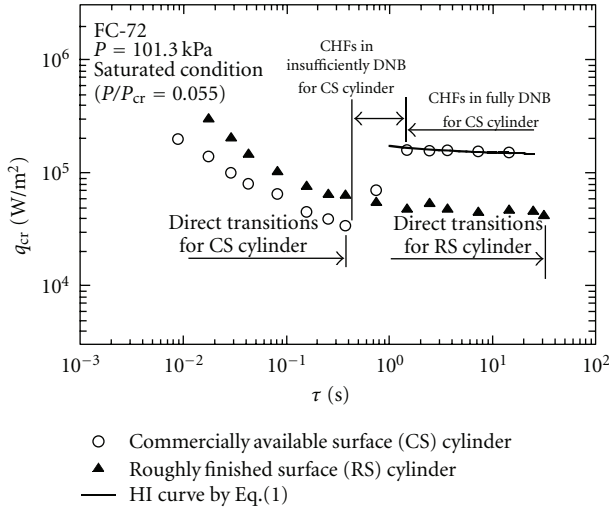


FIGURE 11: The relation between q_{cr} and τ at atmospheric pressure in saturated FC-72 depending on cylinder surface roughness.

to film boiling from non-boiling occurs as an explosive boiling. Fukuda et al. [15] suggested the empirical equation representing transient CHF values versus periods belonging to the first group in a pool of water. One has

$$q_{cr} = q_{st,sub}(1 + 0.21\tau^{-0.5}), \quad (1)$$

where the $q_{st,sub}$ is given by the quasi-steady-state CHF data in each experiment. Equation (1) is effective for not only water but also the highly wetting liquid such as FC-72 as shown in the figure.

3.3.2. Heat Transfer Processes up to CHF. Heat transfer processes during transitions to fully-developed nucleate boiling or to film boiling at atmospheric pressure in saturated FC-72 are shown in Figure 12.

In the case of the CS cylinder of roughness, they show the heat transfer processes to film boiling that are completely different from each other due to the exponential period. For the period of 0.02 s, the processes up to initial boiling heat fluxes, q_{in} , are the heat conduction regime derived by Sakurai and Shiotsu [12]. It is considered that the direct boiling transition from non-boiling to film boiling is due to the heterogeneous spontaneous nucleation (HSN) as mentioned before. For the period of 10 s, however, after the incipience of boiling, the nucleate boiling occurs from the residual inert gases which are included into the cavities that are formed after detachment of vapor bubbles with a slight decrease in surface superheat which prevents the growth of the HSN.

On the other hand, in the case of the RS cylinder of roughness for the period of 10 s as shown with a dashed line, the heat transfer processes up to, q_{in} , show that heat flux, q , increases along the natural convection curve derived by Takeuchi et al. [11] in the same process as the CS cylinder. The CHF point is due to the direct transition from single-phase conduction regime to film boiling; the value q_{in} is equal to q_{cr} . This boiling curve is similar in transition process to the boiling curve for the period of 0.02 s on CS cylinder.

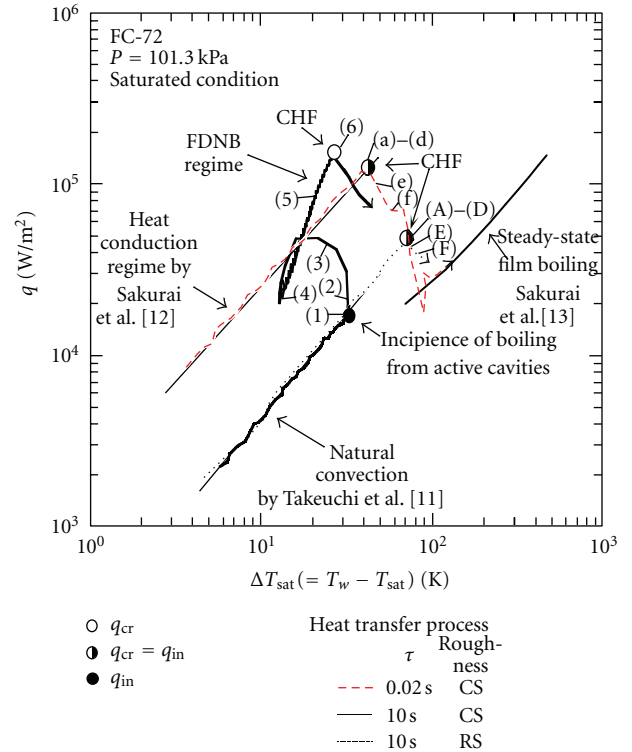


FIGURE 12: Boiling heat transfer processes from non-boiling to film boiling or FDNB at atmospheric pressure in saturated FC-72. Photographs are shown in Figures 13–15.

The boiling occurs at a surface superheat point of 70 K which is the highest temperature in this experimental scope. It is considered that the direct boiling transitions occur due to the levitation of liquid on the cylinder surface by the explosive-like HSN in originally flooded cavities without contribution of the active cavities entraining vapors. The direct transition is particularly likely to occur in the RS cylinder of roughness.

3.3.3. Photograph Studies in Vapor Behavior. Figure 13 shows the photographs of transient boiling behavior taken by a high-speed video camera at the corresponding points shown in Figure 12. The vapor bubbles are rapidly growing and surrounding the cylinder surface. The rapid growth of vapor bubbles is due to heterogeneous spontaneous nucleation (HSN) within the flooded cavities of cylinder. As shown in the figure, the vapor bubbles covered almost all the heater surface within just a few millisecond. It is seen that the vapor bubbles are separated from the cylinder surface. Figure 13(e) is the photograph of the time at which 15 ms elapsed from point (a). The film boiling appears after the departure of vapor bubbles. Figure 13(f) is the photograph after the time passage of 42 ms from point (a) and is the stable film boiling after passing the point (e).

Figure 14 shows the photographs for typical vapor film and vapor bubble behaviors in the transition to developed nucleate boiling corresponding points shown in Figure 12. The large vapor bubbles are rapidly growing and surrounding the cylinder surface, and the cylinder is almost fully

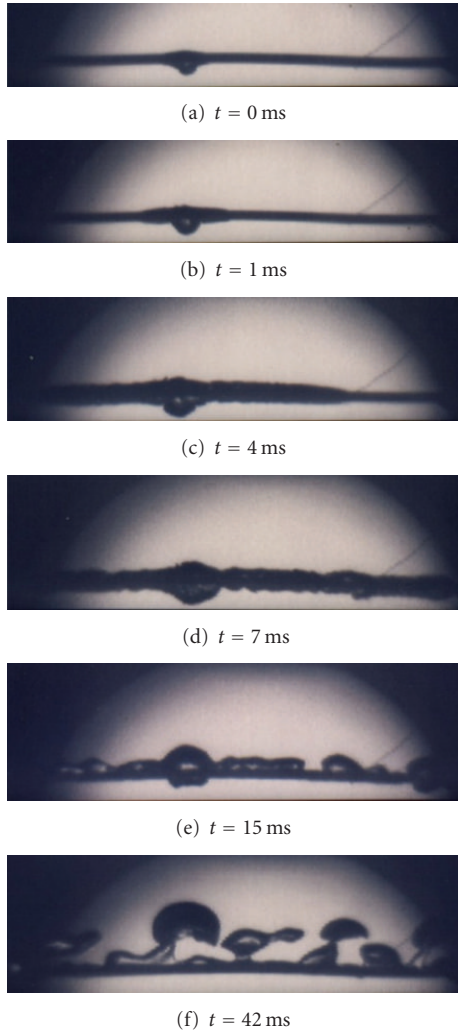


FIGURE 13: Vapor film behavior during direct transition to film boiling for a period of 0.02 s at atmospheric pressure in saturated FC-72 with the CS cylinder.

covered with the vapor bubbles as shown in the Figure 14(b). This vapor film behavior that is rapidly growing and covering the heater surface during boiling initiation could never be seen in the water experiment with quasi-steadily increasing exponential heat input. As seen in Figure 14(c), the nucleate boiling occurs from the cavities of entrained vapor that are formed after detachment of vapor bubbles with a slight decrease in surface superheat which prevents the growth of the HSN. If the detachment of vapor bubbles without decreasing in average surface superheat is realized, the direct or semi-direct transition occurs as in the case of rapidly increasing in heat input mentioned before.

Figure 15 gives a series of subsequent photographs from the moment of onset of a vapor phase to film boiling in experimental condition with RS cylinder. It is caused by slowly increasing heat input with a period of 10 s, and the corresponding heat transfer processes were shown in Figure 12. Figure 15(a) shows the boiling incipience just after natural convection regime. The vapor film behavior shown in

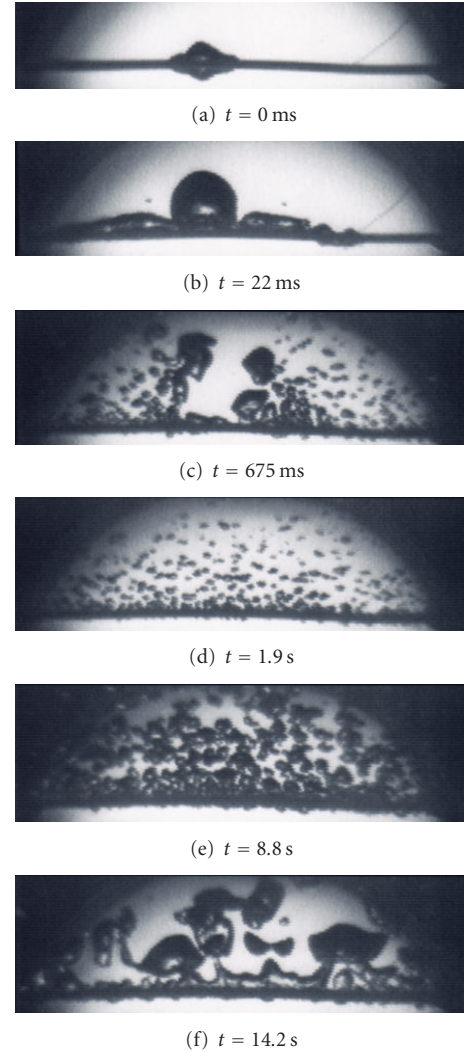


FIGURE 14: Vapor film behavior during transition to FDNB for a period of 10 s at atmospheric pressure in saturated FC-72 with the CS cylinder.

Figures 15(a) to 15(c) is similar to that of the direct transition of CS cylinder for a period of 0.02 s in Figure 13. Then a larger vapor tube is rapidly formed around cylinder, the vapor bubbles collapse as shown in Figure 15(d), and they break away from the cylinder surface. After the detachment of the large vapor bubbles, the vapor bubbles are separated from the vapor film with the most dangerous Taylor wave length as shown in Figure 15(f).

4. Conclusions

The vapor behavior on the horizontal cylinder during the transition from natural convection and transient conduction regimes to film boiling in water and highly wetting liquids such as ethanol and FC-72 due to various exponentially increasing heat inputs including a quasi-steadily increasing heat input to a rapid increasing one was examined by the photographs taken using a high-speed video camera.

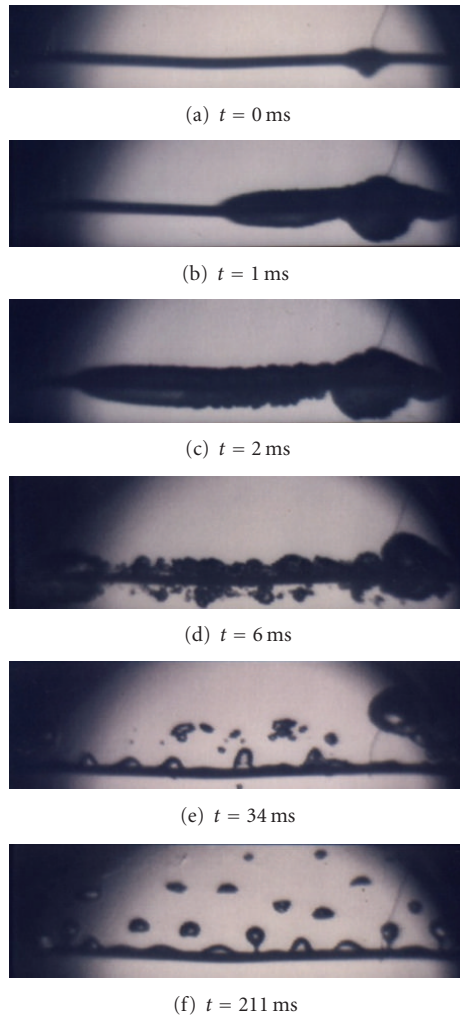


FIGURE 15: Vapor film behavior during direct transition to film boiling for a period of 10 s at atmospheric pressure in saturated FC-72 with the RS cylinder.

In the case of the highly wetting liquids, the vapor film behavior during transition to fully developed nucleate boiling was just similar to that of the direct transition to film boiling. This vapor film behavior that was rapidly growing and covering the heater surface during initial boiling could never be seen in the water experiment with a quasi-steadily increasing exponential heat input. It was confirmed that the initial boiling behavior is significantly affected by the property and the wettability of the liquid. The direct transition at the CHF from non-boiling regime to film boiling one occurred without a heat flux increase for a short period within the second group while semi-direct transition occurred with one. It was certain that the direct or semi-direct transition occurs in the case of rapidly increasing heat input when the detachment of vapor bubbles without decreasing of average surface superheat is realized. The transient CHF's are clearly divided into three principal groups for the periods.

References

- [1] S. S. Kutateladze, "Heat transfer in condensation and boiling," Tech. Rep. AEC-tr-3770, USAEC, Houston, Tex, USA, 1959.
- [2] N. Zuber, "Hydrodynamic Aspects of Boiling Heat Transfer," Tech. Rep. AECU-4439, USAEC, Houston, Tex, USA, 1959.
- [3] B. P. Avksentyuk and N. N. Mamontova, "Characteristics of heat transfer crisis during boiling of alkali metals and organic fluids under free convection conditions at reduced pressure," in *Proceedings of the Heat and Mass Transfer Program*, vol. 7, pp. 355–362.
- [4] S. S. Kutateladze, V. N. Moskvicheva, G. I. Bobrovich, N. N. Mamontova, and B. P. Avksentyuk, "Some peculiarities of heat transfer crisis in alkali metals boiling under free convection," *International Journal of Heat and Mass Transfer*, vol. 16, no. 4, pp. 705–IN1, 1973.
- [5] A. Sakurai and A. Shiotsu, "Heat transfer from a horizontal wire in liquid nitrogen," in *Heat Transfer and Super-conduction Magnetic Energy Storage*, vol. 211, pp. 7–18, ASME HTD, New York, NY, USA, 1992.
- [6] A. Sakurai, M. Shiotsu, and K. Hata, "New transition phenomena to film boiling due to increasing heat inputs on a solid surface in pressurized liquids," in *Proceedings of the ASME Winter Annual Meeting, Instability in Two Phase Flow Systems*, vol. HTD-260/Fed-169, pp. 27–39, ASME, New York, NY, USA, December 1993.
- [7] A. Sakurai, M. Shiotsu, K. Hata, and K. Fukuda, "Photographic study on transitions from non-boiling and nucleate boiling regime to film boiling due to increasing heat inputs in liquid nitrogen and water," *Nuclear Engineering and Design*, vol. 200, no. 1, pp. 39–54, 2000.
- [8] J. Y. Chang, S. M. You, and A. Haji-Sheikh, "Film boiling incipience at the departure from natural convection on flat, smooth surfaces," *Journal of Heat Transfer*, vol. 120, no. 2, pp. 402–409, 1998.
- [9] K. Fukuda, Q. S. Liu, J. D. Park, and H. Kida, "Photographic study on transient critical heat flux depending on surface conditions of test heater in various liquids due to exponentially increasing heat inputs," in *Proceedings of 6th International Symposium on Heat Transfer*, pp. 511–518, Beijing, China, 2004.
- [10] J. Park, "Photographic study of transient phenomena in pool boiling CHF for various liquids," in *Proceedings of 7th International Symposium on Marine Engineering*, Tokyo, Japan, October 2005.
- [11] Y. Takeuchi, K. Hata, M. Shiotsu, and A. Sakurai, "General correlation for laminar natural convection heat transfer from single horizontal cylinders in liquids and gases with all possible Prandtl numbers," in *Proceedings of the ASME International Mechanical Congress and Exposition*, vol. HTD-317-1, pp. 259–270, ASME, New York, NY, USA, November 1995.
- [12] A. Sakurai and M. Shiotsu, "Transient pool boiling heat transfer, Part 1: incipient boiling superheat," *ASME Journal of Heat Transfer*, vol. 99, no. 4, pp. 547–553, 1977.
- [13] A. Sakurai, M. Shiotsu, and K. Hata, "General correlation for pool film boiling heat transfer from a horizontal cylinder to subcooled liquid. Part 2. Experimental data for various liquids and its correlation," *Journal of Heat Transfer*, vol. 112, no. 2, pp. 441–450, 1990.
- [14] A. Sakurai, M. Shiotsu, K. Hata, and K. Fukuda, "Transition phenomena from non-boiling regime to film boiling on a cylinder surface in highly subcooled and pressurized water due to increasing heat inputs," ASME Paper 95-WA/HT-17, 1995.

- [15] K. Fukuda, M. Shiotsu, and A. Sakurai, "Transient pool boiling heat transfer due to increasing heat inputs in subcooled water at high pressures," in *Proceedings of the 7th International Meeting on Nuclear Reactor Thermal Hydraulics*, pp. 554–573, Saratoga Springs, NY, USA, 1995.

Research Article

Aqueous Nanofluid as a Two-Phase Coolant for PWR

Pavel N. Alekseev, Yury M. Semchenkov, and Alexander L. Shimkevich

NRC “Kurchatov Institute”, 1 Kurchatov Square, Moscow 123182, Russia

Correspondence should be addressed to Alexander L. Shimkevich, shall@dhtp.kiae.ru

Received 19 May 2012; Revised 28 August 2012; Accepted 11 September 2012

Academic Editor: Boštjan Končar

Copyright © 2012 Pavel N. Alekseev et al. This is an open access article distributed under the Creative Commons Attribution License, which permits unrestricted use, distribution, and reproduction in any medium, provided the original work is properly cited.

Density fluctuations in liquid water consist of two topological kinds of instant molecular clusters. The dense ones have helical hydrogen bonds and the nondense ones are tetrahedral clusters with ice-like hydrogen bonds of water molecules. Helical ordering of protons in the dense water clusters can participate in coherent vibrations. The ramified interface of such incompatible structural elements induces clustering impurities in any aqueous solution. These additives can enhance a heat transfer of water as a two-phase coolant for PWR due to natural forming of nanoparticles with a thermal conductivity higher than water. The aqueous nanofluid as a new condensed matter has a great potential for cooling applications. It is a mixture of liquid water and dispersed phase of extremely fine quasi-solid particles usually less than 50 nm in size with the high thermal conductivity. An alternative approach is the formation of gaseous (oxygen or hydrogen) nanoparticles in density fluctuations of water. It is possible to obtain stable nanobubbles that can considerably exceed the molecular solubility of oxygen (hydrogen) in water. Such a nanofluid can convert the liquid water in the nonstoichiometric state and change its reduction-oxidation (RedOx) potential similarly to adding oxidants (or antioxidants) for applying 2D water chemistry to aqueous coolant.

1. Introduction

It is well known [1] that the microstructure of liquid water is not understood, and its dynamic hydrogen-bonds (HB) structure has been the subject of intense debate for decades. Ice, whose HB structure was long ago well established, forms a tight “tetrahedral” lattice of molecules each binding to four others. The prevailing model of liquid water holds that as ice melts, the molecules loosen their grip but remain generally arranged in the same tetrahedral groups. This hydrogen-bonding pattern has been assumed to account for water properties.

However the majority of molecules were found in higher density regions with an asymmetric disordered structure where some islands of tetrahedral order were floated [2]. The greater density of liquid water in these regions implies that the molecules are more closely packed there than the simple tetrahedrons seen in ice [3, 4].

The conclusion [2, 5] that a dominant fraction of the molecules in liquid water are very asymmetrically hydrogen bonded with only two well-defined H-bonds (one donating

and one accepting) is in strong contrast to the accepted picture as being near tetrahedral, H bonded. From small-angle X-ray scattering studies, they furthermore find evidence for density nonhomogeneity on a length-scale of 1 nm indicating that the two components are spatially separated on the time scale of the experiment. The recent controversy about the structure of liquid water pits new models involving water molecules in relatively stable rings-and-chains structures against the standard model that posits water molecules in slightly distorted tetrahedral coordination. The current study is giving new life to familiar Rontgen’s “two-structure” model of liquid water [3, 4].

A topological structure of density fluctuations in condensed matter has been studied by molecular-dynamics (MD) simulation as ramified clusters of almost regular Delaunay’s simplexes (tetrahedrons) built on the fours of densely packed atoms and connected in pairs by faces as tetrahedral Bernal’s chains [6, 7]. The review of publications on this subject is presented in the monograph [8] and a topological criterion [9–11] is offered for finding these simplexes exactly. Such a criterion allows making the selection of

the dense-part simplexes by fixing the overall length of their edges in a point of maximum number of obtained clusters in the MD cell.

At the same time, any nanofluid as a new coolant is a suspension of nanoparticles with sizes less than 100 nm and volume fractions typically less than 4% [12]. Such a coolant has shown the ability of enhancement (up to 40%) in thermal conductivity compared with the base liquid [13] and a significant increase of critical heat flux [14]. Oxides (Al_2O_3 , CuO , TiO_2), nitrides (AlN , SiN), carbides (SiC , TiC), and metals (Ag , Au , Cu , Fe) can be used in the nanofluid as nanoparticle materials [15].

Presently, nanofluids are produced by two techniques [15]. A two-step technique starts with nanoparticles produced by one of physical or chemical synthesis techniques as a dry powder and then dispersed into the base liquid. This method may result in a large degree of nanoparticle agglomeration. The single-step (evaporation) one simultaneously makes and disperses the nanoparticles directly into the base liquid. The two-step process produces nanofluids with oxide nanoparticles and the single-step one produces the nanofluids with metal nanoparticles.

They are unlikely to become the mainstay of commercial nanofluid production due to the required low vapour pressure (typically less than 10 Pa) that limits the rate of nanofluid production and makes it expensive. Although nanoparticle agglomeration in this case is minimized as a result of the liquid flowing continuously, the effect of temperature and operation conditions on allocation of nanoparticles may be significant due to changing the electric potential on the surface of colloidal particles as a main factor to provide the stability of nanofluid [16].

Therefore systematic studying of the aqueous nanofluids is needed [17–20] since a key factor in understanding their thermal properties is the clustering effects that provide paths for rapid heat transport and stabilize nanofluid composition in different conditions.

2. Some Aspects of Liquid Water Microstructure

Precise experimental techniques for determining the local structure of liquid water are missing since each water molecule undergoes rapid rearrangement on the order of femtoseconds. The need for a better understanding of water at the microscopic level has forced the development of computational methods that describe the individual and cooperative structure and dynamics of water molecules, and many studies have been carried out using these techniques. These simulations predict locally ordered hydrogen-bonding clusters of water molecules that continually form and break [21].

MD simulations of density fluctuations in liquid metals [9, 10] have shown that their dense tetrahedral clusters are characterized by vertex connections as well as in liquid water the low-density ice crystallites are divided by dense tetrahedral clusters with an asymmetrical structure [1]. However these clusters (see Figure 1(a)) are more complicated due to the effect of hydrogen bonds but the frame of them as a

broken red line connecting the centers of tetrahedrons is also ramified [20].

One can expect that water molecules have enough time for rebuilding hydrogen bonds in a dense part of water density fluctuations due to very fast librations and rotations of them in liquid phase. From this, the model for instant dense clusters [22] is built with helices of hydrogen bonds (see Figure 1(b)). All angles between them are equal to 106.8° . Each water molecule in such clusters is tetrahedrally bonded with three molecules of the same cluster and with one of some ice crystallites in liquid water.

The topology of helical clusters is essentially differed from the one of the crystalline ice. From this and only this point of view, the liquid water is considered as a two-structural fluid by dynamic forming the two topological kinds of clusters in density fluctuations. The mole fraction of helical clusters in liquid water can amount to 0.6 [22].

The dense helical clusters save, in principle, four hydrogen bonds for each molecule of water; three of them are internal and one is external for connecting to ice crystallites. They can stimulate coherent proton vibrations in the coil of helical cluster if these protons are ordered in the helix (see Figure 1(b)). A spectral series, $\nu(n)$, of coherent proton vibrations in the helical cluster as a function of water-molecules number, n , is [22]

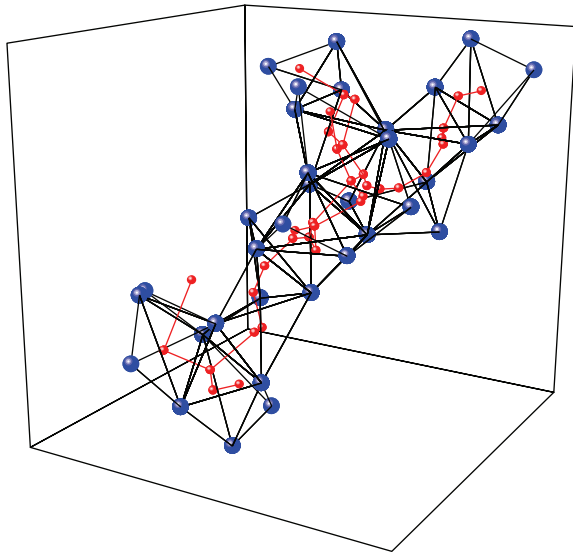
$$\nu[\text{THz}] \sim 22 \frac{\sqrt{n-1}}{n}, \quad \text{at } n \geq 6. \quad (1)$$

A possible generation of coherent proton vibrations by an external electromagnetic impact at these resonance frequencies can selectively amplify each mode and, thus, can strengthen water microheterogeneity far from its thermodynamic equilibrium. Therefore studying the electromagnetic absorption at these frequencies can be interesting both for revealing spectral lines (1), and for creating a possible technique for managing the microstructure of water. Moreover, additives in aqueous solution can be concentrated in the ramified interface of two dynamic microstructures of liquid water that can cause fluctuation-induced clustering of the impurities in nanoparticles and thus, forming a stable two-phase state of aqueous solution [20, 23].

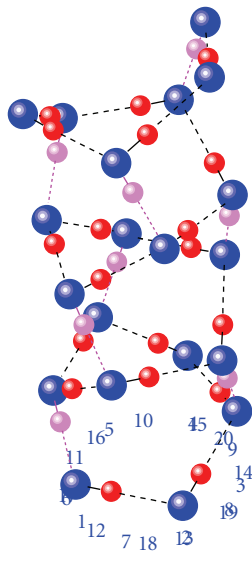
3. Clustering Impurities in Liquid Water

A spatial position of any impurity in liquid solution has dual character due to density fluctuations of the solvent that build instant dense clusters of almost regular tetrahedrons connected in pairs by faces in ramified n -chains from solvent atoms [6, 11]. At a low concentration of impurity, its atoms place on the external faces of the dense solvent clusters. In increasing concentration, the impurity atoms build their own dense tetrahedral clusters in the solution so that it becomes microheterogeneous as a nanofluid [23].

In liquid water, tetrahedral clusters of water density fluctuations (see Figure 1(b)) are more complicated than the ones in simple liquids due to hydrogen bonds but the frame of them as a broken red line (see Figure 1(a)) connecting the centres of tetrahedrons is also ramified [19].



(a)



(b)

FIGURE 1: (a) A dense tetrahedral cluster in MD model of liquid water at 300 K and its frame (broken red line); blue points are the molecules and red points are centres of the cluster tetrahedrons; (b) the helical atomic model for this cluster with possible coherent exchange of protons (red balls) between oxygen atoms (blue balls) along the helix of hydrogen bonds (black lines) and hydrogen-bond bridges (pink balls); the projections of oxygen atoms in the plane are denoted by numbers.

Thus, the impurities residence in liquid water is practised in the interface of low- and high-density regions. At some concentration of impurity atoms, they form their own dense tetrahedral clusters in the aqueous solution. Such clusters (“inherent” nanoparticles) will be stable at different conditions of the water-coolant operation [20].

In this connection, it is offered a fractal model for inherent nanoparticles that can appear in the water coolant under some conditions as percolation clusters of solid-like

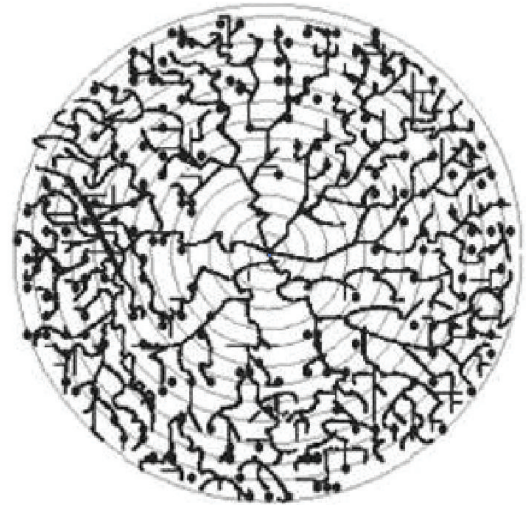


FIGURE 2: The scheme of percolation fractal cluster of solid-like filaments.

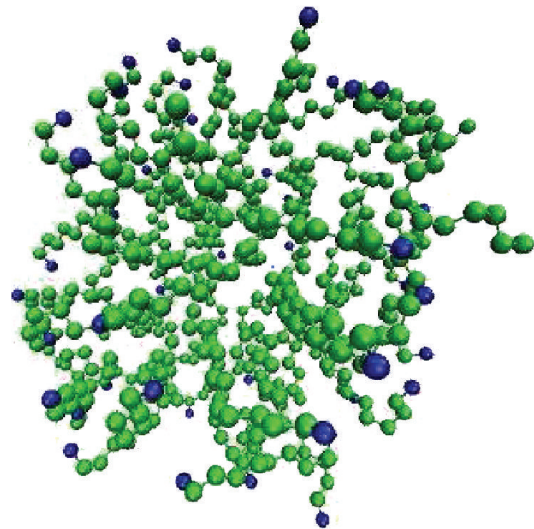


FIGURE 3: The fractal cluster as an inherent micelle in liquid water.

filaments [19] shown in Figure 2. Such a fractal nanoparticle is a micelle presented in Figure 3.

In [24], it is shown that fractal matter, M , enclosed in a sphere of radius, r , satisfies the scaling law

$$M(r) \sim r^D, \tag{2}$$

where D is Hausdorff’s dimension of particle fractal which is equal to ~ 2.5 .

In any real cluster, the fractal structure observed on scales, r , satisfied the condition of $a < r < d/2$, where d is the size of fractal nanoparticle and a is the thickness of fractal filament. In that case, one can easily obtain the volume fraction, φ_f , of particle material in the fractal as [19]

$$\varphi_f = (3/D)(2a/d)^{3-D}. \tag{3}$$

4. Evaluating Heat Transfer in Liquid Water by Fractal Nanoparticles

Thermal properties of fiber constituents (filaments) are locally anisotropic but the same properties of a clew of filaments are isotropic [19]. Therefore the thermal conductivity, λ_f , of fractal matter as a percolation cluster filled with liquid is the same as the solid nanoparticle with respect to heat flow in the fluid and presented as $\lambda_f \equiv \lambda_m$. Here λ_m is the thermal conductivity of dispersed material.

At the same time, spherical fractal particles have developed interface of the solid/liquid contact (see Figure 2) and its heat-variable resistor is negligible. Then, we can use the potential theory of Maxwell [25] for well-dispersed fractal nanoparticles that gives a simple relationship for the thermal conductivity, λ_n , of nanofluid (with randomly distributed and noninteracting spherical particles) in the reduced form

$$\frac{\lambda_n}{\lambda} \approx 1 + 3\varphi_p \frac{(1-\alpha)}{(1+2\alpha)}, \quad (4)$$

where λ is the thermal conductivity of liquid matrix, φ_p is the volume fraction of nanoparticles in liquid, and $\varphi \equiv \varphi_f \varphi_p$ is the volume fraction of their material in the liquid; $\alpha = \lambda/\lambda_m \ll 1$. Since $\varphi_p \equiv \varphi/\varphi_f = (D/3)(2a/d)^{D-3} \varphi$ in [19], the following equation is obtained:

$$\frac{((\lambda_n/\lambda) - 1)}{\varphi} \approx D \left(\frac{2a}{d} \right)^D - \frac{3(1-\alpha)}{1+2\alpha}. \quad (5)$$

The function (5) of three parameters: D , $2a/d$, and α is calculated for estimating the effect of fractal structure of nanoparticles on the thermal conductivity of aqueous nanofluid that is given in Table 1.

5. Discussion of Results

According to [20, 23], the lower limit of the impurity concentration for its clustering in liquid water is $0.1 C_s$, where C_s is the saturation impurity concentration. It is clear that this range for clustering impurities dissolved in water as “solid-like” nanoparticles is an effective way to stabilize the aqueous nanofluid structure for different conditions (high temperature, flow rate, radiation, etc) of its operation in any power system. In the limit of a small volume fraction of such nanoparticles and their high thermal conductivity, the enhancement of thermal conductivity of aqueous nanofluid can be 18φ for spherical fractal particles of 10–50 nm in size composed of fine filaments of 0.5–1.0 nm in diameter. The significant property of considered fractal structure of disperse phase in nanofluids is an explanation of observed enhancement of their kinetic characteristics obtained in different experiments.

At the same time, it is important to understand that the fractal particles are the product of complex chemical reactions between any dissolved impurity and the aqueous solvent. Therefore, it is necessary to develop a special technology for getting them and stabilizing them in liquid matter.

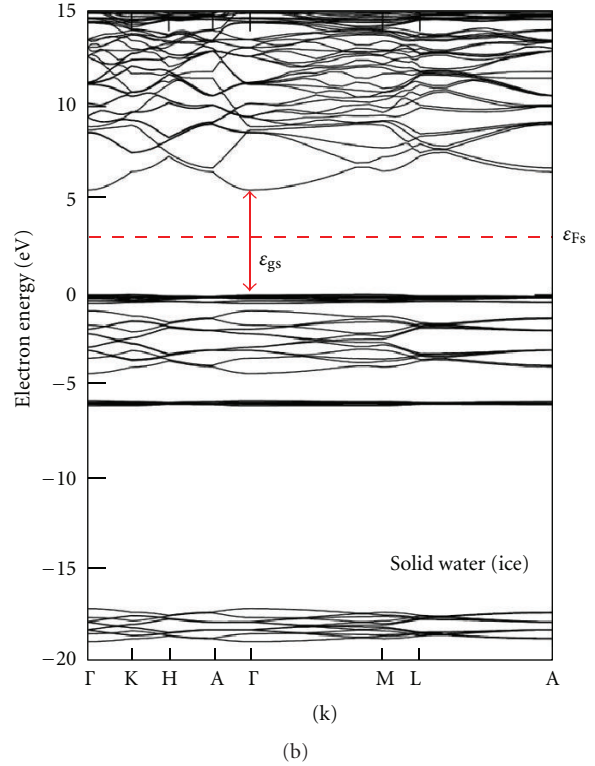
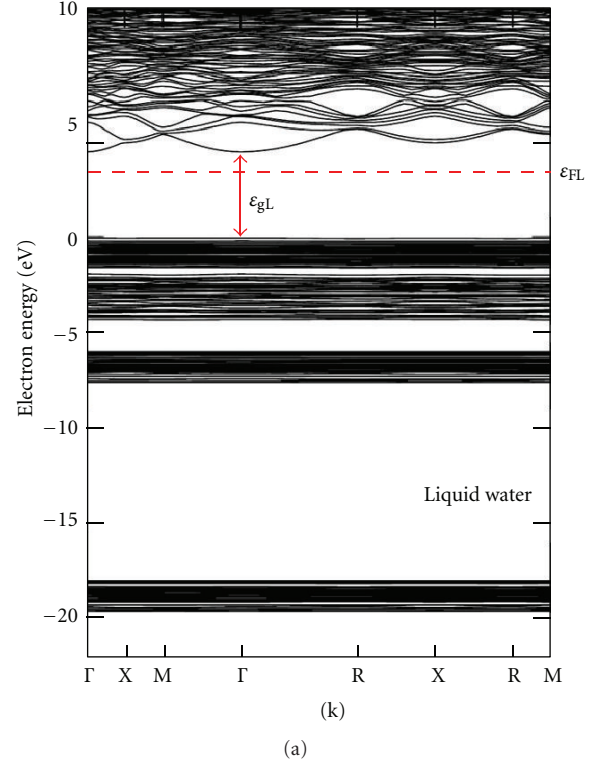


FIGURE 4: Brillouin bands of liquid (a) and solid (b) water [26]; here the zero energy of electrons corresponds to the top of valence band and red dotted lines are Fermi levels, ϵ_{FL} and ϵ_{FS} , of electrons in liquid and solid water with corresponding band gaps, ϵ_{gL} and ϵ_{gs} .

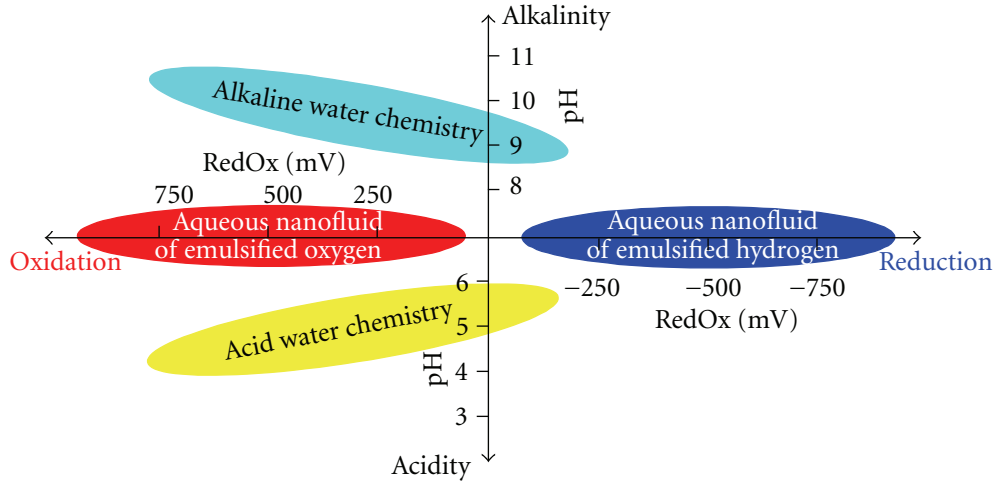


FIGURE 5: Diagram of aqueous chemistry as 2D plot of pH and RedOx parameters.

TABLE 1: The enhancement of water thermal conductivity by fractal nanoparticles.

	Al ₂ O ₃			Al			Cu			Carbon fiber		
<i>D</i>	3.0	2.7	2.5	3.0	2.7	2.5	3.0	2.7	2.5	3.0	2.7	2.5
<i>2a/d</i>	—	0.02	0.1	—	0.02	0.1	—	0.02	0.1	—	0.02	0.1
<i>α</i>	0.02	0.02	0.02	0.002	0.002	0.002	0.001	0.001	0.001	0	0	0
$(\lambda_0/(\lambda - 1))/\varphi$	2.87	8.35	7.56	2.98	8.68	7.86	2.99	5.37	17.6	3.0	8.73	17.7

The theoretical studies [11] show that the fluctuation-induced clustering of impurities is possible only if the solid-like disperse phase (colloids) in aqueous solution is hydroxides. Therefore, it is necessary to select correctly impurities for water solution in order to get the stable nanosuspension in it [20].

In this connection, a nanofluid with gaseous nanoparticles (bubble stones) is interested especially with oxygen (hydrogen) nanobubbles. These gaseous nanoparticles are gathered in fluctuation-induced defects of tetrahedral water structure mentioned above. Obviously, such formation of gaseous nanoemulsion in aqueous solution allows obtaining comparatively stable nanobubbles that can considerably exceed the molecular solubility of gaseous impurities in liquid water at the given temperature.

Moreover, the aqueous nanofluid of emulsified oxygen (hydrogen) converts the liquid water in the nonstoichiometric state that is illustrated in Figure 4(a) by a shift of Fermi level, ε_{FI} , in the band gap, ε_{gl} , of liquid water. Here is the hypostoichiometric state of water by emulsifying hydrogen in it. As seen in Figure 4(b), Fermi level, ε_{Fs} , of solid water is in the middle of band gap, ε_{gs} , that is corresponded to the stoichiometric state of ice as a characteristic electron state of solid water.

It is known [27] that the change of Fermi level in the band-gap of any nonmetal liquid is equivalent to changing a Reduction-Oxidation (RedOx) potential of this melt. This can concern the aqueous nanofluid with emulsified oxygen (hydrogen) as it is shown in Figure 5 in the plane of two coordinates, pH and RedOx [28]. The first parameter defines the logarithmic portion of hydrogen cations in liquid water,

that is, alkalinity or acidity of the aqueous matter, and the second one reflects nonstoichiometric state, $H_2O_{1\pm x}$, of liquid water as the condensed matter, that is, the presence in it of dissolved hydrogen or oxygen.

It is visible that the aqueous chemistry accepted in power engineering of pressure-water reactor (PWR) is the oxidative one due to continuous additives of feed water that naturally dissolves oxygen in it. This impurity is not desirable for the aqueous chemistry of the PWR first-loop coolant due to strong oxidizing structural materials providing continuous growth of oxide films on the surface of fuel cladding.

At the same time, the PWR operation experience shows that this film of thickness more than 10–15 microns is fragile and sensitive to thermal cycles. The film is locally breaking and opens the fuel cladding to corrosion by zirconium-steam reaction.

Therefore, it is important to organize an effective technological process for removing oxygen from the feed water. In hydrogen “rinsing” of this water, it is possible to convert RedOx potential of the aqueous coolant in the negative value area (see Figure 5) and obtain the corrosion-passive one that can inhibit the growth of oxide films on the surface of fuel cladding and local breakup of them.

6. Conclusions

The theoretical studies show how one can provide the stable formation of nanoparticles in water solution. It is important to form clusters in water directly from impurities that are dissolved there. Then, ramified fractal clusters, as natural

solid-like part of solution, can be stable constituents of the aqueous nanofluid.

It will provide the stability of water nanofluid embedded with such nanoparticles that flow in the first loop of PWR without changing their microstructure.

Acknowledgments

The authors are pleased to acknowledge Dr. A. S. Kolokol for giving some data on molecular-dynamic simulation of water structure and discussing this work that is supported by the Russian Foundation of Basic Researches (Grant no. 10-08-00217).

References

- [1] C. Huang, K. T. Wikfeldt, T. Tokushima et al., "The inhomogeneous structure of water at ambient conditions," *Proceedings of the National Academy of Sciences of the United States of America*, vol. 106, no. 36, pp. 15214–15218, 2009.
- [2] P. Wernet, D. Nordlund, U. Bergmann et al., "The structure of the first coordination shell in liquid water," *Science*, vol. 304, no. 5673, pp. 995–999, 2004.
- [3] E. Cartledge, *The Strangest Liquid*, New Scientist, 2010.
- [4] K. Tuttle, *Researchers Rediscover the Structure of Water*, SLAC Today, 2010.
- [5] T. Tokushima, Y. Harada, O. Takahashi et al., "High resolution X-ray emission spectroscopy of liquid water: the observation of two structural motifs," *Chemical Physics Letters*, vol. 460, no. 4–6, pp. 387–400, 2008.
- [6] J. D. Bernal, "The structure of liquids," *Proceedings of the Royal Society A*, vol. 280, p. 299, 1964.
- [7] Y. Waseda, *The Structure of Non-Crystalline Materials, Liquids and Amorphous Solids*, McGraw-Hill, New York, NY, USA, 1980.
- [8] N. N. Medvedev, *Voronoy—Delaunay Method in Research of Structure of Non-Crystalline Systems Novosibirsk*, Siberian Branch of the Russian Academy of Science, 2000.
- [9] A. S. Kolokol and A. L. Shimkevich, "Topological structure of liquid metals," *Atomic Energy*, vol. 98, no. 3, pp. 187–190, 2005.
- [10] A. L. Shimkevich, A. S. Kolokol, and I. Y. Shimkevich, "Two-structure model for simple metals," *Journal of Non-Crystalline Solids*, vol. 353, no. 32–40, pp. 3472–3474, 2007.
- [11] A. S. Kolokol and A. L. Shimkevich, "Topological structure of density fluctuations in condensed matter," *Journal of Non-Crystalline Solids*, vol. 356, no. 4–5, pp. 220–223, 2010.
- [12] S. Choi, "Enhancing thermal conductivity of fluids with nanoparticles," in *Development and Applications of Non-Newtonian Flows*, D. A. Siginer and H. P. Wang, Eds., p. 99, ASME, New York, NY, USA, 1995.
- [13] M. Bahrami et al., "Assessment of relevant physical phenomena controlling thermal performance of nanofluids," in *Proceedings of the ASME International Mechanical Engineering Congress and Expo (IMECE '06)*, Chicago, Ill, USA, November 2006.
- [14] S. M. You, J. H. Kim, and K. H. Kim, "Effect of nanoparticles on critical heat flux of water in pool boiling heat transfer," *Applied Physics Letters*, vol. 83, no. 16, pp. 3374–3376, 2003.
- [15] W. Yu et al., "Review and assessment of nanofluid technology for transportation and other applications," Report of Argonne National Laboratory ANL/ESD/07-9, 2007.
- [16] Nanofluid Datasheet, "Meliorum Technologies," 2008.
- [17] C. H. Lo and T. T. Tsung, "Low-temperature effect on the stability of CuO nanofluid," *Reviews on Advanced Materials Science*, vol. 10, no. 1, pp. 64–68, 2005.
- [18] P. Keblinski, S. R. Phillpot, S. U. S. Choi, and J. A. Eastman, "Mechanisms of heat flow in suspensions of nano-sized particles (nanofluids)," *International Journal of Heat and Mass Transfer*, vol. 45, no. 4, pp. 855–863, 2001.
- [19] A. L. Shimkevich, "On enhancing water heat transfer by nanofluids," in *Proceedings of the 17th International Conference on Nuclear Engineering (ICONE '09)*, pp. 19–22, July 2009.
- [20] P. N. Alekseev et al., "On basic principles for modifying water as a coolant of PWR," in *Proceedings of the Transactions of European Nuclear Conference (ENC '10)*, Barcelona, Spain, 2010.
- [21] R. Roy, W. A. Tiller, I. Bell, and M. R. Hoover, "The structure of liquid water; novel insights from materials research; potential relevance to homeopathy," *Materials Research Innovations*, vol. 9, no. 4, pp. 98–103, 2005.
- [22] A. L. Shimkevich and I. Y. Shimkevich, "On water density fluctuations with helices of hydrogen bonds," *Advances in Condensed Matter Physics*, vol. 2011, Article ID 871231, 5 pages, 2011.
- [23] A. L. Shimkevich, *The Composition Principles for Designing Nuclear-Reactor Materials*, Edited by N. N. Ponomarev-Stepnoi, Izdat, Moscow, Russia, 2008.
- [24] V. E. Tarasov, "Fractional hydrodynamic equations for fractal media," *Annals of Physics*, vol. 318, no. 2, pp. 286–307, 2005.
- [25] J. C. Maxwell, *A Treatise on Electricity and Magnetism*, Dover, New York, NY, USA, 3rd edition, 1954.
- [26] G. Galli, *Electronic Properties of Water*, University of California, <http://angstrom.ucdavis.edu/>.
- [27] P. N. Alekseev and A. L. Shimkevich, "On voltage-sensitive managing the redox-potential of MSR fuel composition," in *Proceedings of the 16th International Conference on Nuclear Engineering (ICONE '08)*, pp. 21–29, May 2008.
- [28] D. Langmuir, *Aqueous Environmental Chemistry*, Prentice Hall, New Jersey, NJ, USA, 1997.

Research Article

Depressurization of Vertical Pipe with Temperature Gradient Modeled with WAHA Code

Oriol Costa, Iztok Tiselj, and Leon Cizelj

Reactor Engineering Division, Jožef Stefan Institute, Jamova Cesta 39, 1000 Ljubljana, Slovenia

Correspondence should be addressed to Oriol Costa, oriol.costa@ijs.si

Received 14 June 2012; Accepted 27 August 2012

Academic Editor: Eckhard Krepper

Copyright © 2012 Oriol Costa et al. This is an open access article distributed under the Creative Commons Attribution License, which permits unrestricted use, distribution, and reproduction in any medium, provided the original work is properly cited.

The subcooled decompression under temperature gradient experiment performed by Takeda and Toda in 1979 has been reproduced using the in-house code WAHA version 3. The sudden blowdown of a pressurized water pipe under temperature gradient generates a travelling pressure wave that changes from decompression to compression, and vice versa, every time it reaches the two-phase region near the orifice break. The pressure wave amplitude and frequency are obtained at different locations of the pipe's length. The value of the wave period during the first 20 ms of the experiment seems to be correct but the pressure amplitude is overpredicted. The main three parameters that contribute to the pressure wave behavior are: the break orifice (critical flow model), the ambient pressure at the outlet, and the number of volumes used for the calculation. Recent studies using RELAP5 code have reproduced the early pressure wave (transient) of the same experiment reducing the discharge coefficient and the bubble diameter. In the present paper, the long-term pipe pressure, that is, 2 seconds after rupture, is used to estimate the break orifice that originates the pressure wave. The numerical stability of the WAHA code is clearly proven with the results using different Courant numbers.

1. Introduction

Propagation of pressure waves through the piping systems of nuclear power plants is of key interest in the field of reactor safety analyses. Pressure surges are important also in other fields of process engineering [1]. During the loss-of-coolant-accident in a water-cooled reactor, the subcooled decompression results in the propagation of a rarefaction wave through the reactor system and can even result in further structural damage and failure to maintain core geometry and core cooling [2].

One of the key experiments historically well known as a benchmark case for thermal hydraulics system code RELAP5 [3] was the one of Edwards and O'Brien [4]. They ruptured a horizontal pipe filled with water at pressures and temperatures characteristic for water-cooled reactors. Later, Takeda and Toda [5] experimentally observed the pressure behavior in a vertical pipe ruptured at the top end with a temperature gradient (higher temperature at the top end) and analyzed it with simple equilibrium and nonequilibrium wave propagation models. Takeda and Toda showed that for

a pipe with a temperature gradient, flashing in the hotter section results from the passing of a rarefaction wave with a large enough amplitude, whereas the colder section, with a lower vapor pressure, remains subcooled liquid. A large discontinuity in the sound speed arises between the two-phase and single-phase regions serving as a reflective surface. The data from Takeda and Toda has been compared with a RELAP5 simulation by Lafferty et al. [6].

The RELAP5 computer code, widely used in nuclear reactor transient analysis, is based on a two-fluid model consisting of the mass, momentum, and energy conservation equations for each phase solved using a semi-implicit finite-difference technique [3, 7]. In the present paper, computer code WAHA [8], developed for simulations of acoustic phenomena in piping systems, is used to simulate the experiment of Takeda and Toda. WAHA code uses a similar mathematical model as RELAP5, but it is based on a characteristic upwind finite difference scheme. This allows more accurate tracking of pressure waves with less numerical diffusion and modeling of the critical two-phase flow with the basic two-fluid model without any special models.

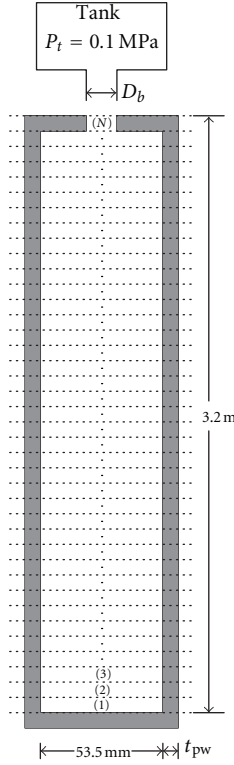


FIGURE 1: Sketch of the pipe section (D_b : break diameter, t_{pw} : pipe wall thickness).

The paper is divided in two main groups. Description of the experimental facility and introduction to the WAHA computer program are given in Section 2, and the results of the simulations are presented in Section 3 and 4. Section 3 starts with an explanation of the WAHA piping model and it is followed by a descriptive presentation of the simulations' results testing different numerical parameters. The influence of the parameters in the results gives an insight in the WAHA code numerical implementation. The influence of the Courant number, order of accuracy of the calculation and the number of volumes, used to divide the pipe's length, are tested initially. In Section 4 the sensitivity of different physical models is studied, first testing the pipe elasticity model and wall thickness influence, Section 4.1. Using the best of these parameters, the simulations are improved further studying the consequences of a smaller effective orifice diameter and higher values of the tank pressure in Sections 4.2 and 4.3 respectively. At the end, the conclusions are drawn.

2. Description of the Experiment and the Waha Code

The subcooled blowdown under temperature gradient experimental facility [5] comprised a test section of stainless steel pipe of 3.2 m length and 53.5 mm internal diameter. An orifice of 15 mm diameter was located at the top of the pipe resembling the pipe break and it was followed by

TABLE 1: Location of the pressure transducers (PT).

PT	Distance from bottom of the pipe (cm)
1	310.0
2	298.2
3	275.6
4	200.0
5	100.0
6	25.0

an exhaust tube minimizing back pressure effects after the orifice. The orifice was covered with 0.03~0.75 mm thick mylar paper. By rupturing the mylar paper, the sudden blowdown experiments started. The water filling the pipe section was heated by electrical heaters until the desired linear temperature distribution which was measured with thirteen temperature measuring terminals was attained. Five different experiments were performed with different temperature distributions. The temperature at the bottom of the pipe was fixed at room temperature (RT) for all five experiments. The temperatures at the top, close to the orifice, were RT, 95°C, 120°C, 140°C, and 160°C. Six different pressure transducers (PT) were mounted along the pipe length section to capture the fluid pressure changes. The positions of the transducers can be seen in Table 1. After heating up the water to the specific test temperature distribution, the pressure was set at 0.855 MPa at the position PT1 before the beginning of the experiments. Figure 1 shows a schematic view of the pipe.

The experiment with fluid temperature at the top of the pipe equal to 160°C has been modeled using the in-house code WAHA version 3 [8]. The WAHA computer program is a one-dimensional six-equation two-fluid solver developed for simulations of two-phase flow water hammer phenomena. The continuity, momentum and energy equations for liquid and gas phases are used in a nonconservative form. The continuity and energy equations are derived to account for the pipe elasticity and variable pipe cross-section effects. The pipe cross section ($A(x, t)$) can change due to variable geometry, which depends on the position, and the material elasticity, (1):

$$A(x, t) = A(x) + A_e(p(x, t)). \quad (1)$$

The pressure pulse ($p(x, t)$) produces a variation of the pipe diameter (D_p) following the linear relation [9]

$$\frac{dA_e}{A(x)} = \frac{D_p}{t_{pw}} \frac{dp}{E} = K dp, \quad (2)$$

where t_{pw} stands for the pipe wall thickness and E the modulus of elasticity of the material.

The WAHA code uses its own steam tables and contains correlations for mass, momentum, and heat transfer between phases and for wall friction. The correlations are flow regime dependent. The system of WAHA equations can be written in the form:

$$\mathbf{A} \frac{\partial \vec{\psi}}{\partial t} + \mathbf{B} \frac{\partial \vec{\psi}}{\partial x} = \vec{S}, \quad (3)$$

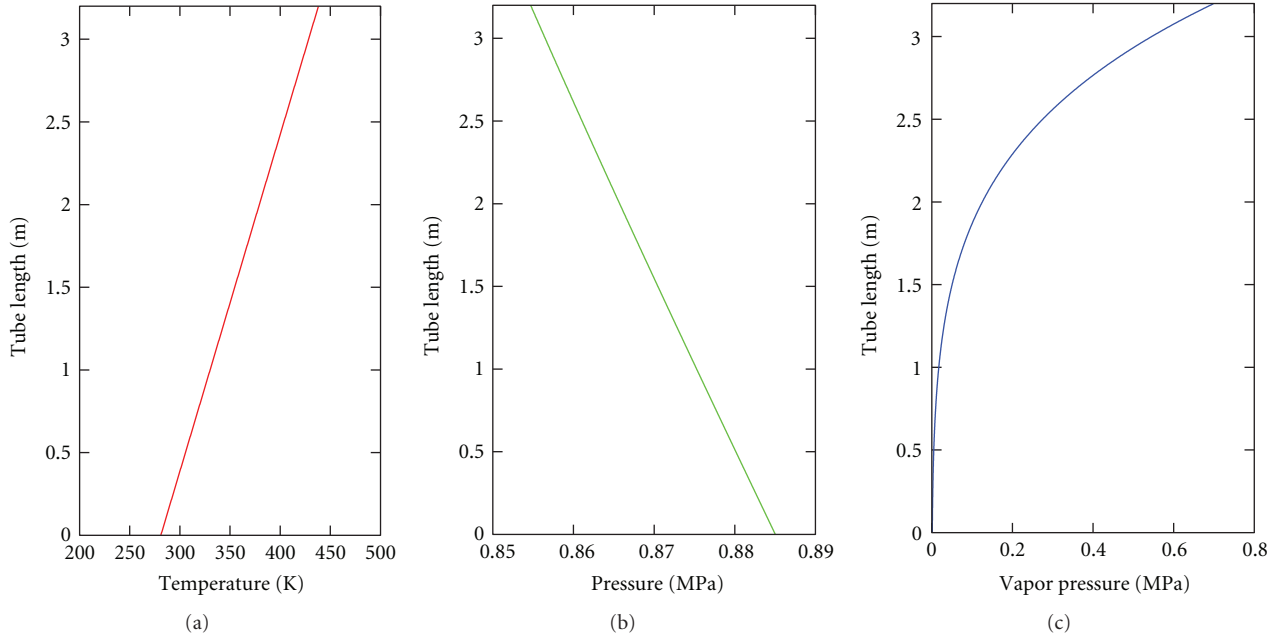


FIGURE 2: Initial conditions of the water.

where $\vec{\psi} = (p, \alpha, v_f, v_g, u_f, u_g)$ is the vector of independent variables (pressure, vapor volume fraction, velocities, and specific internal energy for the liquid and gas phases, resp.), \mathbf{A} and \mathbf{B} are the matrices of the system, and \vec{S} is a vector which contains the nondifferential terms in the equations. The numerical scheme of the WAHA computer program uses the splitting operator with implementation consisting of two steps explained below. First, the source term vector \vec{S} is split in two parts. The “non-relaxation” sources \vec{S}_{N-R} which contain the wall friction, volumetric forces, sources due to the variable pipe cross-section and sources due to the pipe motion (not implemented in version 3). The second part of the source term vector \vec{S} includes the relaxation sources \vec{S}_R that tend to establish thermal and mechanical equilibrium between liquid and vapor phases. The relaxation source terms \vec{S}_R are often stiff, meaning that their characteristic times are much shorter than other phenomena in two-phase flow. In the first step of the splitting operator method, the convection term with the nonrelaxation sources is treated with shock-capturing numerical scheme with low numerical diffusion:

$$\mathbf{A} \frac{\partial \vec{\psi}}{\partial t} + \mathbf{B} \frac{\partial \vec{\psi}}{\partial x} = \vec{S}_{N-R}. \quad (4)$$

In the second step, the system of ordinary differential equations—relaxation source terms—is solved with a variable time step:

$$\mathbf{A}_T \frac{\partial \vec{\psi}_T}{\partial t} = \vec{S}_R, \quad (5)$$

where $\vec{\psi}_T = (p, \alpha, v_f, v_g, T_f, T_g)$ now contains the temperature of both phases instead of the specific internal energy. Matrices \mathbf{A}_T , \mathbf{A} , and \mathbf{B} are fully developed in [8].

3. Waha Model—Sensitivity to Numerical Parameters

The experiment with water temperature at the top of the pipe equal to 160°C has been reproduced using the WAHA computer program.

3.1. Model and Initial Conditions. The WAHA code uses ASCII input data files that contain all geometrical, physical, computational and temporal characteristics of a modeled piping system. Figure 1 shows the two modeled components to simulate the experimental facility. The first component is the pipe which consists of N volumes dividing its length. The lower part of the pipe is a closed end ensuring fluid velocity equal to 0. The last volume (Figure 1) at the top of the pipe has a cross section that is equivalent to the break/orifice diameter. This volume is connected to the second component, a tank. The tank component is a constant pressure boundary condition, and it is set to ambient pressure. The fluid initial conditions of temperature, pressure, and vapor pressure can be seen in Figure 2. The temperature at the top of the pipe is 160°C. The total simulated time is two seconds (2 s) after the blowdown with special attention to the first 20 ms of the transient. The simulations’ outputs are the pressure values of those volumes corresponding to the pressure transducers, locations (Table 1).

3.2. Results of the Simulations. In order to assess the capability of the WAHA computer code to simulate the two-phase flow decompression blowdown, the influence that different parameters have on the results has been tested. In the next subsections, the numerical parameters analyzed are the Courant number, order of accuracy of the calculation and the number of volumes dividing the pipe’s length. In the next

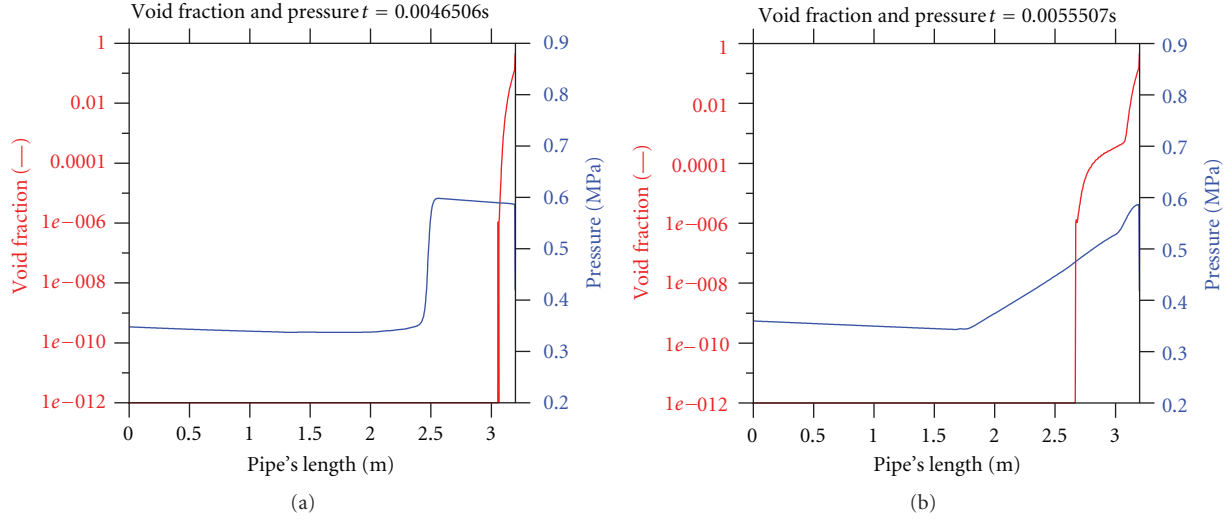


FIGURE 3: Rarefaction (a) and reflected compression (b) wave.

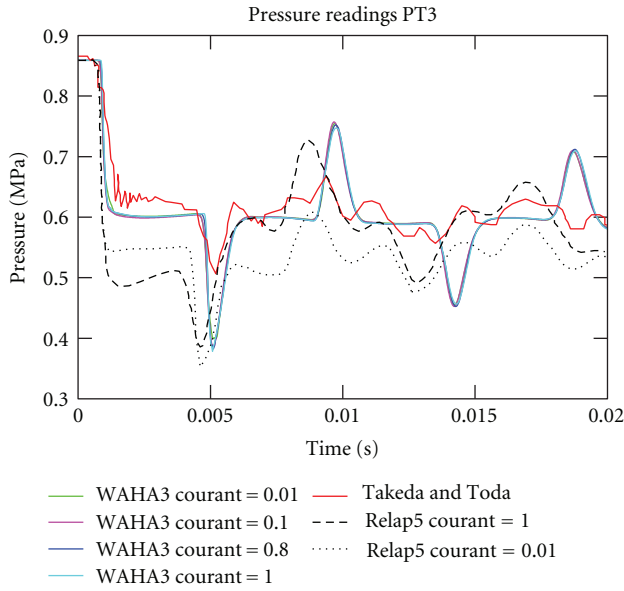


FIGURE 4: Comparison between WAHA, RELAP5 and experimental results for different Courant numbers.

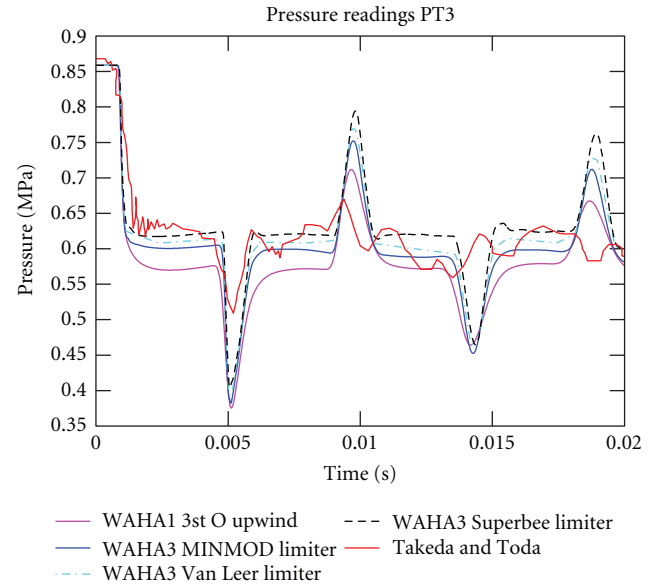


FIGURE 5: Simulation of results using different orders of accuracy.

section, sensitivity to various physical models is shown: role of the pipe elasticity model and wall thickness, and the break flow modeling. Other parameters (results not shown in the present paper) which have no influence on the results were also tested. Those parameters are the wall friction model, material roughness or friction factor. The results presented in this work are compared with the experimental results from [5].

3.2.1. Influence of Courant Number. The convective part of the system of equations in WAHA code, (4) is derived following a finite difference scheme [8]. The stability domain

for its integration is limited by the CFL (Courant-Friedrichs-Levy) condition:

$$\Delta t \leq Co \frac{\Delta x}{\max(|\lambda_k|)}, \quad k = 1, 6, \quad (6)$$

where Co is the Courant number, Δx the spatial increment, Δt the time increment, and λ_k the eigenvalues of the diagonal matrix Λ , which come from the diagonalization of the Jacobian matrix $\mathbf{A}^{-1} \cdot \mathbf{B} = \mathbf{L} \cdot \Lambda \cdot \mathbf{L}^{-1}$ in (4). The eigenvalues provide a good approximation for the sum of the speed of sound in the fluid media (c) and the fluid velocity (u). After the blowdown, a small region with low void fraction appears close to the orifice where the speed of sound is one order of magnitude lower, that is, from approximately 1400 m/s

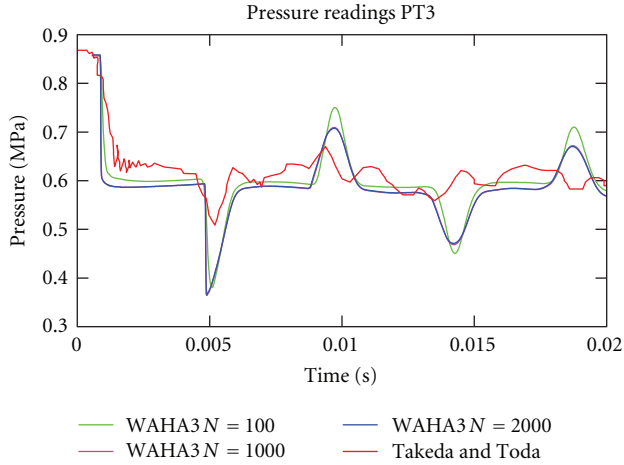


FIGURE 6: Influence of the number of volumes dividing the pipe's length.

in the one-phase liquid region to 50–500 m/s in the two-phase region. The fluid velocity is almost zero in the one-phase region and close to 30 m/s in the two-phase region. Therefore, the most limiting value for Δt resides in the one-phase region where the time increment follows:

$$\Delta t \leq Co \frac{\Delta x}{c + u} \approx Co \frac{\Delta x}{c}. \quad (7)$$

Figure 3 shows the 1 ms time window when the rarefaction wave reaches the two-phase region and then it is reflected as a compression wave. The moment it reaches the two-phase region the pressure drop increases the void fraction near the break [10]. Figure 4 shows the results of the simulations performed with WAHA code using 100 volumes and pipe wall thickness of 3 mm, for different Courant numbers. They are compared with the experimental results and the numerical simulations of the same experiment using the RELAP5 code, published recently by Lafferty et al. [6]. The RELAP5 simulations were performed with the default thermal nonequilibrium model and 99 nodes dividing the pipe section.

A general observation that can be extracted from Figure 4 is that the behavior of the simulated pressure wave is correct when compared with the experimental results from [5]. However, the results in Figure 4 show important differences between the WAHA and RELAP5 codes. While the WAHA simulations are not affected by the Courant number, the RELAP5 results show different pressure drops and subsequent average pressure levels for the two Courant numbers shown here. The first pressure drop value (≈ 0.6 MPa) simulated with WAHA code follows the experimental results closer. Furthermore, WAHA predicts higher pressure amplitudes than RELAP5.

3.2.2. Order of Accuracy of the Calculation. The WAHA code has implemented a combination of first-order upwind discretization and second-order discretization of (3). The problems arising from the pure second-order discretization,

like oscillations near the vicinity of non-smooth solutions can be solved using a combination of the first- and the second-order accurate discretization, that is, with the use of limiters. Limiters account for the smoothness of the solutions. If the solutions are smooth, a larger part of the second-order discretization is used, otherwise larger part of the first-order discretization is used [8, 11]. Figure 5 shows the simulation results for pure first-order upwind discretization and the combination of first- and second-order discretization using the limiters described in [8, 11]. In the transient solved here, the pure second-order implementation gives unstable results and they are not shown. The simulations have been performed with 100 volumes, Courant number equal to 0.8 and pipe wall thickness equal to 3 mm.

The period of the pressure oscillations does not change significantly between the first-order and the combined-order with different limiters. First-order upwind discretization, which is supposed to give the least accurate solution, overpredicts excessively the first pressure drop at the beginning of the simulation. On the other hand, the pressure amplitudes are better estimated. The three limiter options give reasonable results for the first pressure drop, the Superbee limiter the one which follows the experimental results more accurately at the beginning of the simulation. Superbee limiter is supposed to give better results for steepest waves while the most smeared waves are better reproduced with MINMOD. Van-Leer's limiter solution should lie between the solutions obtained with the MINMOD and the Superbee limiters. This can be clearly observed in Figure 5. Superbee limiter gives the highest pressure amplitudes differing from the experimental results. As well, Superbee and Van-Leer solutions give non-physical oscillations after steep pressure changes. Pressure changes with MINMOD limiter are smooth and the pressure amplitudes, although overestimated, are not as high as with Superbee or Van-leer. MINMOD will be used in further sections.

3.2.3. Influence of Number of Volumes. The influence of the number of volumes used to divide the pipe's length can be seen in Figure 6. Three possibilities with N equal to 100, 1000, and 2000 have been tested, despite the general recommendation for 1D models, according to which, the use of volume length lower than the volume diameter often does not make too much sense. Almost no differences can be seen between 1000 and 2000 volumes except the much higher computing time needed to perform the simulations. The required time using 1000 volumes is two hours while the time needed for 2000 volumes goes up to ten hours. The period of the oscillations is practically the same for 100 or 1000 volumes. A small change in the wave behavior can be seen at the lowest pressure value when the rarefaction wave passes by the position PT3, at time 0.005 s. The two main differences that can be observed in Figure 6 are the lower pressure level reached with 1000 volumes after the first pressure drop and the higher pressure amplitudes using 100 volumes. While the first pressure drop is better reproduced using 100 volumes, the pressure amplitude is excessively overpredicted. The number of volumes used to divide the pipe's length gives

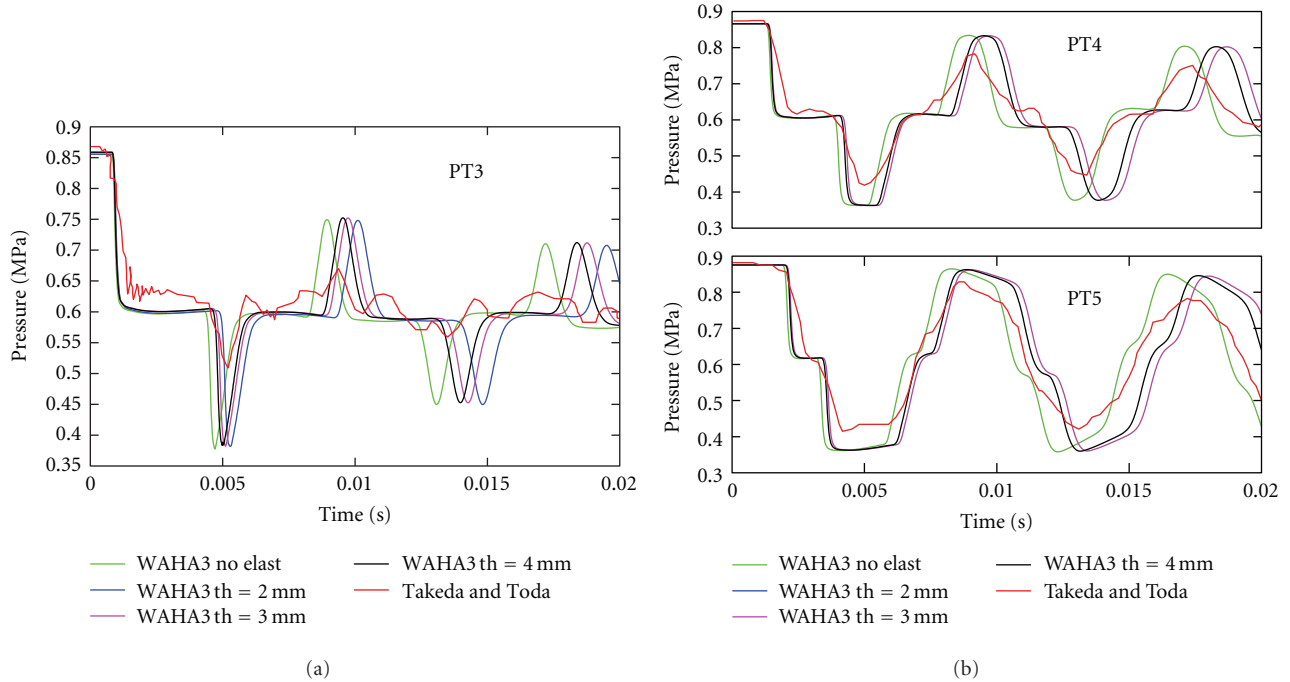


FIGURE 7: Pressure readings at PT3 (a), PT4 and PT5 (b) compared with experiment.

the height of an individual volume. Consequently the last volume, which has a cross section equivalent to the break orifice, has a height of 3.2 cm for 100 volumes and of 3.2 mm for 1000 volumes. In the 100 volumes case, the longer pipe wall at the orifice region produces extra friction effects on the fluid, which finds more difficulties to leave the pipe after the blowdown, decreasing the first pressure drop value. Further on, the pressure in the pipe is kept at higher levels and slightly higher pressure amplitudes are generated after each wave reflection.

No data has been found showing the dimensions of the wall thickness at the top of the pipe where the orifice was machined. It seems more likely that the wall thickness should be similar to the pipe's wall thickness, that is, 3 mm (see Section 4.1), and so the number of volumes to divide the pipe should be 1000.

After the results shown so far, there seems to be no parameter available through the input file, which could further adjust the simulation results to the experimental ones. Further adjustments could be made by changing the physical models inside the code, however, this was avoided in the present work. Slightly lower pressure level is reached after the first blowdown and further pressure amplitudes are clearly overpredicted. Everything seems to point towards extra friction effects, that influenced the experimental results but that aren't considered so far in our simulations, or 3D flow effects at the region close to the break which cannot be modeled with one-dimensional codes. Parameters such as material roughness, the wall friction model, or multiplying friction factor [8] have been tested as well but they did not produce any difference in the results. The fluid velocity in the one-phase region is practically 0. Consequently the influence

of any friction-related parameter is negligible in this region. The fluid velocity in the two-phase region obtained during the simulations is in the order of 30 m/s. The use of reasonable values for the material roughness and friction factor parameter has no influence on the results in this region either. Furthermore, the pressure levels after the two second simulations were compared with the experimental values. The break diameter and downstream pressure (tank pressure) were modified to adjust the long term pressure.

4. Sensitivity of Physical Models

Various physical models were tested to check the sensitivity of the results. Pipe elasticity and break modeling turned out to be relevant and are described below. As mentioned previously, the wall friction model, material roughness or friction factor were tested too, but with no major influence on the results.

4.1. Elasticity Model and Wall Thickness. The pipe elasticity can be taken into account in the WAHA code equations [1, 2]. Pipe elasticity reduces the effective sonic velocity in the pipe [9]:

$$\frac{1}{c^2} = \frac{1}{c_0^2} + K \cdot \rho, \quad (8)$$

where $K = D_p / (t_{pw} \cdot E)$ as in (2), c is the effective sound velocity and c_0 is the sonic velocity in the pure fluid.

In Figure 7 one can observe the influence that the material elasticity has on the results. Three pipe wall thicknesses (2, 3 and 4 mm) and the results without elasticity (or stiff pipe) are compared, because the wall thickness is not

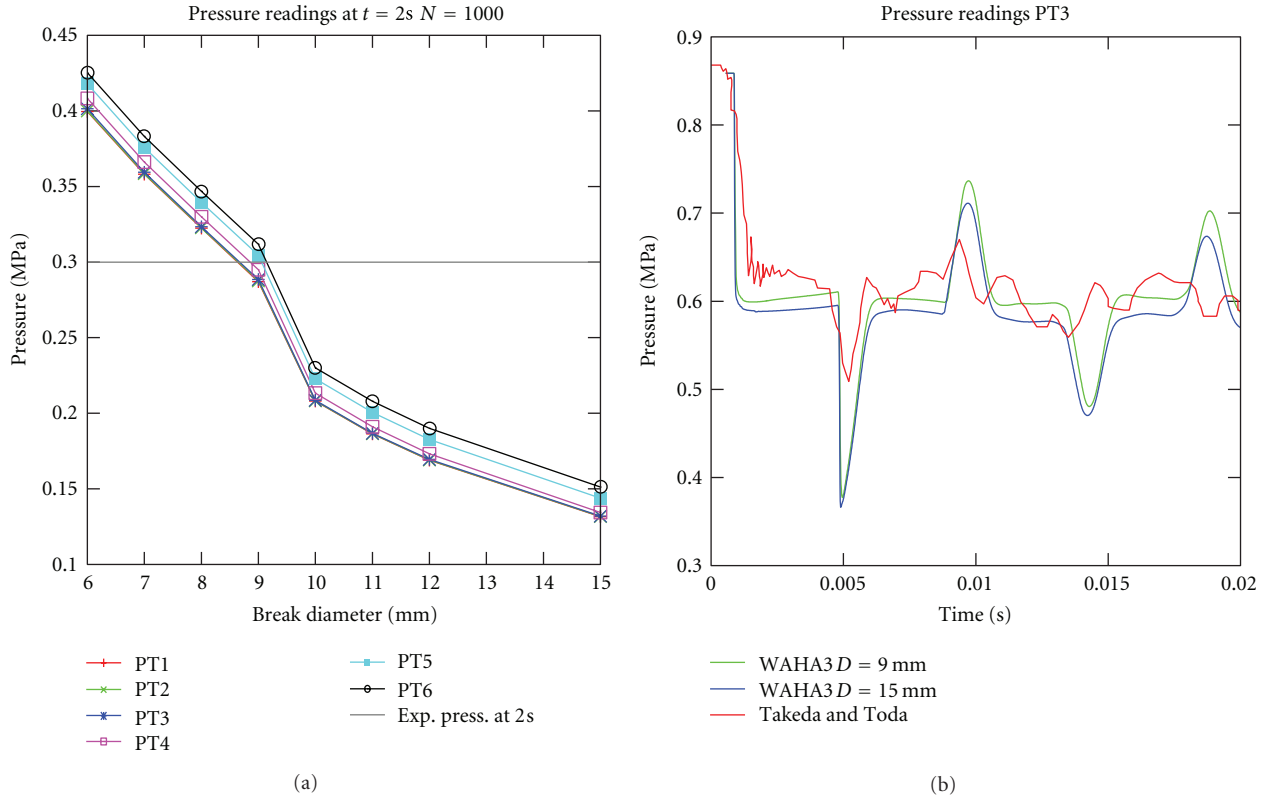


FIGURE 8: (a) Final simulated pressure at PT locations using different break diameters. (b) PT3 pressure readings using 9 and 15 mm break diameters.

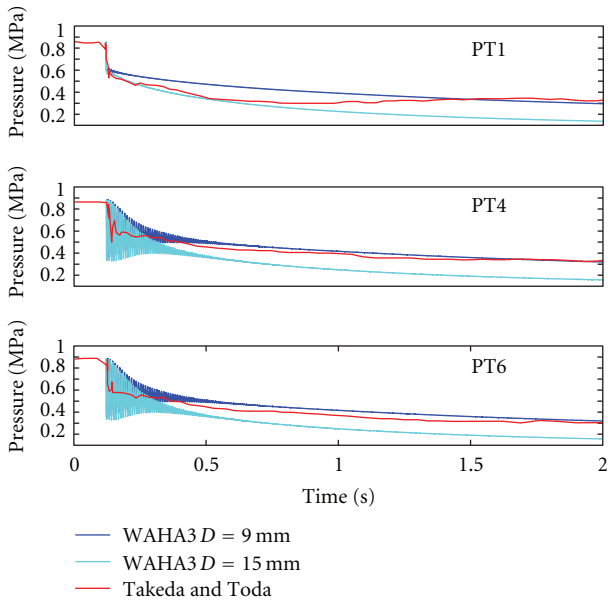


FIGURE 9: Time 2 s pressure readings using 9 and 15 mm break diameters.

available in the experiment’s description. The simulations were performed using 100 volumes dividing the pipe’s length, Courant number equal to 0.8 and pipe’s material with elastic

modulus of 2.0×10^{11} Pa. The first pressure drop at the beginning of the experiment is slightly overpredicted but the average pressure follows the experimental data quite well. The pressure wave amplitude is clearly overpredicted at PT3 location but it is less at PT4 and PT5. The period of the simulated wave observed at PT4 and PT5 positions agrees with the experimental results as well. The influence of the pipe elasticity is clear observing the results from the figure. When a completely stiff pipe is considered, meaning that material elastic modulus (or the pipe wall thickness) is infinity, the period at PT4 and PT5 closely matches the experimental data. On the other hand, the pressure drop generated by the rarefaction wave is too fast. This can be seen in PT3 location at 0.005 s. If the pipe elasticity is considered, the pressure wave is slower. Thinner the pipe wall, higher is the wave period. The results for pipe thickness equal to 3 mm match the time of the experimental lower pressure value at 0.005 s. Furthermore, for a 53.5 mm internal diameter stainless steel pipe, a thickness of 3 mm seems to be the best assumption [12].

4.2. *The Break Diameter.* The results of the fluid pressure after two seconds transient obtained with the WAHA code are half the value of the experimental results (Figure 8). One of the reasons to explain this behavior could be that the effective orifice diameter was smaller than 15 mm due to failure of the Mylar paper to break completely generating

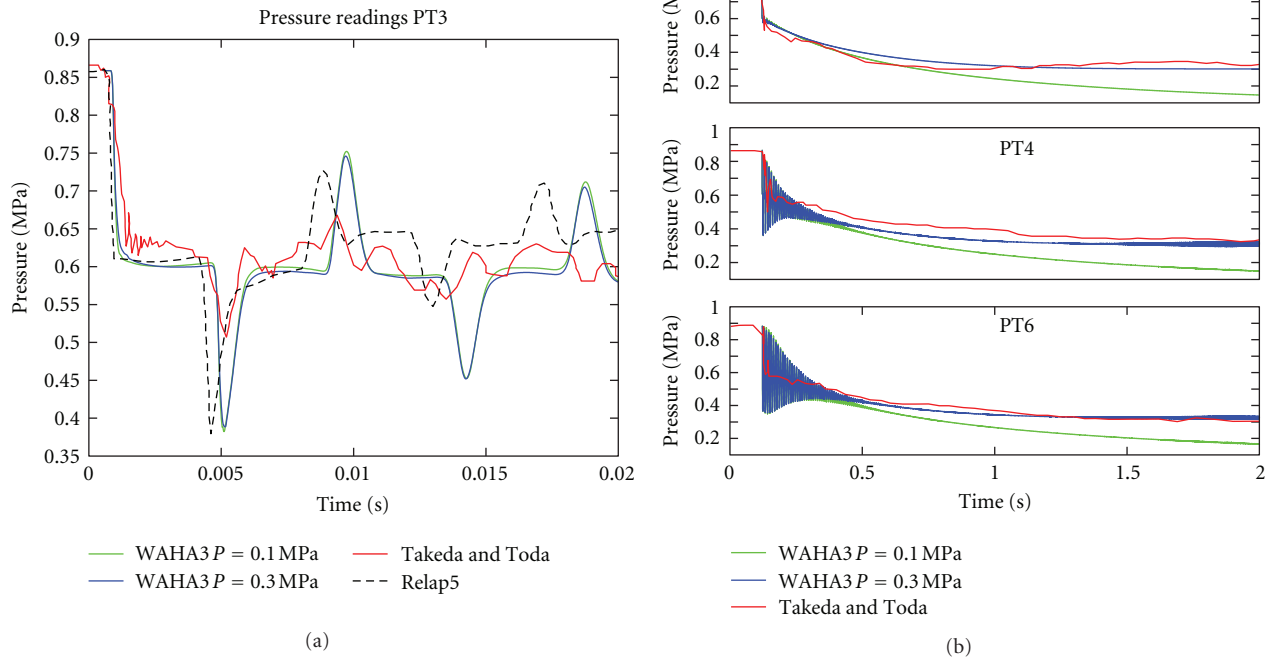


FIGURE 10: (a) Influence of tank pressure to the simulated results and comparison with experiment and RELAP5. (b) time 2 s transient with different tank pressures.

unaccounted pressure drops. The pressure value obtained in [5] after two seconds blowdown was approximately 0.3 MPa, and it can be seen as a horizontal line in Figure 8(a). We can also observe in the figure the pressure values at the six pressure transducers locations using different simulated break diameters. The simulations were performed using 1000 volumes, MINMOD limiter, courant number 0.8 and pipe wall thickness 3 mm. It can be seen that with a 9 mm break diameter the final experimental pressure can be reached while with the 15 mm diameter, the pressure is exactly half the experimental value. Diameters from 6 to 9 mm are modeled slightly different using the WAHA code. Recommendation for simulations with smooth area change model in WAHA code manual (Section 4.2.2 in [8]) is to avoid cross-section ratios, between neighboring volumes, exceeding a factor of roughly 2. Thus, due to the big difference between the dimensions of the pipe and break diameters, the top three volumes have decreasing cross sections, modeling a kind of “bottle neck” at the top of the pipe. For D_b smaller than approximately 10 mm, the ratio with the pipe diameter is $D_p/D_b > 5.35$. Figure 8(b) shows the first 20 ms of the transient modeled using 15 mm and 9 mm break diameter and they are compared with the experimental results. Figure 9 shows the same comparison but for the 2 s time simulations.

The short-term effects using 9 mm break diameter are a slightly lower initial pressure drop, but higher pressure amplitudes, Figure 8(b). Like with the number of volumes, the results are not conclusive. On the other hand, looking at the 2 s results (Figure 9), at PT4 and PT6 locations the

experimental pressure level is followed quite well by the simulations using $D_b = 9$ mm. It has to be pointed out that the simulated pressure oscillations at those locations are kept for a longer time and higher in magnitude compared to the experimental data. The final pressure level at PT1 is the same as in the experiment. WAHA code simulated a smooth pressure decrease during the 2 s transient while the experiment showed slightly lower pressure levels between 0.5 and 0.75 s and then the pressure went up to 0.3 MPa. The initial pressure decrease tendency at PT1 during first 0.5 s seems to be followed more accurately modeling the break using 15 mm diameter.

4.3. Downstream—Tank Pressure Influence. Another reason for the 2s experimental pressure values to be higher than the simulated ones could be a back pressure downstream of the break orifice higher than 0.1 MPa. The experimental facility had mounted a ball valve and an exhaust pipe downstream of the break orifice. The exhaust pipe diameter was not much bigger than the pipe diameter and not far from the break orifice the exhaust pipe had an elbow. Most likely the pressure right after the break was not exactly constant to 0.1 MPa, as it was initially modeled in WAHA by the use of the tank boundary condition. No pressure readings were taken at locations after the break orifice in [5]. The pipe downstream of the break has not been modeled with WAHA but the tank pressure has been set at higher values to match the experimental results, as can be seen in Figure 10(b). The break diameter used in the simulations is 15 mm. It can be seen that with a tank pressure of 0.3 MPa, the pressure

at PT1 and PT6 locations follows the experimental results closely and at PT4 the pressure is a bit underpredicted. Furthermore, at PT1 the experimental results follow initially the simulations using a tank pressure of 0.1 MPa and then move towards those with values using 0.3 MPa. Despite the discrepancies, the results look quite promising.

Looking at Figure 10(a), one can observe the pressure at PT3 for 20 ms transient with tank pressure of 1 and 3 atm. They are compared with the experiment and the RELAP5 results [6]. In this case RELAP5 simulations were performed with a reduced discharge coefficient of 0.5 and different bubble diameter by setting a Laplace length factor of 0.1. RELAP5 approaches slightly better the first pressure drop value from the experiment but the rarefaction wave passes PT3 location too soon, at $t = 0.005$ s. The WAHA results instead do not seem to be affected excessively during the 20 ms transient due to an external pressure of 3 atm. We can see that the pressure amplitude is a bit lower with a tank pressure of 3 atm which is the desired behavior. The time for the rarefaction wave is better predicted compared to the RELAP5. Also the average pressure level seems to be better reproduced with the WAHA code.

Due to these last results we can conclude that a smaller effective break diameter together with downstream unexpected back pressure and 3D fluid flow effects before the pipe break are probably the reasons for the overestimated pressure amplitudes and the lower value of the first pressure drop obtained with the simulations.

5. Conclusions

In the present paper, the in-house computer program WAHA version 3 is used to reproduce the subcooled decompression under temperature gradient experiment performed by Takeda and Toda in 1979. The WAHA code is a one-dimensional six-equation two-fluid solver developed for simulations of the two-phase flow water hammer phenomena. The equations for the two-phase flow are implemented in non-conservative form and the pipe elasticity effects are taken into account.

Different WAHA parameters have been tested such as the pipe elasticity model and wall thickness, the Courant number, order of accuracy of the calculation and the number of volumes that divide the pipe. The WAHA code can't reproduce perfectly the experimental results. The main problem resides in the overpredicted pressure amplitudes. The first pressure drop after the blowdown is also slightly overpredicted. The period of the wave though follows very well the experimental one. Extra friction effects that had influenced the experimental results but that are not considered so far in our simulations or 3D flow effects at the region close to the break which can't be modeled with one-dimensional codes seem to be the reasons for the disagreement. Parameters such as material roughness, the wall friction model or multiplying friction factor have been tested as well but did not produce any significant difference in the results.

In order to improve the results, the influence of different effective break diameters is checked and it is found that the 2 s transient experimental pressure value can be obtained

with a break diameter of 9 mm. Further on, the influence of the downstream pressure after the break is also tested. With a boundary condition of 0.3 MPa tank pressure after the break, the final experimental pressure is also obtained. The first pressure drop is the same and the pressure amplitudes, although still overpredicted, are slightly lower. The comparison of the WAHA results with recent RELAP5 simulations of the same experiment shows that WAHA code follows the experimental data more accurately although the pressure amplitudes are highly overpredicted. In order to further improve the WAHA model of the experiment, pressure readings downstream of the break orifice would be of a big advantage.

Acknowledgment

The authors gratefully acknowledge the financial contribution of the Slovenian Research Agency through the Research Project J2-4078 and Research Program P2-0026.

References

- [1] A. Bergant, J. M. C. Westende, T. van't Koppel et al., "Water hammer and column separation due to accidental simultaneous closure of control valves in a large scale two-phase flow experimental test rig," Proceedings of the ASME Pressure Vessels & Piping Division/K-PVP Conference, Bellevue, Wash, USA, July 2010.
- [2] P. Hermansky and M. Krajščovič, "The dynamical loading of the WWER440V213 reactor pressure vessel internals during LOCA accident in hot and cold leg of the primary circuit," in *Proceedings of the International Conference Nuclear Energy for New Europe*, Portorož, Slovenia, September 2010.
- [3] "RELAP5/MOD3 Code Manual," vol. 1–7, The RELAP5 Code Development team, NUREG/CR-5535, EG&G, Idaho Falls, Idaho, USA, 1995.
- [4] A. R. Edwards and T. P. O'Brien, "Studies of phenomena connected with the depressurization of water reactors," *Journal of the British Nuclear Energy Society*, vol. 9, no. 2, pp. 125–135, 1970.
- [5] Y. Takeda and S. Toda, "Pressure oscillation in subcooled decompression under temperature gradient," *Journal of Nuclear Science and Technology*, vol. 16, no. 7, pp. 484–495, 1979.
- [6] N. Lafferty, V. Ransom, and M. L. de Bertodano, "RELAP5 analysis of two-phase decompression and rarefaction wave propagation under a temperature gradient," *Nuclear Technology*, vol. 169, no. 1, pp. 34–49, 2010.
- [7] B. Končar and M. Borut, "Wall function approach for boiling two-phase flows," *Nuclear Engineering and Design*, vol. 240, no. 11, pp. 3910–3918, 2010.
- [8] "WAHA3 Code Manual," IJS-DP-8841, Institute Jožef Stefan, Ljubljana, Slovenija, 2004.
- [9] E. B. Wylie and V. L. Streeter, *Fluid Transients*, 1978.
- [10] I. Kljenak and B. Mavko, "Simulation of void fraction profile evolution in subcooled nucleate boiling flow in a vertical annulus using a bubble-tracking approach," *Heat and Mass Transfer*, vol. 42, no. 6, pp. 552–561, 2006.
- [11] R. J. LeVeque, *Numerical Methods for Conservation Laws*, Lectures in Mathematics, ETH, Zurich, Switzerland, 1992.
- [12] "B36. 10 welded and seamless wrought steel pipe and B36. 19 stainless steel pipe," ASME/ANSI Standards.

Research Article

Validation and Application of the Thermal Hydraulic System Code TRACE for Analysis of BWR Transients

V. H. Sánchez,¹ M. Thieme,² and W. Tietsch³

¹*Institute for Neutron Physics and Reactor Technology (INR), Karlsruhe Institute of Technology (KIT), 76344 Eggenstein-Leopoldshafen, Germany*

²*TÜV SÜD Industrie Service GmbH, Westendstraße 199, 80686 Munich, Germany*

³*Westinghouse Electric Germany GmbH, 68140 Mannheim, Germany*

Correspondence should be addressed to V. H. Sánchez, victor.sanchez@kit.edu

Received 13 April 2012; Accepted 7 August 2012

Academic Editor: Boštjan Končar

Copyright © 2012 V. H. Sánchez et al. This is an open access article distributed under the Creative Commons Attribution License, which permits unrestricted use, distribution, and reproduction in any medium, provided the original work is properly cited.

The Karlsruhe Institute of Technology (KIT) is participating on (Code Applications and Maintenance Program) CAMP of the US Nuclear Regulatory Commission (NRC) to validate TRACE code for LWR transient analysis. The application of TRACE for the safety assessment of BWR requires a throughout verification and validation using experimental data from separate effect and integral tests but also using plant data. The validation process is normally focused on safety-relevant phenomena for example, pressure drop, void fraction, heat transfer, and critical power models. The purpose of this paper is to validate selected BWR-relevant TRACE-models using both data of bundle tests such as the (Boiling Water Reactor Full-Size Fine-Mesh Bundle Test) BFBT and plant data recorded during a turbine trip event (TUSA) occurred in a Type-72 German BWR plant. For the validation, TRACE models of the BFBT bundle and of the BWR plant were developed. The performed investigations have shown that the TRACE code is appropriate to describe main BWR-safety-relevant phenomena (pressure drop, void fraction, and critical power) with acceptable accuracy. The comparison of the predicted global BWR plant parameters for the TUSA event with the measured plant data indicates that the code predictions are following the main trends of the measured parameters such as dome pressure and reactor power.

1. Introduction

The use of validated numerical simulation tools for the analysis of the plant response under off normal conditions is mandatory. In the framework of the Code Applications and Maintenance Program (CAMP) of the US NRC, the TRACE code is being validated for LWR safety investigations [1]. An extensive validation of coupled neutron kinetics/thermal hydraulic codes is taking place worldwide in the frame of national and international benchmarks related to both pressurized and boiling water reactors (PWR and BWRs) using plant data such as the Peach Bottom turbine trip test [2, 3], the Oskarshamn-2 Instability event [4] and the Ringhals Loss of Feedwater Case [5]. The Karlsruhe Institute of Technology (KIT) is participating on CAMP program and performing validation work for light water reactors (LWRs) [6] and Generation 4 reactors [7]. For the validation of safety-relevant

TRACE heat transfer models, data from different bundle tests such as the NUPEC BFBT and PSBT (PWR Subchannel and Bundle Test) tests are available from the international OECD/NEA Benchmarks [8, 9]. Important data for the validation of models related to single and two-phase flow pressure drop, void fraction, burnout, and DNB are accessible to benchmark participants. For the validation of void models of the CHAN component in TRACE, data from several void fraction steady-state tests performed at the BFBT facility were simulated by TRACE [10].

In addition, 69 pressure drop tests and 151 critical power steady-state tests were investigated [11]. Furthermore, plant data from BWR plant events are used by KIT for the overall TRACE validation [12, 13].

The assessment of pressure drop, void fraction, and critical power is essential for BWR analysis since any change in the thermal hydraulic conditions of the core will impact

the neutron moderation and population in the core. Moreover any pressure change in the core will lead to a change of the void fraction distribution, and subsequently the core power will change depending of the perturbation. The validity of the thermal hydraulic models of a safety analysis tool like TRACE needs to be validated against experimental data gained in single effect, bundle, integral tests, or using plant data.

In this paper, details of BFBT tests and of the experiments used for the validation of the TRACE will be presented. The TRACE modelling of the BFBT test will be described indicating the parameter ranges and types of measured data available. A discussion of the comparison of TRACE predictions with BFBT test data will follow. The turbine trip event occurred in a German BWR plant will be briefly discussed followed by a description of the plant model developed for TRACE to simulate the turbine trip event. Finally, a comparison of TRACE calculations with selected measured data of the plant is given, and the main results are discussed.

2. Validation of TRACE for BWR Applications

2.1. Short Description of BFBT Tests. The BFBT facility from NUPEC in Japan has been used for measuring the void fraction and critical power for typical BWR reactor conditions [8]. Experiments covering a wide range of BWR-operating conditions (max. pressure of 10.3 MPa, max. liquid temperature of 588.15 K, max. power of 12 MW, and a max. flow rate of 20.83 kg/s) can be performed. In the test section of the facility, representative fuel assemblies with different fuel rod arrangements and water rods can be arranged. The fuel rod simulator consists of a heater (Nichrome) of 3.65 mm outer diameter, an insulator (Boron nitride) of 4.85 mm, and the cladding (Inconel 600) of 6.15 mm outer diameter. The heated length is 3.708 m height.

The NUPEC BFBT tests were focused on the investigation of pressure drop for single- and two-phase flow situations, void fraction (steady state and transient) as well as critical power (steady state and transient) for different BWR assembly arrangements, radial and pin power distributions, and bundle axial power profiles.

The differential and absolute pressures were measured using diaphragm transducers located at different axial locations as shown in Figure 2. Two different systems were used in BFBT to measure the averaged void fraction at three axial bundle elevations (X-ray densitometers) and to measure the detailed void distributions at radial plane located at the upper bundle part (X-ray CT scanner). The rapid temperature escalation when critical power conditions are achieved was measured using thermocouples distributed at radial planes located at four axial positions in the upper part of the test section, where burnout is expected to occur. The critical power was measured by slowly increasing the bundle

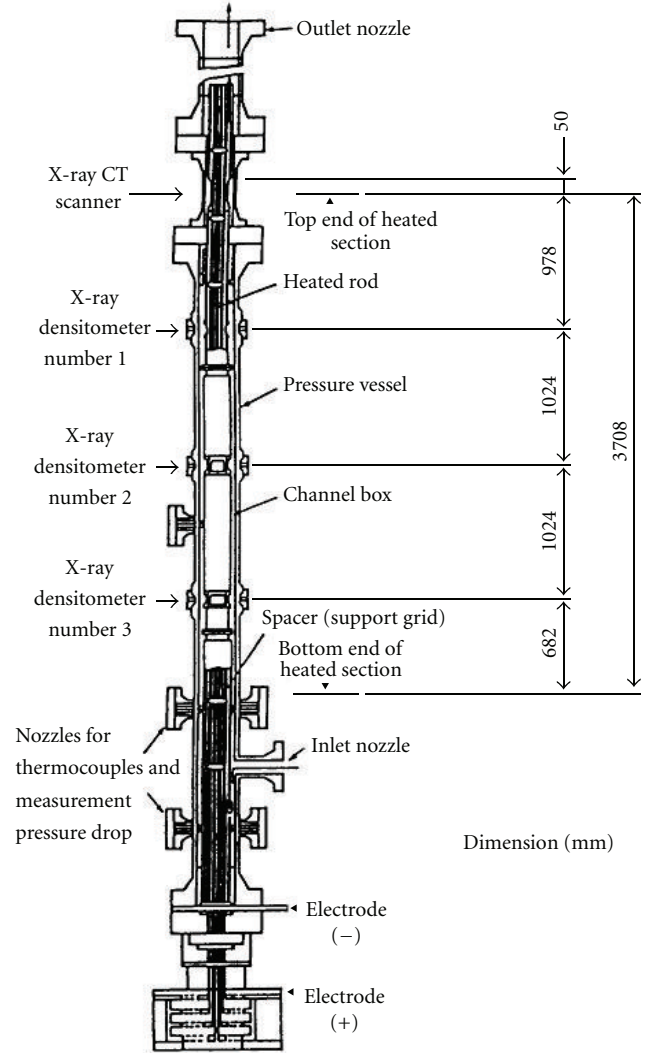


FIGURE 1: Vertical cut of the NUPEC BFBT test facility.

power while monitoring the individual heater thermocouple signals.

The critical power defined by the benchmark team is reached when the peak simulator surface temperature became 14 K higher than the steady-state temperature level. The inlet flow rate was measured using turbine flow meter. In the heater rods, the surface temperature was monitored at positions just upstream of the spacers by the 0.5 mm diameter chrome-alumel thermocouples, which were located in the heater rod cladding. In Table 1 the estimated accuracy of the measured parameters is given. Three types of void fraction measurements: the sub-channel-averaged void fraction (averaged over more than 400 pixel elements), the local void fraction measured on a 0.3 mm × 0.3 mm square pixel element, and the cross-sectional averaged void fraction (averaged over more than 10⁵ pixel elements). The accuracy of these void fraction measurements depends on the photon statistics of the X-ray source, the detector nonlinearity, and the accuracy of the known fluid condition (temperature and pressure) measurements.

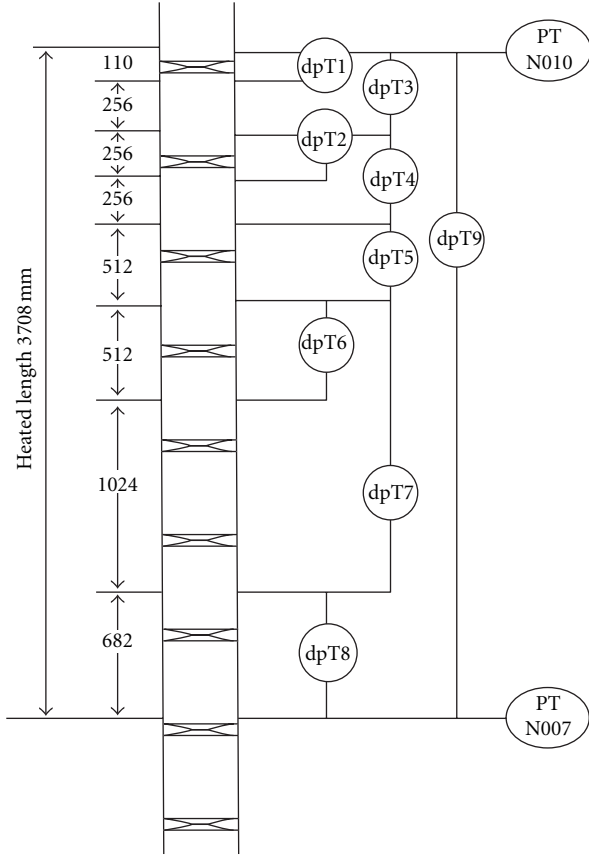


FIGURE 2: Locations of the pressure drop measurements.

TABLE 1: Estimated accuracy of the measured parameters in BFBT test [8].

	Pressure	1%
	Mass flow rate	1%
	Power	1.5%
	Fluid temperature at bundle inlet	1.5° C
X-ray CT scanner	Subchannel void fraction measurements	3%
X-ray CT scanner	Cross-sectional void fraction measurement	2%
X-ray CT scanner	Spatial resolution	0.3 mm × 0.3 mm
X-ray CT scanner	scanning time	15 seconds
X-ray densitometer	Sampling time	Max. 60 seconds

A detailed description of the test series for the pressure drop, void fraction, and critical power measurement can be found in the BFBT benchmark description [8].

2.2. TRACE Model for Post Test Simulation of BFBT Test. TRACE models have been developed for simulating a large number of tests series characterized by the same geometrical arrangement devoted to the measurements of different quantities using and different thermal hydraulic parameters, power profiles, and fuel assembly geometries (no water rods,

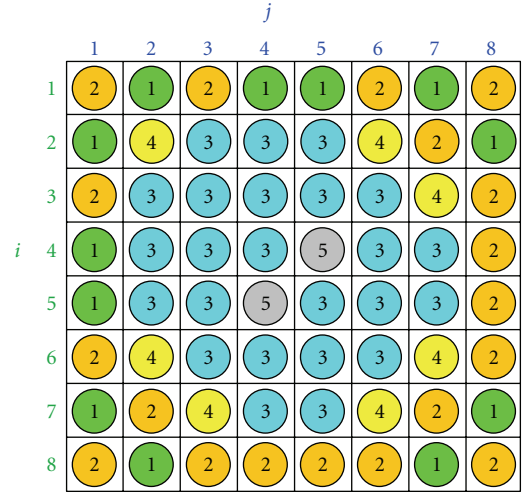


FIGURE 3: CHAN representation of the BFBT bundle.

one water rod, two water rods, and different number of simulator rods). Input decks for the large number of tests were automatically generated using Python scripts taking into account the specific initial and boundary conditions of each test. Hereafter, a TRACE model for the simulation of the experiment number 1071-53 will be described as representative for all other tests to avoid repetition.

The TRACE modelling [10] is focused on the BFBT test section only, that is, the heated zone (heater and water rods) and both lower and upper plenums, where the boundary conditions of each test are defined. For modelling of the bundle part, the BWR-specific CHAN component is used. The bundle conditions at the inlet and outlet are represented in TRACE by the FILL (inlet mass flow and inlet temperature) and the BREAK (outlet pressure) components. The CHAN components allow a very detailed representation of each simulator, water rods, and channel box taking into account the power of each simulator. In Figure 3, the CHAN model of the 8 × 8 – 2 BWR bundle is shown, where each different colour of the simulator indicates a different radial power. The two gray rods are the water rods. In Figure 4 the TRACE representation of the whole test section is shown indicating the axial nodalization (24 nodes) as well as the boundary conditions at the inlet and outlet: FILL (Number 100) and BREAK (Number 300). The seven spacer grids are modelled by an additive pressure drop at the particular positions. Each simulator rod is subdivided in 22 radial mesh points to catch the radial temperature distribution. The bundle power in all heaters (simulator rods) is defined in the POWER component of TRACE. In Figure 3, there are four rod groups (1 to 4) characterized by a different relative radial power, and the two rods number 5 represent the water rods.

2.3. Selected Results of the TRACE Simulations. A detailed description of the assessment of all pressure drop, void fraction, and critical power BFBT tests investigated with TRACE can be found in [10]. Hereafter only selected results demonstrating the validation of the BWR models will be presented.



FIGURE 4: TRACE representation of the heated test section.

2.3.1. *Pressure Drop Tests.* In Figures 5 and 6 a comparison of TRACE predictions with the experimental data for both single- and two-phase flow pressure drop measurements is shown. It can be seen that TRACE tends to underpredict the single-phase pressure drop in the whole pressure range, but the deviations are within the 10% of margin error. On the contrary for the two-phase flow experiments, TRACE predictions are closer to experimental values except for few cases. Almost all predictions are within the 10% margin of error along the whole bundle elevation.

2.3.2. *Void Fraction Tests.* Many void fractions tests were simulated with TRACE, and the results have been compared to the measured data at four axial bundle elevations.

In Figures 7 and 8 predicted void fraction at the bundle outlet and at the upper bundle part is compared to the experimental data of the test series (0-1, 0-2, 0-3, 1, 2, 3, and 4). It can be observed that the majority of the predictions are within the 10% error band, except for few tests. The deviations of the TRACE predictions compared to the data become larger for the lower bundle levels, Figure 8. Based on sensitivity studies, the influence of the four input parameters such as outlet pressure, outlet quality, flow rate and inlet subcooling was investigated [10]. It confirmed that TRACE predictions are worse for low-quality and mass flow conditions [10] since these conditions are not completely in the validation range of correlations.

2.3.3. *Critical Power Tests.* In case of the BFBT critical power tests, TRACE tends to overpredict the measured data. Nevertheless the root square mean error (RSME) is below 0.82 MW [11]. The comparison of the predicted (C) and

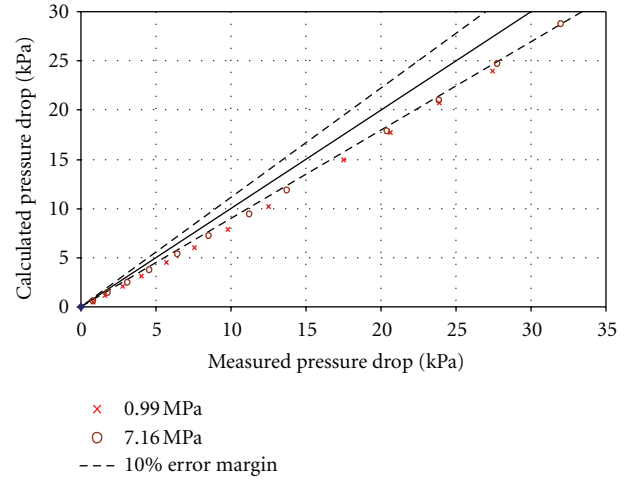


FIGURE 5: Comparison of predicted and measured single-phase pressure drop in BFBT tests.

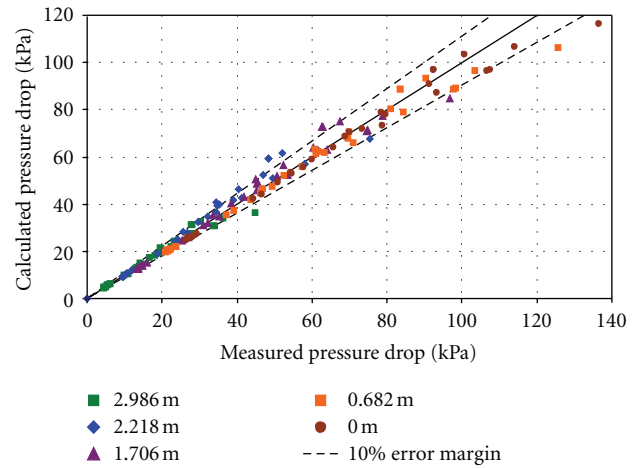


FIGURE 6: Comparison of predicted and measured two-phase pressure drop in BFBT tests.

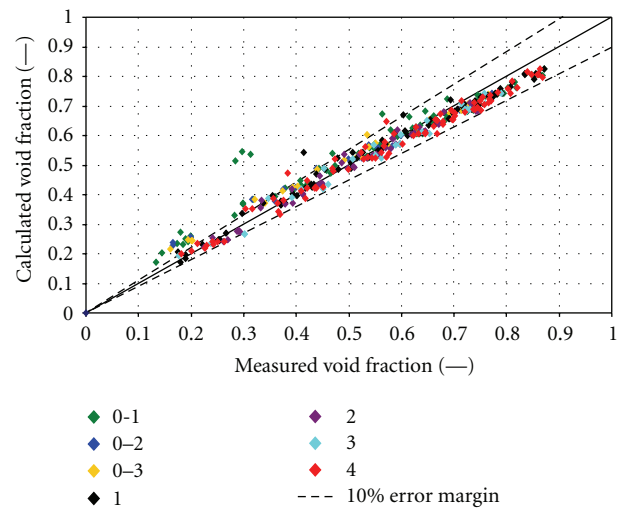


FIGURE 7: Comparison of predicted and measured void fraction results at 3.758 m.

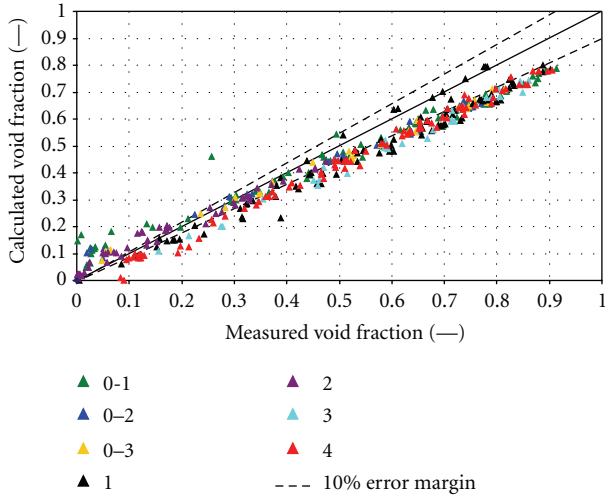


FIGURE 8: Comparison of predicted and measured void fraction results at 2.730 m.

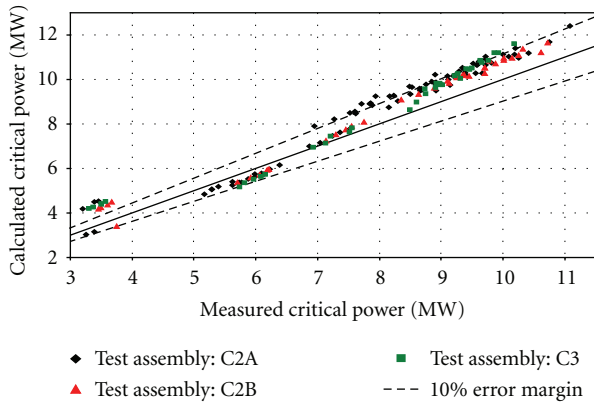


FIGURE 9: Comparison of calculated with measured critical power for different bundle arrangements.

measured (M) critical power is given in Figure 9. There, three regions can be distinguished: (1) for critical power below 4 MW, most of the tests are over predicted; (2) for critical power between 5 and 6.5 MW, TRACE underpredicts the data, but the calculated values are inside the 10% error band; (3) for critical powers above 7 MW, TRACE over predicts the measured data, but a large number of predictions are within the 10% error band. It has to be noted that around the pressure of 7.2 MPa the predicted critical powers are different since the power profile of the assemblies C2A and C2B (cosine shaped) is different from that of C3 (skewed peak shape), see Figure 10. In addition, C2A and C2B have different radial power profiles. TRACE over predicts the measured critical power in the pressure range of 5.5 MPa to 8.6 MPa. Finally Figure 11 indicates that for low mass flux conditions ($<500 \text{ kg/m}^2\text{s}$) the overprediction of TRACE is between 20 and 35% while for larger mass fluxes the predictions are within the 10% error margin [11].

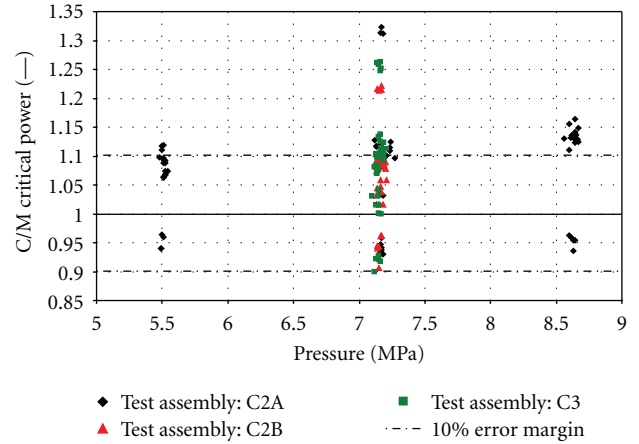


FIGURE 10: C/M ratio as function of the bundle pressure.

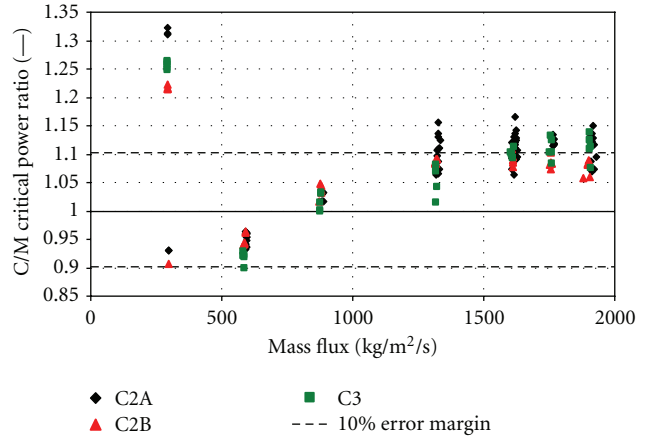


FIGURE 11: C/M ratio as function of bundle mass flux.

3. Application of TRACE for the Simulation of a Turbine Trip Event

For the application of TRACE to simulate BWR transients it is important to demonstrate that TRACE simulates properly real plant events. A turbine trip event in the type-72 German BWR plant that happened in 1998 (cycle 13) was selected for the analysis with the code TRACE using point kinetics model. First of all, the turbine trip event will be described together with the initial and boundary conditions, followed by the description of the developed integral plant model.

3.1. Description of the Turbine Trip Event. The turbine trip event was initiated by the erroneous activation of the condenser controller when the pressure was above 0.3 bar [14]. In reality, the condenser pressure was not higher than 0.145 bar. As a consequence the reactor power was reduced from the nominal value (3840 MWth) to about 35% of nominal power by partial insertion of control rods and reduction of the rotational speed of the eight main recirculation pumps (MRP) to almost minimal value (600 U/min). In

addition, one MRP was shut down due to unknown reasons. Furthermore, four groups of the safety relief valves were manually opened for a short time to hinder a pressure increase in the steam line. It has to be noted that after the turbine stop valve (TSV) started to close, the turbine bypass valve (TBV) started to open. But the diameter of the TBV (bypass line) is smaller than the one of the TSV (steam line). Consequently a pressure increase was propagated from the steam line to the reactor pressure vessel leading to a void collapsing and hence to a power increase. But since the mass flow rate through the core is considerably reduced due to the MRP speed reduction, more void is generated in the core leading to a power decrease.

3.2. Description of the Integral BWR Plant Model. The reference plant is a German BWR of type 72 consisting of eight internal recirculation pumps (MRP). Four steam and feed-water lines are connected to the reactor pressure vessel. In the core 784 fuel assemblies of uranium oxide (UO₂) and mixed oxide fuel (MOX) were loaded in cycle 13.

An integral plant model was developed for TRACE using the three-dimensional VESSEL component for the representation of the reactor pressure vessel (RPV), the CHAN component for the fuel assemblies, the SEPT component to model the separators and dryers in eight groups, the PUMP component to model the MRPs as well as various PIPE components for the representations of the steam and feedwater lines. The VALVE component was used to model the safety relief valves (SRVs) and the TSV and TBV. Finally, the BREAK and FILL components were used to define, for example, the turbine (pressure boundary conditions) and the feed water injection (mass flow rate and temperature). The POWER component using the point kinetics option was selected to describe the power change during the simulation of the transient.

The RPV was subdivided into 22 axial nodes taking into account the constructive peculiarities of the internals below and above the core as well as in two rings and one azimuthal sector (2D model). In Figure 12 the representation of the integral BWR plant model is given. More details of this model are given in [12]. There was shown that a 3D model and a 2D model predict the same results for the TUSA event which represents a global perturbation of the core behaviour. But for the investigation of nonsymmetrical transients like a rod drop accident, a 3D thermal hydraulic model is mandatory to catch the local perturbation of, for example, the reactor power distribution.

Since the dynamic response of the pumps does not play an important role during the TUSA, they were represented by a simplified model.

3.3. TRACE Simulation of the TUSA Event

Steady-State Simulation. Using the described TRACE model of the BWR plant, a steady-state simulation of the plant conditions just before the event occurred was simulated.

It was shown that the predicted parameters were in a good agreement with the reference plant data. Most of the predictions were close to the reference values (deviations less than 5%). Only the pressure drop predicted over the steam dryer showed the largest deviation (about 18%) [12]. For example the water level within the RPV predicted by TRACE amounted 14.49 m compared to the reference value of 14.36 m.

Transient Simulation. Based on the good agreement obtained for the steady-state BWR conditions, the integral model was extended to take into account the boundary conditions during the TUSA event such as the reduction of the recirculation velocity of the 8 MRPs, the opening and closure of the TSV and TBV after the initiation of the event. In addition the reduction of the MRP flow was also taken into account in the modelling of the TUSA event; see Figures 13 and 14. Considering these boundary conditions the TUSA transient was simulated with TRACE using the point kinetics model.

The evaluation of the simulation has shown that the TUSA progression was dominated mainly by the two competing effects, namely, the void reactivity and the Doppler coefficient, in the short term and by the behaviour of the recirculation pumps in the long term.

The magnitude of the void effect was much larger than the one of the fuel temperature increase. As expected, after the TUSA a sharp void collapsing was predicted. This was caused by the pressure wave propagation from the steam line to the core, and it leads to a pressure spike shown in Figure 15.

As a consequence the reactor power increased rapidly due to the increased moderation of the neutrons in the core. Then, the power increase was stopped by the increased void generation in the core as a consequence of the reduction of the core mass flow rate, (see Figure 13) stabilizing after 50 s at a much lower power level (~40%) than the nominal one, as shown in Figure 16. The reactor approached stationary conditions at around 300 s.

Further sensitivity analysis was performed to find out the most important parameters influencing the progression of this TUSA event, specifically the reactor power, the dome pressure, and the water level inside the RPV. To do so, the delay time for the opening (TSV) and closing (TBV) of the steam line valves was varied. It was found out that these parameters can influence the maximal water level as well as the pressure peak and power peak during TUSA. Also the uncertainty in the global reactivity coefficients will influence the response of these global parameters.

4. Summary and Further Work

The presented validation work using BFBT bundle data has shown that TRACE is appropriate to describe the main BWR phenomena. For the single- and two-phase pressure drop tests, TRACE tends to underpredict the single phase pressure drop while the calculation of the two phase pressure drop agrees well with the measured data. A comparison of

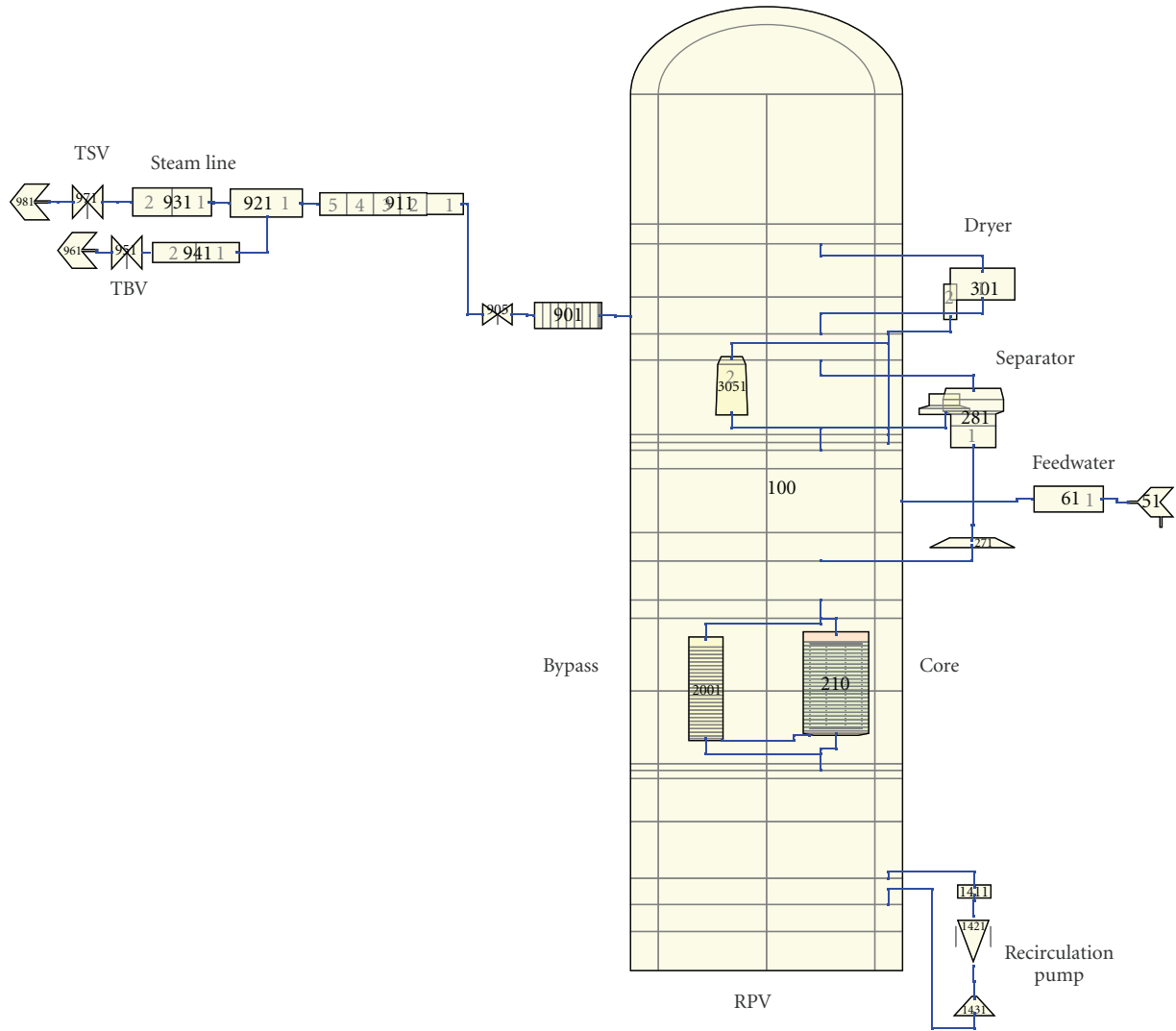


FIGURE 12: Integral BWR plant model of the BWR as represented by SNAP (2D model).

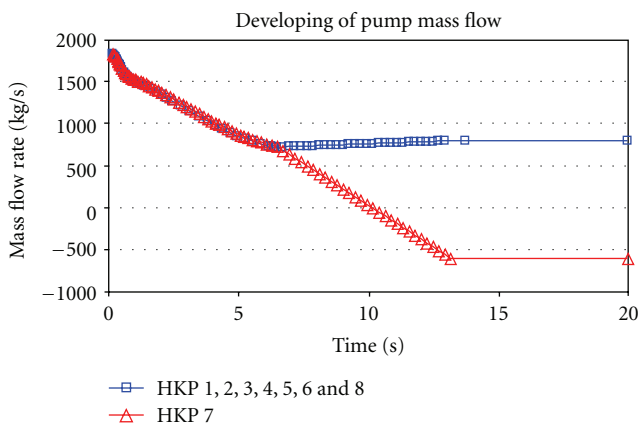


FIGURE 13: MRP mass flow rate during the transient.

predicted void fractions for the different bundle arrangements with the data indicates that TRACE is able to predict

reasonably well the void fraction at all axial measurement positions. The predictions are specifically for the bundle outlet close to the data.

The critical power tests were well predicted with TRACE except for low mass fluxes conditions, where TRACE tends to over predict the critical heat flux. The posttest analysis of the TUSA event with the 2D plant model using point kinetics demonstrated that the predictions are in good agreement with the recorded plant data. Despite these encouraging results, further investigations are needed to improve the code's prediction capability, for example, for burnout under transient conditions. A detailed review of the models for the prediction of the critical power is still necessary. In addition, the qualification of the 3D RPV model of the BWR German plant needs to be performed using plant data for situations where the thermal behavior of the core is asymmetrical. For such situations, the coupling of this 3D thermal hydraulic model with a 3D neutronic core model is needed. This work is already underway [13] and will be published in a subsequent publication.

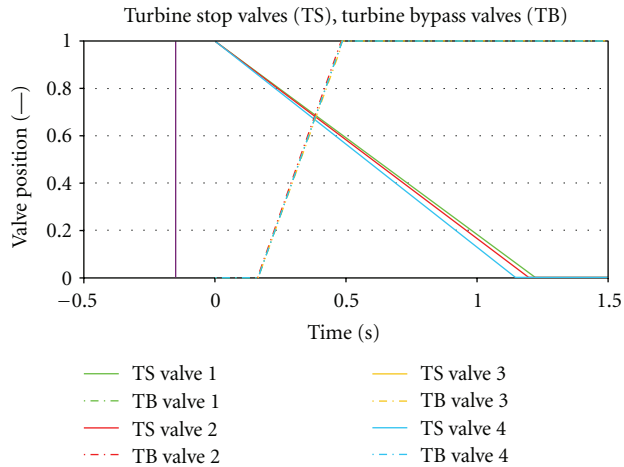


FIGURE 14: Dynamic of the closing and opening of TS and TB.

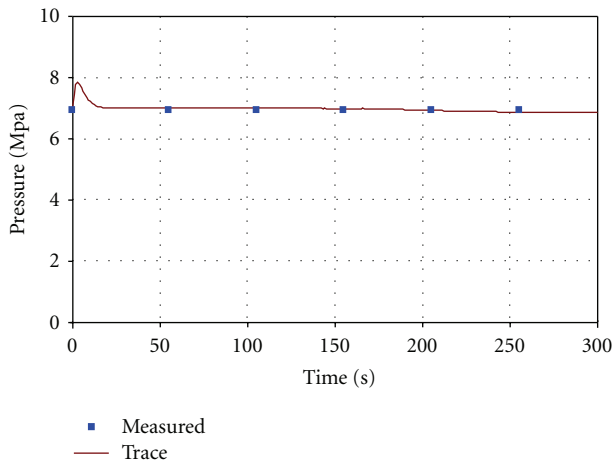


FIGURE 15: Comparison of predicted and measured dome pressure during transient.

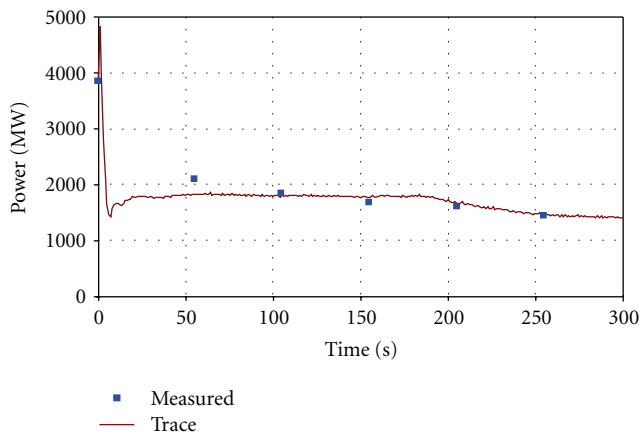


FIGURE 16: Comparison of predicted and measured reactor power during transient.

Abbreviations

BFBT:	Boiling Water Reactor Full-Size Fine-Mesh Bundle Test
PSBT:	PWR Subchannel and Bundle Test
BWR:	Boiling water reactor
CT:	Computer tomography
CAMP:	Code Application and Maintenance Program
LWR:	Light water reactors
NUPEC:	Nuclear Power Engineering Corporation
NRC:	US Nuclear Regulatory Commission
MRP:	Main recirculation pump
MOX:	Mixedoxide fuel
RPV:	Reactor pressure vessel
RSME:	Root square mean error
TUSA:	Turbine trip event
TBV:	Turbine bypass valve
TSV:	Turbine stop valve.

Acknowledgments

The authors greatly appreciate the technical advice from Mr. Holzer (Simpelkamp Nukleartechnik) and Mr. Scholz and Dr. Förster (Nuclear Power Plant Gundremmingen). The fruitful discussions with them helped us to clarify important plant specific issues for the model development. Finally, the authors thank the Program “Nuclear Safety Research” of KIT for the financial support of the Research Topic “Multiphysics Methodologies for Reactor Dynamics and Safety.”

References

- [1] “TRACE V5. 0 assessment manual,” Main Report, U. S. Nuclear Regulatory Commission, Washington, DC, USA, 2005.
- [2] K. Ivanov, A. Olson, and E. Sartori, “OECD/NRC BWR turbine trip transient benchmark as a basis for comprehensive qualification and studying best estimate coupled codes,” in *Proceedings of the International Conference on the New Frontiers of Nuclear Technology (PHYSOR '02)*, Seoul, Korea, October 2002.
- [3] K. Nikitin, J. Judd, G. M. Grandi, A. Manera, and H. Ferroukhi, “Peach bottom 2 turbine trip 2 simulation by TRACE/S3K coupled code,” in *Proceedings of the Advances in Reactor Physics to Power the Nuclear Renaissance Pittsburgh Conference (PHYSOR '10)*, pp. 2283–2293, CD-ROM, American Nuclear Society, Pittsburgh, Pa, USA, May 2010.
- [4] T. Kozłowski, S. Roshan, T. Lefvert et al., “TRACE/PARCS validation for BWR stability based on OECD/NEA oskarshamn-2 benchmark,” in *Proceedings of the 14th Annual Topical Meeting on Nuclear Reactor Thermalhydraulics*, Toronto, Canada, September 2011.
- [5] J. Bánáti, M. Stålek, C. Demazière, and M. Holmgren, “Analysis of a loss of feedwater case at the ringhals-3 NPP using RELAP5/PARCS coupled codes,” in *Proceedings of the 16th International Conference on Nuclear Engineering (ICONE '08)*, pp. 135–144, Orlando, Fla, USA, May 2008.
- [6] W. Jäger and V. Sánchez, “Development of a 3D-VVER-1000-RPV-model for the investigations of a coolant mixing

- experiment with the best-estimate code TRACE,” in *Proceedings of the Annual Meeting on Nuclear Technology*, Karlsruhe, Germany, May 2007.
- [7] W. Jäger, V. Sánchez, and R. Macián-Juan, “On the uncertainty and sensitivity analysis of experiments with supercritical water with TRACE and SUSAN,” in *Proceedings of the 18th International Conference on Nuclear Engineering (ICONE '10)*, Xi'an International Conference Center, May 2010.
- [8] B. Neykov, F. Aydogan, L. Hochreiter, and K. Ivanov, *NUPEC BWR Full-Size Fine-Mesh Bundle Test (BFBT) Benchmark—Volume I: Specifications*, NEA/NSC/DOC(2005)5, Pennsylvania State University, 2005.
- [9] A. Rubin, A. Schoedel, M. Avramova, H. Utsuno, S. Bajorek, and A. Velazquez-Lozada, *OECD/NRC Benchmark Based on NUPEC PWR Subchannel and Bundle Tests (PSBT), Volume I: Experimental Database and Final Problem Specifications*, US NRC OECD Nuclear Energy Agency, 2010.
- [10] M. Thieme, W. Tietsch, R. Macian, and V. Sanchez, “Validation of TRACE using the void fraction tests of the NUPEC BFBT facility,” in *Proceedings of the International Congress on Advances in Nuclear Power Plants (ICAPP '09)*, Tokio, Japan, May 2009.
- [11] M. Thieme, W. Tietsch, R. Macian, and V. Sanchez, “Post-test investigations of BFBT critical power tests with trace,” in *Proceedings of the 17th International Conference on Nuclear Engineering (ICONE '09)*, pp. 503–513, Brussels, Belgium, July 2009.
- [12] M. Thieme, “Qualifizierung des best-estimate programmsystems TRACE für die sicherheitsbewertung von störfallabläufen in siedewasserreaktoren,” Internal Report, 2009.
- [13] Ch. Hartmann, V. Sánchez, and W. Tietsch, “Analysis of a German BWR Core with TRACE/PARCS using different cross section sets,” in *Proceedings of the 14th International Topical Meeting on Nuclear Reactor Thermal Hydraulics (NURETH '11)*, Toronto, Canada, September 2011.
- [14] Rusch, “TUSA Auslösung über hydraulischen Kondensatordruckwächter,” Störungsbericht KRB II, BLOCK C. Aktenzeichen A-30/234. 28. 7., 1998.

Research Article

A Derivation of the Nonlocal Volume-Averaged Equations for Two-Phase Flow Transport

Gilberto Espinosa-Paredes

*Área de Ingeniería en Recursos Energéticos, Universidad Autónoma Metropolitana,
P.O. Box 55-535, Iztapalapa, 09340 Mexico City, DF 09340, Mexico*

Correspondence should be addressed to Gilberto Espinosa-Paredes, gepe@xanum.uam.mx

Received 29 May 2012; Revised 7 August 2012; Accepted 9 August 2012

Academic Editor: Boštjan Končar

Copyright © 2012 Gilberto Espinosa-Paredes. This is an open access article distributed under the Creative Commons Attribution License, which permits unrestricted use, distribution, and reproduction in any medium, provided the original work is properly cited.

In this paper a detailed derivation of the general transport equations for two-phase systems using a method based on *nonlocal* volume averaging is presented. The *local* volume averaging equations are commonly applied in nuclear reactor system for optimal design and safe operation. Unfortunately, these equations are limited to length-scale restriction and according with the theory of the averaging volume method, these fail in transition of the flow patterns and boundaries between two-phase flow and solid, which produce rapid changes in the physical properties and void fraction. The *non-local* volume averaging equations derived in this work contain new terms related with *non-local* transport effects due to accumulation, convection diffusion and transport properties for two-phase flow; for instance, they can be applied in the boundary between a two-phase flow and a solid phase, or in the boundary of the transition region of two-phase flows where the *local* volume averaging equations fail.

1. Introduction

The technique of *local* volume averaging of microscopic conservation equations of motion and transport has received numerous research and analysis [1–16], in order to obtain macroscopic balance equations applicable to multiphase systems. The approximation of *local* volume-averaged conservation equation of two-phase flow is valid when the following length-scale restriction is fulfilled [10]:

$$\frac{\ell}{\mathfrak{V}} \ll 1, \quad (1)$$

where ℓ is the characteristic length of the dispersed phases, and \mathfrak{V} is the characteristic length of the global system:

$$\frac{1}{\mathfrak{V}} = \frac{\text{MAX}_{x \in V_k} |\nabla \langle \psi_k \rangle(x, t)|}{\text{MAX}_{x \in V_k} |\langle \psi_k \rangle(x, t)|}. \quad (2)$$

In this equation ψ_k is the intrinsic property and $\langle \psi_k \rangle$ represents the average and V_k is the volume of k -phase. Then, ℓ is associated where ψ_k varies significantly, and \mathfrak{V} with the changes in $\langle \psi_k \rangle$.

The imposition of the guarantees *good behavior* of the averaged variables. However, the most well-known multiphase flow systems where the length-scale restriction given by (1) are not true: geological systems [17], fractionation of hydrocarbons [18], transport of contaminants [19–21], elimination of contamination in aqueous streams [22], cuttings transport [23–25], and concentration of pharmaceuticals [26], among others that include extraction and separation processes [27]. Specifically, in nuclear systems of BWR type and other industrial applications that involve multiphase flow, the length-scale restriction is no longer satisfied following the transition to churn or slug flow regimes, where the number of bubbles is highly decreased and their size is increased to the length of the magnitude order of the averaging volume, including the whole system, that is, pipe diameter.

The *local* volume averaging of the conservation equations (mass, momentum, and energy) involves averaging the product of a volume-averaged variable $\langle \psi_k \rangle$ (in this paper it was sought to use the nomenclature defined by Lahey and Drew [10]), with the unaveraged variable (φ_k), that is,

$\langle \varphi_k \langle \psi_k \rangle \rangle$ (here ψ_k and φ_k are intensive properties associated with the k phase). The conditions necessary to bring a volume-averaged variable outside the volume integral are the imposing of the length-scale restriction given by (1), that is, $\langle \varphi_k \langle \psi_k \rangle \rangle = \langle \varphi_k \rangle \langle \psi_k \rangle$, with the idea of obtaining manipulated variables associated with the processes of two-phase flow.

Another common case of the *local* volume averaging of the conservation equations is the average product of two unaveraged variables, that is, $\langle \varphi_k \psi_k \rangle$. The traditional representation is $\langle \varphi_k \psi_k \rangle = \alpha_k \langle \varphi_k \rangle \langle \psi_k \rangle + \langle \tilde{\varphi}_k \tilde{\psi}_k \rangle$, where $\tilde{\varphi}_k$ and $\tilde{\psi}_k$ represent the spatial deviations around averaged values of the *local* variables and are defined by the decomposition $\varphi_k = \langle \varphi_k \rangle + \tilde{\varphi}_k$ and $\psi_k = \langle \psi_k \rangle + \tilde{\psi}_k$ [5]. The removal of averaged quantities from the volume integrals is consistent with the length-scale restriction given by (1). The mathematical consequence of this type of inequality can be expressed as $\langle \tilde{\varphi}_k \rangle = 0$ and $\langle \tilde{\psi}_k \rangle = 0$.

However, for more realistic problems, this length-scale restriction given by (1) is not true. In general, this length-scale restriction is not valid within the boundary region (e.g., transition region in two-phase flows) due to significant spatial variations of the two-phase flow structure. The classical length-scale restriction which is implicit in the average transport equations are not satisfied.

In this paper a detailed derivation of the general transport equations for two-phase systems using a method based on *nonlocal* volume averaging, that is, without length-scale restriction is presented. The *nonlocal* volume averaging equations derived in this work contain new terms related to *nonlocal* transport effects due to accumulation, convection diffusion, and transport properties for two-phase flow heat transfer. The *nonlocal* terms were evaluated considering that these are a function of the *local* terms, which yield new coefficients or closure relationships.

2. Preliminaries

The two-phase flow is a system formed by a fluid mixture of l (liquid) and g (gas) phases flowing through a region V as is illustrated in Figure 1. Phase k ($= l, g$) has a variable volume V_k with a total interfacial area of A_k in the averaging volume V , which has an enveloping surface area (A) with a unit normal vector (\underline{n}) pointing outward. A portion of A_k is made of a liquid-gas interphase A_{lg} and a fluid-solid interface A_{kw} . The unit normal vector \underline{n}_k of A_k is always drawn outwardly from phase k , regardless whether it is associated with A_{lg} or A_{kw} .

Local averaging volume

$$V = V_l(t) + V_g(t). \quad (3)$$

Volume fraction g phase in fluid mixture

$$\alpha_g = \frac{V_g(t)}{V}. \quad (4)$$

The method of volume averaging is a technique that can be used to rigorously derive continuum equations for multiphase systems. This means that the equations valid for

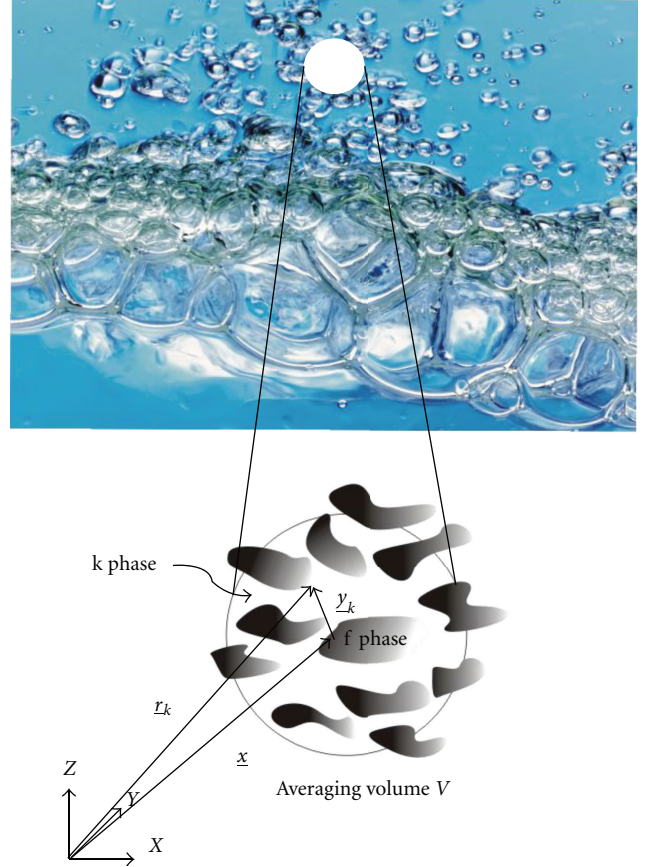


FIGURE 1: Schematic figure of a two-phase flow with a transition region, showing the position vectors and the averaging volume.

a particular phase can be spatially smoothed to produce equations that are valid everywhere, except in the boundaries which contain the multiphase systems.

The volume average operator or superficial volume average $\langle \psi_k \rangle^s$ of some property ψ_k (scalar, vector, or tensor) associated with the k phase is given by

$$\langle \psi_k \rangle^s |_{\underline{x}} = \frac{1}{V} \int_{V_k(\underline{x}, t)} \psi_k(\underline{x} + \underline{y}_k, t) dV, \quad (5)$$

where V is the averaging volume, V_k is the volume of the k phase (contained V), \underline{x} is the position vector locating the centroid of the averaging volume, \underline{y}_k is the position vector at any point in the k phase relative to the centroid, as is illustrated in Figure 1, and dV indicates that the integration is carried out with respect to the components of \underline{y}_k . Then, (5) indicates that the volume-averaged quantities are associated with the centroid. In order to simplify the notation, we will avoid the precise nomenclature used and represent the superficial average of ψ_k as

$$\langle \psi_k \rangle^s = \frac{1}{V} \int_{V_k} \psi_k |_{\underline{x} + \underline{y}_k} dV. \quad (6)$$

The *intrinsic average* is expressed in the form

$$\langle \psi_k \rangle = \frac{1}{V_k} \int_{V_k} \psi_k |_{\underline{x} + \underline{y}_k} dV. \quad (7)$$

These averages will be used in the theoretical development of the two-phase flow transport equations and are related by

$$\langle \psi_k \rangle^s = \alpha_k \langle \psi_k \rangle. \quad (8)$$

With $\psi_k = 1$, the result leads to

$$\langle 1 \rangle^s = \alpha_k. \quad (9)$$

As mentioned above V is a constant, which is invariant in both space and time as illustrated in Figure 1. In this case the volumes of each phase of the flow may change with the position and time, that is, $V_k(\underline{x}, t)$. It should be clear that the volume fraction α_k is a function of the position and time.

When the local instantaneous transport equations are averaged over the volume, terms arise which are averages of derivatives. In order to interchange differentiation and integration in the averaging transport equations, two special averaging theorems are needed. The first one is the spatial theorem [1, 28, 29]

$$\langle \nabla \psi_k \rangle^s = \nabla \langle \psi_k \rangle^s + \frac{1}{V} \int_{A_k} \psi_k |_{\underline{x}+\underline{y}_k} \underline{n}_k dA, \quad (10)$$

where ψ_k is a quantity associated with the k phase, \underline{n}_k is the unit normal vector directed from the k phase towards the f phase, and A_k is the area of the k - f interface contained within V .

The second integral theorem is a special form of the Leibniz rule known as the transport theorem [10, 30]:

$$\left\langle \frac{\partial \psi_k}{\partial t} \right\rangle^s = \frac{\partial \langle \psi_k \rangle^s}{\partial t} - \frac{1}{V} \int_{A_k} \psi_k |_{\underline{x}+\underline{y}_k} \underline{W}_k \cdot \underline{n}_k dA, \quad (11)$$

where \underline{W}_k is the velocity of the k - f interface in V ,

$$A_k = A_{kw} + A_{lg}. \quad (12)$$

If $\psi_k = 1$, the previous theorems lead to

$$\nabla \alpha_k = -\frac{1}{V} \int_{A_k} \underline{n}_k dA, \quad (13)$$

$$\frac{\partial \alpha_k}{\partial t} = \frac{1}{V} \int_{A_k} \underline{W}_k \cdot \underline{n}_k dA. \quad (14)$$

In these theorems ψ_k should be continuous within the k phase.

It is important to note that these theorems are not restricted to the inequality given by (1).

In order to eliminate the point or *local* variable ψ_k in the spatial averaging theorem given by (10) we use the spatial decomposition ($\psi_k = \langle \psi_k \rangle + \tilde{\psi}_k$) [5],

$$\begin{aligned} \langle \nabla \psi_k \rangle^s &= \nabla \langle \psi_k \rangle^s + \frac{1}{V} \int_{A_k} \langle \psi_k \rangle |_{\underline{x}+\underline{y}_k} \underline{n}_k dA \\ &+ \frac{1}{V} \int_{A_k} \tilde{\psi}_k |_{\underline{x}+\underline{y}_k} \underline{n}_k dA. \end{aligned} \quad (15)$$

In the homogeneous regions of the system, the following length-scale restriction given by (1) is usually satisfied, and the following simplification is considered:

$$\langle \psi_k \rangle |_{\underline{x}+\underline{y}_k} \cong \langle \psi_k \rangle, \quad \text{for } \frac{\ell}{\mathfrak{J}} \ll 1. \quad (16)$$

Then, the second term on the right side of (15) can be written as

$$\begin{aligned} &\frac{1}{V} \int_{A_k} \langle \psi_k \rangle |_{\underline{x}+\underline{y}_k} \underline{n}_k dA \\ &= \left\{ \frac{1}{V} \int_{A_k} \underline{n}_k dA \right\} \langle \psi_k \rangle \\ &= -\{\nabla \alpha_k\} \langle \psi_k \rangle, \quad \text{for } \frac{\ell}{\mathfrak{J}} \ll 1. \end{aligned} \quad (17)$$

In general, the averaged terms evaluated in the centroid can be removed from the integrals, where this result was obtained using the lemma given by (13). Then, (15) can be rewritten as follows:

$$\langle \nabla \psi_k \rangle^s = \alpha_k \nabla \langle \psi_k \rangle + \frac{1}{V} \int_{A_k} \tilde{\psi}_k |_{\underline{x}+\underline{y}_k} \underline{n}_k dA, \quad \text{for } \frac{\ell}{\mathfrak{J}} \ll 1. \quad (18)$$

The similar form, the theorem given by (11) can be rewritten as

$$\begin{aligned} \left\langle \frac{\partial \psi_k}{\partial t} \right\rangle^s &= \alpha_k \frac{\partial \langle \psi_k \rangle^s}{\partial t} \\ &- \frac{1}{V} \int_{A_k} \tilde{\psi}_k |_{\underline{x}+\underline{y}_k} \underline{W}_k \cdot \underline{n}_k dA, \quad \text{for } \frac{\ell}{\mathfrak{J}} \ll 1, \end{aligned} \quad (19)$$

where this result was obtained using the lemma given by (14).

The *local* average volume in principle cannot describe significant variations or sudden changes where the characteristic length ℓ can be of the order of \mathfrak{J} . Then, it is necessary to extend the scope of the theorems given by (18) and (19), which is the goal of the next section.

3. Nonlocal Averaged Volume

The spatial decomposition given by $\psi_k = \langle \psi_k \rangle + \tilde{\psi}_k$ represents a *decomposition of length scales*, that is, the average $\langle \psi_k \rangle$ undergoes significant change only over the large length scale, while that the spatial deviation $\tilde{\psi}_k$ is dominated by the small length scale ℓ . However, this idea considered that the *nonlocal* effects are negligible.

Returning to (10) and (11), it clearly indicates that is a *nonlocal* spatial averaging theorem since the dependent variable $\langle \psi_k \rangle$ is evaluated at other points than the centroid (which is indicated by $\langle \psi_k \rangle |_{\underline{x}+\underline{y}_k}$). In this context, we use *nonlocal* in the sense that it does not involve the use of length-scale restriction in its derivation [31, 32].

3.1. Nonlocal Averaged Volume Approximation. The area integral of $\langle \psi_k \rangle |_{\underline{x}+\underline{y}_k} \underline{n}_k$ is evaluated in the k phase indicated by position vector \underline{y}_k shown in Figure 1. Then,

$$\frac{1}{V} \int_{A_k} \langle \psi_k \rangle |_{\underline{x}+\underline{y}_k} \underline{n}_k dA, \quad (20)$$

which is essentially a *nonlocal* term since that the dependent variable $\langle \psi_k \rangle$ is not evaluated at the centroid, \underline{x} (Figure 1).

The nature of the volume-averaged variable $\langle \psi_k \rangle|_{\underline{x}+\underline{y}_k}$ can be known applying a Taylor series expansion about the centroid of the averaging volume [33]:

$$\langle \psi_k \rangle|_{\underline{x}+\underline{y}_k} = \langle \psi_k \rangle + \underline{y}_k \cdot \nabla \langle \psi_k \rangle + \frac{1}{2} \underline{y}_k \underline{y}_k : \nabla \nabla \langle \psi_k \rangle + \dots \quad (21)$$

The second, third, and following terms on the left side correspond to *nonlocal* effects. Then, this equation can be approximate by

$$\langle \psi_k \rangle|_{\underline{x}+\underline{y}_k} = \langle \psi_k \rangle|_{\underline{x}} + \langle \psi_k \rangle_{\text{NL}}, \quad (22)$$

where $\langle \psi_k \rangle_{\text{NL}} = \underline{y}_k \cdot \nabla \langle \psi_k \rangle + (1/2) \underline{y}_k \underline{y}_k : \nabla \nabla \langle \psi_k \rangle + \dots$. Inclusive can be treated as source term formed by $\langle \psi_k \rangle|_{\underline{x}+\underline{y}_k} - \langle \psi_k \rangle$. It is important to emphasize that the presence of the term $\langle \psi_k \rangle_{\text{NL}}$ involves that the *nonlocal* representation avoids imposing length-scale restrictions. Then, the general representation of *nonlocal* term is

$$\langle \psi_k \rangle_{\text{NL}} = \begin{cases} \langle \psi_k \rangle|_{\underline{x}+\underline{y}_k} - \langle \psi_k \rangle, & \text{without length-scale restrictions,} \\ 0, & \text{for } \frac{\ell}{\mathfrak{S}} \ll 1. \end{cases} \quad (23)$$

The physical interpretation of (23) indicates that the *nonlocal* contribution is negligible in the homogeneous region, that is, those portions of the two-phase flow that are not influenced by the rapid changes in the structure which occur in the boundary region. Therefore, *nonlocal* term can be important in the boundary region, where $\langle \psi_k \rangle|_{\underline{x}+\underline{y}_k} - \langle \psi_k \rangle$ is important and the length-scale constraints given by (1) are not valid.

Applying these ideas the theorems can be expressed in *nonlocal* terms:

$$\begin{aligned} \langle \nabla \psi_k \rangle^s &= \alpha_k \nabla \langle \psi_k \rangle \\ &+ \frac{1}{V} \int_{A_k} \langle \psi_k \rangle_{\text{NL}} \underline{n}_k dA + \frac{1}{V} \int_{A_k} \tilde{\psi}_k|_{\underline{x}+\underline{y}_k} \underline{n}_k dA, \end{aligned} \quad (24)$$

$$\begin{aligned} \left\langle \frac{\partial \psi_k}{\partial t} \right\rangle^s &= \alpha_k \frac{\partial \langle \psi_k \rangle}{\partial t} \\ &- \frac{1}{V} \int_{A_k} \langle \psi_k \rangle_{\text{NL}} \underline{W}_k \cdot \underline{n}_k dA \\ &- \frac{1}{V} \int_{A_k} \tilde{\psi}_k|_{\underline{x}+\underline{y}_k} \underline{W}_k \cdot \underline{n}_k dA. \end{aligned} \quad (25)$$

The forms of these integral theorems are applied in this work to obtain *nonlocal* volume-averaged conservation equation for two-phase flow, that is, without restriction of the length scale.

3.2. *Average Volume of the Product of Two Local Variables* $\varphi_k \psi_k$. The explicit representation of the average volume of the product of two *local* variables is given by

$$\langle \varphi_k \psi_k \rangle^s = \frac{1}{V} \int_{V_k} (\varphi_k \psi_k)|_{\underline{x}+\underline{y}_k} dV. \quad (26)$$

Substituting the correspondent spatial deviations for the *local* variables φ_k and ψ_k leads to

$$\langle \varphi_k \psi_k \rangle^s = \alpha_k \langle \varphi_k \rangle \langle \psi_k \rangle + \langle \psi_k \rangle \langle \tilde{\varphi}_k \rangle^s + \langle \varphi_k \rangle \langle \tilde{\psi}_k \rangle^s + \langle \tilde{\varphi}_k \tilde{\psi}_k \rangle^s. \quad (27)$$

This is rewritten as

$$\langle \varphi_k \psi_k \rangle^s = \langle \varphi_k \psi_k \rangle_{\text{NL}} + \alpha_k \langle \varphi_k \rangle \langle \psi_k \rangle + \langle \tilde{\varphi}_k \tilde{\psi}_k \rangle^s, \quad (28)$$

where $\langle \varphi_k \psi_k \rangle_{\text{NL}}$ is a *nonlocal* term, since it involves, indirectly, values of $\langle \varphi_k \rangle$ and $\langle \psi_k \rangle$ that are not associated with the centroid of the averaging volume illustrated in Figure 1. The *nonlocal* contribution is given by

$$\begin{aligned} \langle \varphi_k \psi_k \rangle_{\text{NL}} &= \langle \langle \varphi_k \rangle \langle \psi_k \rangle \rangle^s + \langle \tilde{\varphi}_k \langle \psi_k \rangle \rangle^s \\ &+ \langle \langle \varphi_k \rangle \tilde{\psi}_k \rangle^s - \alpha_k \langle \varphi_k \rangle \langle \psi_k \rangle. \end{aligned} \quad (29)$$

It can be demonstrated that

$$\langle \varphi_k \psi_k \rangle_{\text{NL}} = 0, \quad \text{for } \frac{\ell}{\mathfrak{S}} \ll 1. \quad (30)$$

3.3. *Operators Applied to Two Local Variables* $\varphi_k \psi_k$. The typical expressions in the transport phenomena in a two-phase flow involve an average differential operator with two *local* variables,

$$\begin{aligned} \langle \nabla \varphi_k \psi_k \rangle^s &= \nabla \langle \varphi_k \psi_k \rangle^s + \frac{1}{V} \int_{A_k} \varphi_k \psi_k|_{\underline{x}+\underline{y}_k} \underline{n}_k dA, \\ \left\langle \frac{\partial \varphi_k \psi_k}{\partial t} \right\rangle^s &= \frac{\partial \langle \varphi_k \psi_k \rangle^s}{\partial t} - \frac{1}{V} \int_{A_k} \varphi_k \psi_k|_{\underline{x}+\underline{y}_k} \underline{W}_k \cdot \underline{n}_k dA. \end{aligned} \quad (31)$$

With the previous ideas we obtain expanded form of the theorems for the product of *two-local* variables

$$\begin{aligned} & \langle \nabla \varphi_k \psi_k \rangle^s \\ &= \nabla \langle \varphi_k \psi_k \rangle_{\text{NL}} + \nabla \cdot \langle \varphi_k \rangle \langle \psi_k \rangle + \nabla \cdot \langle \tilde{\varphi}_k \tilde{\psi}_k \rangle^s \\ &+ \underbrace{\left\{ \frac{1}{V} \int_{A_k} \langle \varphi_k \rangle \langle \psi_k \rangle \underline{n}_k dA \right\}_{\text{NL}}}_{\text{nonlocal}} \\ &+ \underbrace{\left\{ \frac{1}{V} \int_{A_k} (\tilde{\varphi}_k \tilde{\psi}_k) |_{\underline{x}+\underline{y}_k} \underline{n}_k dA \right\}_{\text{D}}}_{\text{dispersion}}, \end{aligned} \quad (32)$$

$$\begin{aligned} & \left\langle \frac{\partial \varphi_k \psi_k}{\partial t} \right\rangle^s \\ &= \alpha_k \frac{\partial \langle \varphi_k \rangle \langle \psi_k \rangle}{\partial t} + \frac{\partial \langle \varphi_k \psi_k \rangle_{\text{NL}}}{\partial t} + \frac{\partial \langle \tilde{\varphi}_k \tilde{\psi}_k \rangle^s}{\partial t} \\ &+ \underbrace{\left\{ \frac{1}{V} \int_{A_k} \langle \varphi_k \rangle \langle \psi_k \rangle \underline{W}_k \cdot \underline{n}_k dA \right\}_{\text{NL}}}_{\text{nonlocal}} \\ &+ \underbrace{\left\{ \frac{1}{V} \int_{A_k} (\tilde{\varphi}_k \tilde{\psi}_k) |_{\underline{x}+\underline{y}_k} \underline{W}_k \cdot \underline{n}_k dA \right\}_{\text{D}}}_{\text{dispersion}}. \end{aligned} \quad (33)$$

4. Nonlocal Volume-Averaged General Balance Equations for Two-Phase Flow

The starting point for the development of the *nonlocal* volume-averaged conservation equations is the point conservation equations. In order to illustrate the application of the *nonlocal* theorems and related definitions, we considered the general balance equation for some ψ properties in the k phase:

$$\frac{\partial(\rho_k \psi_k)}{\partial t} + \nabla \cdot (\rho_k \underline{U}_k \psi_k) + \nabla \cdot \underline{D}_k = \rho_k f, \quad (34)$$

where ψ_k is the quantity conserved, \underline{D}_k is the molecular flux, and f is a volumetric source. As summarized in Table 1, depending on the choice of the quantity to be conserved, either of these equations can be used to quantify the mass, momentum, and energy conservation of each phase.

The volume averaged of the general balance equation can be expressed as

$$\left\langle \frac{\partial(\rho_k \psi_k)}{\partial t} \right\rangle^s + \langle \nabla \cdot \rho_k \underline{U}_k \psi_k \rangle^s + \langle \nabla \cdot \underline{D}_k \rangle^s = \langle \rho_k f_k \rangle^s. \quad (35)$$

TABLE 1: Conservation terms.

Conservation principle	ψ_k	\underline{D}_k	f
Mass	1	0	0
Momentum	\underline{U}_k	$\rho_k \underline{I} - \underline{\tau}_k$	\underline{g}_k
Energy	$e_k - p_k/\rho_k$	$\underline{q}_k'' - (\rho_k \underline{I} - \underline{\tau}_k) \cdot \underline{U}_k$	$\underline{g}_k \cdot \underline{U}_k + q_k'''/\rho_k$

Note: $e_k = h_k + U_k^2/2$ is the total specific energy for the k phase, where h_k is the enthalpy.

\underline{q}_k'' denotes the heat flux vector for the k phase.

The *nonlocal* transport theorem of the product of two variables derived in this work given by (33) with $\varphi_k = \rho_k$ is used in order to express the first term of this equation:

$$\begin{aligned} & \left\langle \frac{\partial \rho_k \psi_k}{\partial t} \right\rangle^s \\ &= \alpha_k \frac{\partial \langle \rho_k \rangle \langle \psi_k \rangle}{\partial t} + \frac{\partial \langle \rho_k \psi_k \rangle_{\text{NL}}}{\partial t} + \frac{\partial \langle \tilde{\rho}_k \tilde{\psi}_k \rangle^s}{\partial t} \\ &- \left\{ \frac{1}{V} \int_{A_k} \langle \rho_k \rangle \langle \psi_k \rangle \underline{W}_k \cdot \underline{n}_k dA \right\}_{\text{NL}} \\ &- \left\{ \frac{1}{V} \int_{A_k} (\tilde{\rho}_k \tilde{\psi}_k) |_{\underline{x}+\underline{y}_k} \underline{W}_k \cdot \underline{n}_k dA \right\}_{\text{D}}. \end{aligned} \quad (36)$$

The *nonlocal* averaging theorem for the product of three variables can be developed following the same procedure given by (32). Then, the second term in (35) is given by

$$\begin{aligned} & \langle \nabla \cdot \rho_k \underline{U}_k \psi_k \rangle^s \\ &= \alpha_k \nabla \cdot (\langle \rho_k \rangle \langle \underline{U}_k \rangle \langle \psi_k \rangle) \\ &+ \nabla \cdot \langle \rho_k \underline{U}_k \psi_k \rangle_{\text{NL}} + \nabla \cdot \langle \rho_k \underline{U}_k \psi_k \rangle_{\text{D}} \\ &+ \left\{ \frac{1}{V} \int_{A_k} \langle \rho_k \rangle \langle \underline{U}_k \rangle \langle \psi_k \rangle \cdot \underline{n}_k dA \right\}_{\text{NL}} \\ &+ \left\{ \frac{1}{V} \int_{A_k} (\tilde{\rho}_k \tilde{\underline{U}}_k \tilde{\psi}_k) |_{\underline{x}+\underline{y}_k} \cdot \underline{n}_k dA \right\}_{\text{D}}, \end{aligned} \quad (37)$$

where the dispersion term is given by

$$\begin{aligned} & \nabla \cdot \langle \rho_k \underline{U}_k \psi_k \rangle_{\text{D}} \\ &= \nabla \cdot \langle \rho_k \rangle \langle \tilde{\psi}_k \tilde{\underline{U}}_k \rangle^s + \nabla \cdot \langle \underline{U}_k \rangle \langle \tilde{\rho}_k \tilde{\psi}_k \rangle^s \\ &+ \nabla \cdot \langle \psi_k \rangle \langle \tilde{\rho}_k \tilde{\underline{U}}_k \rangle^s + \nabla \cdot \langle \tilde{\rho}_k \tilde{\underline{U}}_k \tilde{\psi}_k \rangle^s. \end{aligned} \quad (38)$$

The *nonlocal* averaging theorem given by (24) with $\psi_k = \underline{D}_k$ is used in order to obtain the diffusive term

$$\begin{aligned} & \langle \nabla \cdot \underline{D}_k \rangle^s \\ &= \alpha_k \nabla \cdot \langle \underline{D}_k \rangle + \frac{1}{V} \int_{A_k} \langle \underline{D}_k \rangle_{\text{NL}} \cdot \underline{n}_k dA \\ &+ \frac{1}{V} \int_{A_k} \tilde{\underline{D}}_k |_{\underline{x}+\underline{y}} \cdot \underline{n}_k dA. \end{aligned} \quad (39)$$

The terms $\langle \rho_k f_k \rangle^s$ are obtained with the application of (28)

$$\langle \rho_k f_k \rangle^s = \langle \rho_k f_k \rangle_{\text{NL}} + \alpha_k \langle \rho_k \rangle \langle f_k \rangle + \langle \tilde{\rho}_k \tilde{f}_k \rangle^s. \quad (40)$$

In order to simplify the previous equations, the following representations are proposed:

$$\begin{aligned} & \frac{\partial \langle \rho_k \psi_k \rangle_{\text{NL}}}{\partial t} \\ &= \eta_a \alpha_k \frac{\partial (\langle \rho_k \rangle \langle \psi_k \rangle)}{\partial t}, \quad \text{nonlocal accumulation,} \end{aligned} \quad (41)$$

$$\begin{aligned} & \frac{\partial \langle \tilde{\rho}_k \tilde{\psi}_k \rangle^s |_{\underline{x}}}{\partial t} \\ &= \delta_a \alpha_k \frac{\partial (\langle \rho_k \rangle \langle \psi_k \rangle)}{\partial t}, \quad \text{dispersion for accumulation,} \end{aligned} \quad (42)$$

$$\begin{aligned} & \nabla \cdot \langle \rho_k \underline{U}_k \psi_k \rangle_{\text{NL}} \\ &= \eta_b \alpha_k \nabla \cdot (\langle \rho_k \rangle \langle \underline{U}_k \rangle \langle \psi_k \rangle), \quad \text{nonlocal convection,} \end{aligned} \quad (43)$$

$$\begin{aligned} & \nabla \cdot \langle \rho_k \underline{U}_k \psi_k \rangle_{\text{D}} \\ &= \delta_b \alpha_k \nabla \cdot (\langle \rho_k \rangle \langle \underline{U}_k \rangle \langle \psi_k \rangle), \quad \text{dispersion for convection,} \end{aligned} \quad (44)$$

$$\langle \rho_k f_k \rangle_{\text{NL}} = \eta_c \alpha_k \langle \rho_k \rangle \langle f_k \rangle, \quad \text{nonlocal source,} \quad (45)$$

$$\langle \tilde{\rho}_k \tilde{f}_k \rangle^s = \delta_c \alpha_k \langle \rho_k \rangle \langle f_k \rangle, \quad \text{dispersion for source,} \quad (46)$$

where η and δ are dimensionless parameters. The parameter η is the *nonlocal* nature, while the δ parameter agglutinates the dispersion effects. Now, the diffusive flux of (39) can be expressed as

$$\langle \nabla \cdot \underline{D}_k \rangle^s = \alpha_k \nabla \cdot \langle \underline{D}_k \rangle + M_{\text{kNL}} + \tilde{M}_k. \quad (47)$$

In this equation the following definitions were used:

$$\begin{aligned} M_{\text{kNL}} &= \frac{1}{V} \int_{A_k} \langle \underline{D}_k \rangle_{\text{NL}} \cdot \underline{n}_k dA, \\ & \text{interfacial Nonlocal diffusion,} \end{aligned} \quad (48)$$

$$\begin{aligned} \tilde{M}_k &= \frac{1}{V} \int_{A_k} \tilde{\underline{D}}_k |_{\underline{x}+\underline{y}} \cdot \underline{n}_k dA, \\ & \text{interfacial Diffusion due to dispersion.} \end{aligned} \quad (49)$$

Finally, substituting (41)–(49), the *nonlocal* volume-averaged of the general balance equation (without length-scale restriction) finally is obtained:

$$\begin{aligned} & \lambda_a \alpha_k \frac{\partial (\langle \rho_k \rangle \langle \psi_k \rangle)}{\partial t} + \lambda_b \alpha_k \nabla \cdot (\langle \rho_k \rangle \langle \underline{U}_k \rangle \langle \psi_k \rangle) \\ & + \alpha_k \nabla \cdot \langle \underline{D}_k \rangle \\ &= \lambda_c \alpha_k \langle \rho_k \rangle \langle f_k \rangle - M_{\text{kNL}} - \tilde{M}_k - M_{\text{kD}}^\Gamma - M_{\text{kNL}}^\Gamma, \end{aligned} \quad (50)$$

where

$$\lambda = \eta + \delta + 1, \quad (51)$$

$$\begin{aligned} M_{\text{kD}}^\Gamma &= \left\{ \frac{1}{V} \int_{A_k} (\tilde{\rho}_k \tilde{\underline{U}}_k \tilde{\psi}_k) |_{\underline{x}+\underline{y}_k} \cdot \underline{n}_k dA \right\}_{\text{D}} \\ & - \left\{ \frac{1}{V} \int_{A_k} (\tilde{\rho}_k \tilde{\psi}_k) |_{\underline{x}+\underline{y}_k} \underline{W}_k \cdot \underline{n}_k dA \right\}_{\text{D}}, \\ M_{\text{kNL}}^\Gamma &= \left\{ \frac{1}{V} \int_{A_k} (\langle \rho_k \rangle \langle \underline{U}_k \rangle \langle \psi_k \rangle) \cdot \underline{n}_k dA \right\}_{\text{NL}} \\ & - \left\{ \frac{1}{V} \int_{A_k} \langle \rho_k \rangle \langle \psi_k \rangle \underline{W}_k \cdot \underline{n}_k dA \right\}_{\text{NL}}. \end{aligned} \quad (52)$$

Recalling that a portion of A_k is made of a liquid-gas interphase and a fluid-solid interphase A_{kW} . Then, M_{kD}^Γ (and M_{kNL}^Γ) consider the transport phenomena related with interfacial mass transfer between fluid-fluid and fluid-solid interphase, that is, $M_{\text{k}}^\Gamma = M_{\text{kFE}}^\Gamma + M_{\text{wkE}}^\Gamma$ (with $E = \text{D, NL}$).

5. Discussion

The volume averaged of the balance equation with *length-scale* restriction can be obtained starting from the *nonlocal* averaging equation (50), which contains *local* and *nonlocal* terms of the averaged volume. When $\eta \rightarrow 0$, $\langle \rho_k \underline{U}_k \psi_k \rangle_{\text{NL}} \rightarrow 0$, $\langle \rho_k f_k \rangle_{\text{NL}} \rightarrow 0$, $M_{\text{kNL}} \rightarrow 0$, and $M_{\text{kNL}}^\Gamma \rightarrow 0$, the *local* averaging volume equation is recovered. Then, (46) simplifies to

$$\begin{aligned} & (\delta_a + 1) \alpha_k \frac{\partial (\langle \rho_k \rangle \langle \psi_k \rangle)}{\partial t} \\ & + (\delta_b + 1) \alpha_k \nabla \cdot (\langle \rho_k \rangle \langle \underline{U}_k \rangle \langle \psi_k \rangle) + \alpha_k \nabla \cdot \langle \underline{D}_k \rangle \\ & = (\delta_c + 1) \alpha_k \langle \rho_k \rangle \langle f_k \rangle - \tilde{M}_k - M_{\text{kD}}^\Gamma, \quad \frac{\ell}{\mathcal{V}} \ll 1. \end{aligned} \quad (54)$$

The fundamental difference between *local* and *nonlocal* equations is that (50) involves, indirectly, values of the variables that are not associated with the centroid of the averaged volume as illustrated in Figure 1, while in (54) all the values of the volume-averaged variables are associated with the centroid of the averaged volume. The physical interpretation indicates that (54) describes the *homogeneous* two-phase flow. In this work the homogeneous term is used to indicate that the two-phase flow system has a behavior close to that of a homogeneous system; then to ensure homogeneity the system under study is based in *length-scale* restriction used to perform the upscaling in the two-phase flow system. However, (50) has not *length-scale* restriction and in principle it can describe regions of a two-phase flow, where drastic changes occur in the void fraction and transport properties (e.g., diffusivity).

The *nonlocal* volume averaging equations derived in this work contain new terms related to *nonlocal* transport effects due to accumulation, convection diffusion, and transport properties for two-phase flow. In general, the *nonlocal* terms

were evaluated considering them as a function of the *local* terms, yielding new coefficients (η' 's) that can be called *nonlocal* coefficients due to its nature these coefficients were defined through (41), (43), and (45) along with (48) and (53). It is important to note that these last two equations can also be expressed in terms of the *local* terms.

The *nonlocal* coefficients (η' 's) are new closure relationships of the present novel formulation. For the application in a two-phase flow it is necessary as a first approximation to perform an analysis of order of magnitude, with the idea of identifying the predominant effects where the coefficients are not negligible (i.e., the temporal and diffusive effects are negligible). Then, the significant *nonlocal* coefficients can be evaluated with new or existing procedures in the experimental field, theoretical deduction, or numerical simulation, for instance.

The physical meaning of the *nonlocal* coefficients is related to the scaling process, that is, in the transition region as it can be observed in Figure 1. These coefficients act as coupling elements among the phenomena occurring in at least two different length scales. Outside of the interregion the length scales are smaller compared with those near the interregion (Figure 1).

Some examples where *nonlocal* general equation (50) can be applied are where α_k presents abrupt changes [33, 34], in particular transitions of flow patterns, interface with stratified or annular flow drops and bubbles, and others as in the boundary region of the two-phase flow and solid, where the length-scale restriction given by (1) is not valid.

6. Conclusions

In this paper a derivation of the general transport equations for two-phase systems using a method-based on *nonlocal* volume averaging was presented. The *nonlocal* volume averaging equations derived in this work (50) contain new terms related to *nonlocal* transport effects due to accumulation, convection diffusion, and transport properties for two-phase flow.

The *nonlocal* terms were evaluated as a first approximation considering that these are a function of the *local* terms (41), (43), and (45), given as result of the *nonlocal* volume averaging equations (50) for practical applications. The *nonlocal* coefficients (η' 's) are new closure relationships of the present novel formulation. The significant *nonlocal* coefficients can be evaluated with new or existent procedures: theoretical, numerical, and experimental. These coefficients act as coupling elements among the phenomena occurring in at least two different length scales, during the scaling process for pragmatic applications.

To illustrate the application of the representations of the *nonlocal* theorems and related definitions, the general balance equation for some ψ property in the k phase was considered, where it was demonstrated that a *nonlocal* volume averaging balance equation was obtained with meaningful averages. This general balance equation can be applied generally where α_k presents abrupt changes [34, 35], such as transitions of flow patterns, interfaces with stratified

or annular flow drops and bubbles, and others such as in the boundary region of the multiphase system, where the length-scale restriction (1) are not valid.

The *nonlocal* averaging model derived in this work represents a novel proposal and its framework could be the beginning of extensive research, both theoretical and experimental, as well as numerical simulation.

References

- [1] J. C. Slattery, "Flow of viscoelastic fluids through porous media," *AIChE*, vol. 13, pp. 1066–1071, 1967.
- [2] D. A. Drew, "Averaged field equations for two-phase media," *Studies in Applied Mathematics*, vol. 50, no. 2, pp. 133–166, 1971.
- [3] D. A. Drew and L. A. Segel, "Averaged equations for two-phase flows," *Studies in Applied Mathematics*, vol. 50, no. 3, pp. 205–231, 1971.
- [4] J. Bear, *Dynamics of Fluid in Porous Media*, Elsevier, New York, NY, USA, 1972.
- [5] W. G. Gray, "A derivation of the equations for multi-phase transport," *Chemical Engineering Science*, vol. 30, no. 2, pp. 229–233, 1975.
- [6] G. Yadigaroglu and R. T. Lahey, "On the various forms of the conservation equations in two-phase flow," *International Journal of Multiphase Flow*, vol. 2, no. 5–6, pp. 477–494, 1976.
- [7] W. G. Gray and K. O'Neill, "On the general equations for flow in porous media and their reduction to Darcy's law," *Water Resources Research*, vol. 12, no. 2, pp. 148–154, 1976.
- [8] J. M. Delhaye, "Instantaneous space-averaged equations," in *Two-Phase Flows and Heat Transfer*, S. Kakac and F. Mayinger, Eds., vol. 1, pp. 81–90, Hemisphere, Washington, DC, USA, 1977.
- [9] W. G. Gray and P. C. Y. Lee, "On the theorems for local volume averaging of multiphase systems," *International Journal of Multiphase Flow*, vol. 3, no. 4, pp. 333–340, 1977.
- [10] R. T. Lahey and D. A. Drew, "The three-dimensional time and volume averaged conservation equations of two-phase flow," *Advances in Nuclear Science & Technology*, vol. 20, pp. 1–69, 1989.
- [11] R. I. Nigmatulin, "Spatial averaging in the mechanics of heterogeneous and dispersed systems," *International Journal of Multiphase Flow*, vol. 5, no. 5, pp. 353–385, 1979.
- [12] M. Hassanizadeh and W. G. Gray, "General conservation equations for multi-phase systems: 1. Averaging procedure," *Advances in Water Resources*, vol. 2, pp. 131–144, 1979.
- [13] S. Banerjee and A. M. C. Chan, "Separated flow models-I. Analysis of the averaged and local instantaneous formulations," *International Journal of Multiphase Flow*, vol. 6, no. 1–2, pp. 1–24, 1980.
- [14] J. M. Delhaye, "Basic equations for two phase flow modeling," in *Two-Phase Flow and Heat Transfer in the Power and Process Industries*, A. E. Bergles, J. G. Collier, J. M. Delhaye, G. F. Hewitt, and F. Mayinger, Eds., pp. 40–97, Hemisphere, Washington, DC, USA, 1981.
- [15] W. T. Sha, B. T. Chao, and S. I. Soo, "Time averaging of volume averaged conservation equation of multiphase flow," in *Proceedings of the 21st ASME/AIChE National Heat Transfer Conference*, pp. 420–426, Seattle, Wash, USA, 1983.
- [16] W. T. Sha and B. T. Chao, "Novel porous media formulation for multiphase flow conservation equations," *Nuclear Engineering and Design*, vol. 237, no. 9, pp. 918–942, 2007.

- [17] G. Dagan, "Statistical theory of groundwater flow and transport: poro to laboratory, laboratory to formation, and formation to regional scale," *Water Resources Research*, vol. 22, no. 9, pp. 1205–1345, 1986.
- [18] T. C. S. M. Gupta, A. N. Goswami, and B. S. Rawat, "Mass transfer studies in liquid membrane hydrocarbon separations," *Journal of Membrane Science*, vol. 54, no. 1-2, pp. 119–130, 1990.
- [19] M. L. Brusseau, "Transport of reactive contaminants in heterogeneous porous media," *Reviews of Geophysics*, vol. 32, no. 3, pp. 285–313, 1994.
- [20] M. Quintard and S. Whitaker, "Convection, dispersion, and interfacial transport of contaminants: homogeneous porous media," *Advances in Water Resources*, vol. 17, no. 4, pp. 221–239, 1994.
- [21] T. K. Sen and K. C. Khilar, "Review on subsurface colloids and colloid-associated contaminant transport in saturated porous media," *Advances in Colloid and Interface Science*, vol. 119, no. 2-3, pp. 71–96, 2006.
- [22] P. F. M. M. Correia and J. M. R. De Carvalho, "A comparison of models for 2-chlorophenol recovery from aqueous solutions by emulsion liquid membranes," *Chemical Engineering Science*, vol. 56, no. 18, pp. 5317–5325, 2001.
- [23] H. Cho, S. N. Shah, and S. O. Osisanya, "A three-segment hydraulic model for cuttings transport in coiled tubing horizontal and deviated drilling," *Journal of Canadian Petroleum Technology*, vol. 41, no. 6, pp. 32–39, 2002.
- [24] G. Espinosa-Paredes and O. Cazarez-Candia, "Two-region average model for cuttings transport in horizontal wellbores I: transport equations," *Petroleum Science and Technology*, vol. 29, no. 13, pp. 1366–1376, 2011.
- [25] G. Espinosa-Paredes and O. Cazarez-Candia, "Two-region average model for cuttings transport in horizontal wellbores II: interregion conditions," *Petroleum Science and Technology*, vol. 29, no. 13, pp. 1377–1386, 2011.
- [26] S. C. Lee, "Continuous extraction of penicillin G by emulsion liquid membranes with optimal surfactant compositions," *Chemical Engineering Journal*, vol. 79, no. 1, pp. 61–67, 2000.
- [27] E. Bayraktar, "Response surface optimization of the separation of DL-tryptophan using an emulsion liquid membrane," *Process Biochemistry*, vol. 37, no. 2, pp. 169–175, 2001.
- [28] T. B. Anderson and R. Jackson, "A fluid mechanical description of fluidized beds," *Industrial & Engineering Chemistry Fundamentals*, vol. 6, pp. 527–538, 1967.
- [29] C. M. Marle, "Écoulements monophasique en milieu poreux," *Revue de l'Institut Français du Pétrole*, vol. 22, pp. 1471–1509, 1967.
- [30] C. A. Truesdell and R. A. Toupin, "The classical field theories," in *Encyclopedia of Physics*, S. Flugge, Ed., vol. 3/1, pp. 226–858, Springer, 1960.
- [31] J. H. Cushman, "Multiphase transport equations I: general equation for macroscopic local space-time homogeneity," *Transport Theory and Statistical Physics*, vol. 12, no. 1, pp. 35–71, 1983.
- [32] G. Espinosa-Paredes, "Jump mass transfer for double emulsion systems," *International Mathematical Forum*, vol. 2, no. 32, pp. 1553–1570, 2007.
- [33] S. Whitaker, *The Method of Volume Averaging*, Kluwer Academic, Dodrecht, The Netherlands, 1999.
- [34] G. Espinosa-Paredes and A. Nuñez-Carrera, "SBWR model for steady state and transient analysis," *Science and Technology of Nuclear Installations*, vol. 2008, Article ID 428168, 18 pages, 2008.
- [35] C. Morel, "Modeling approaches for strongly non-homogeneous two-phase flows," *Nuclear Engineering and Design*, vol. 237, no. 11, pp. 1107–1127, 2007.